Universidade do Minho
Escola de Engenharia

Hung Mai Vu

Control of an anthropomorphic
manipulator involved in
physical Human-Robot Interaction

Master Dissertation
Master in Mechatronics Engineering

Work performed under the guidance of
Professor Estela Guerreiro da Silva Bicho Erlhagen

June, 2012

DECLARAÇÃO

Nome: Hung Mai Vu

Correio electrónico: maihungvu@gmail.com
Tlm. 925 376 306
Passaporte: B3714398

Título da dissertação:

Control of an anthropomorphic manipulator involved in physical Human-Robot Interaction

Ano de conclusão: 2012

Orientadora:
Professor Estela Guerreiro da Silva Bicho Erlhagen

Designação do Mestrado:
Master in Mechatronics Engineering

Escola:Engenharia
Departamento: Engenharia Mecânica

Guimarães, ___/___/_____

Assinatura: _____

To my loving parents,

Acknowledgments

I would like to give many thanks to many people that have contributed to my study and supported me in many ways over the last years.

I wish to express my deep gratitude to my scientific advisor Prof. Bicho Estela for giving me the opportunity to do the work presented in this thesis. Her guidance, support and friendship were essential for my achievement.

I am grateful to researchers Rui Silva, Toni Machado, Tiago Malheiro, Miguel Sousa, Emanuel Sousa, Eliana Costa, Luis Louro and Flora Ferreira for their support with robots and devices in the Anthropomorphic and Mobile Robotics Laboratory at the University of Minho. Their friendship also made the time that I have spent there more pleasant and interesting.

I would like to give thanks to Prof. Monteiro Caetano for smoothing academic procedures during my study at the University of Minho. Conversations with him inside and also outside the class were also interesting.

My many thanks go to all of my colleagues and friends, both Portuguese and Vietnamese who helped me in many ways. The time that we shared with each other in the beautiful city of Guimarães was very pleasant and special to me.

To my family, I wish to express my gratitude to my mother, Ban, to my sisters, Hien and Hoa for their endless support. Their love for me is the unlimited energy source for my achievement.

Abstract

The objective of the dissertation is to flexibly control the end effector velocity of a redundant 7-DOF manipulator by using a differential kinematics approach, while ensuring the safety of the robotic arm from exceeding the physical limits of joints in terms of position, velocity and acceleration. The thesis also contributes with a real-time obstacle avoidance strategy for controlling anthropomorphic robotic arms in dynamic obstacle environments, taking account of sudden appearances or disappearances of mobile obstacles. A method for compensating force errors due to changes in the orientation of end effectors, independent from structures of force sensors, is developed to achieve high accuracy in force control applications. A novel method, the Virtual Elastic System, is proposed to control mobile manipulators for physical Human-Robot Interaction (pHRI) tasks in dynamic environments, which enables the combination of an Inverse Differential Kinematics for redundant robotic arms and a Dynamical Systems approach for nonholonomic mobile platforms. Experiments with a 7-DOF robotic arm, side-mounted on a nonholonomic mobile platform, are presented with the whole robot obstacle avoidance, proving the efficiency of the developed method in pHRI scenarios, more specifically, cooperative human-robot object transportation tasks in dynamic environments. Extensions of the method for other mobile manipulators with holonomic mobile platforms or higher degrees of freedom manipulators are also demonstrated through simulations.

Keywords: *Redundant Manipulator, Real-time obstacles avoidance, Anthropomorphic Mobile Manipulator, Physical Human-Robot Interaction, Cooperative Object Transportation*

Contents

List of Figures

List of Tables

Chapter 1

Introduction

1.1 Anthropomorphic robotic systems

Nowadays, robotic systems have been playing an important role in the modern life. They are participating in production lines of the industrial manufacturing, helping patients during their recovery processes in hospitals, exploring deep oceans and space which are unknown to man and even supporting humans during their daily lives. Benefiting from advances in different technologies of mechanics, electronics, computers and controls, robots have been improved in both of their physical capabilities and intelligence for providing better services. Anthropomorphic robotics systems, which are capable to give friendly interactions with humans, are highly desired for applications involving human-robot physical interactions. Figure 1.1 presents two anthropomorphic robots ARoS and Dumbo which are available at the Anthropomorphic and Mobile Robotics Laboratory of the University of Minho. The available softwares, which were developed in the lab, enable the motion planning for the redundant 7-DOF manipulator to move the end effector from place to place with human-liked movements ([Costa e Silva et al., 2011]) and the navigation in dynamic environments of the mobile platform of the robot Dumbo while its robotic hand is kept still ([Malheiro et al., 2012]).
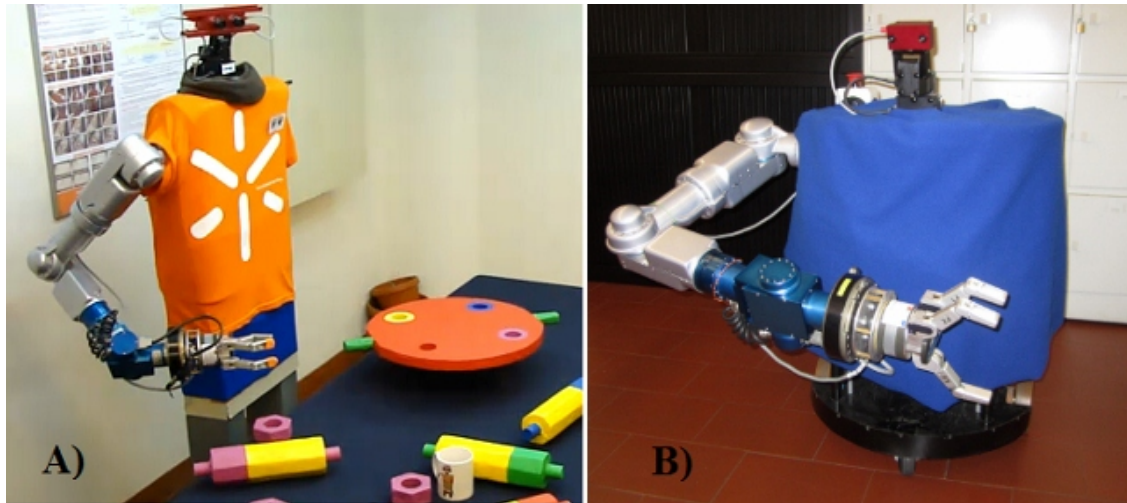
Figure 1.1: Anthropomorphic robotic systems, developed at the Anthropomorphic and Mobile Robotics Laboratory of the University of Minho: ARoS (A) and Dumbo (B)

In applications such as tracking, grasping a mobile object or moving the end effector with desired velocity profiles, the end effector needs to move at an equal or higher velocity to keep up with the moving target. In the case of using control strategies which allow the end effector to move from position to position by generating trajectories, such as motion planning, changes in the target's position or in its moving direction will most likely result in recalculating trajectories. Therefore, in such dynamic target applications, these control strategies become inadequate because of the high computational burden and also lack of flexibility. The control of anthropomorphic robotic arms faces more challenges in dynamic obstacle environments. When the end effector moves with a desired velocity, the challenge is keeping the links of robotic arms free from collisions with mobile obstacles. Moreover, sudden appearance or disappearance of obstacles in the workspace may result in undesired reactions of the robotic arm if the adopted control strategy is not prepared for these situations.

In anthropomorphic mobile manipulators, 7-DOF robotic arms can be side-mounted on mobile platforms to provide friendly human interactions. However, these types of mobile manipulators possess more geometric and kinematic constraints because rotational

movements of the mobile platform change strongly the manipulator configuration and may lead to a collision between the arm and the body. In the case of using a nonholonomic mobile platform, its limited movements make control strategies face even more challenges in ensuring the mobile platform to support the robotic arm properly while still having enough flexibility to navigate through unstructured and dynamic environments. The control methods, e.g. [Janiak & Tchon, 2010] and [Luca et al., 2010], which involve the calculation of an extended Jacobian matrix for unifying the control of mobile platforms and manipulators, become inadequate because local optimizations, based on the nullspace of the associated Jacobian, can not guarantee that all constraints between manipulators and mobile platform are satisfied. Free obstacles navigation for both of the manipulator and the mobile platform simultaneously is also a challenging issue.

Moreover, in physical human-robot interaction scenarios, robotic systems must respect some safety requirements because they and human partners share the same workspace to perform cooperative tasks. For instance, during human robot object transportation tasks, the robot is not supposed to move or rotate the object without forces, torques exerted by the human. Therefore, although anthropomorphic robotic systems are promising to provide elegant interactions with humans, a powerful control method is highly desired to fully exploit their capabilities and challenge physical Human-Robot Interaction applications.

1.2 Motivation of the thesis

The aims of this dissertation is to control a 7-DOF anthropomorphic robotic arm in velocity-constrained tasks by using the Inverse Differential Kinematics approach (see, e.g. [Wang et al., 2010] and [Papadopoulos & Poulakakis, 2000]). The kinematics of the redundant manipulator is fully studied, which covers the construction of the Jacobian matrix and the redundancy resolution and the singularity analysis. The safety of the robotic arm, in term of physical joints limits of position, velocity and also acceleration, is taken into

account with the real-time obstacle avoidance behavior for performing tasks in dynamic target and obstacles environments.

Another objective of the thesis is to control an anthropomorphic mobile manipulator for physical Human-Robot Interaction tasks in dynamic environments. A novel Virtual Elastic System approach is proposed to combine an Inverse Differential Kinematics, e.g. [Siciliano & Khatib, 2008] for redundant robotic arms and a Dynamical Systems approach, e.g. [Bicho et al., 2000] for nonholonomic mobile platforms and achieve free obstacles movements for the whole system.

Errors in forces and torques readings due to variations of the end effector orientation need to be eliminated to achieve higher accuracy in force control applications and an error compensation method is developed as another contribution of this work.

1.3   Organization of the thesis

The remainder of the thesis is organized into the following structure:

Chapter 2 presents the architecture of anthropomorphic robotic platforms, i.e. the robots ARoS and Dumbo, which are used in this work.

Chapter 3 presents kinematics studies of a redundant 7 degrees of freedom manipulator by using an Inverse Differential Kinematics approach. This includes the construction of the Jacobian matrix and redundancy resolution and singularity analysis of the robotic arm.

Chapter 4 focuses on exploiting the dexterity of the redundant robotic arm by optimizing the nullspace of the Jacobian matrix, which allows to control the 7-DOF anthropomorphic robotic arm in velocity-constrained tasks with real-time obstacle avoidance while ensuring the safety of the robotic arm from exceeding the physical limits of joints in terms of position, velocity and acceleration.

Chapter 5 is dedicated to a method which allows to achieve higher accuracy in force

control applications by removing the effect of the end effector orientation on forces and torques readings.

Chapter 6 proposes a novel method, so-called Virtual Elastic System, which enables the control of anthropomorphic mobile manipulators for physical Human-Robot Interactions in dynamic environments with collisions avoidance for the whole system. Extensions for mobile manipulators with holonomic mobile platform or higher degrees of freedom manipulators are illustrated through simulations.

And finally, Chapter 7 will summarize the work and discuss results.

Chapter 2

The experimental Anthropomorphic Robotic Systems

2.1   ARoS-An Anthropomorphic Robotic System

The robot Aros is an anthropomorphic robotic system that was designed and built in the Anthropomorphic and Mobile Robotics Laboratory of the University of Minho. Its construction, as well as equipments mounted on it, were supported by two research projects:

- European IP project *JAST (Joint-Action Science and Technology)*, financed by the European Commission (ref.IST-2-003747-IP).
- Portuguese project *Anthropomorphic robotic systems: control based on the processing principles of human and other primates' motor system and potential applications in service robotics and biomedical engineering*, financed by FCT (Fundacão para a Ciência e a Tecnologia) and University of Minho (ref.CON-CRREEQ/17/2001).

The architecture of ARoS which is used in the first part of this thesis, is presented in Figure 2.1. It consists of a vision system which is composed of two cameras, using stereo image processing to provide 3D coordinates of objects in real-time. A pan-tilt module in the neck of ARoS is used to change the direction where the robot is looking.
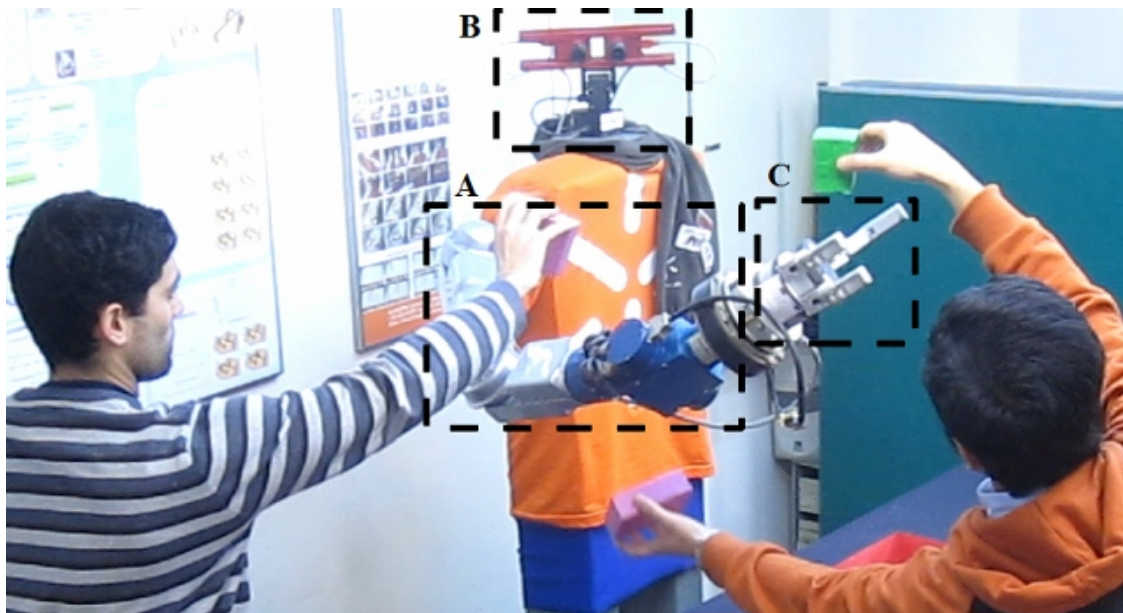
Figure 2.1: The robot ARoS-Anthropomorphic Robotic System consists of a 7-DOF robotic arm (A), a stereo vision system with two cameras mounted on a pan-tilt unit (B) and a 3 fingers robotic hand (C)

The anthropomorphic robotic arm of ARoS is the Light Weight Arm 7-DOF from AMTEC Robotics/Schunk^{TM}. It weights 12 kg and supports a total payload of 3 kg. The arm consists of seven revolutes joints with rotation directions as in Figure 2.2. The robot arm has some important points that are corresponding to the human arm:

S-Center of the **S**houlder

E-Center of the **E**lbow

W-Center of the **W**rist

H-Center of the **H**and

The dimension of the robotic arm is proportional to the human arm and the lengths of its links are available in Table 2.1. Characteristics of joints include joint limits, minimum increments, maximum velocities and maximum accelerations are available in Table 2.2. The joint values in the table are in the case that all the robot links are stretched out. The manufacturer, AMTEC Robotics/Schunk^{TM}, provides high level interface functions while the low level control is performed, in each joint, by an embedded Proportional-Integral-
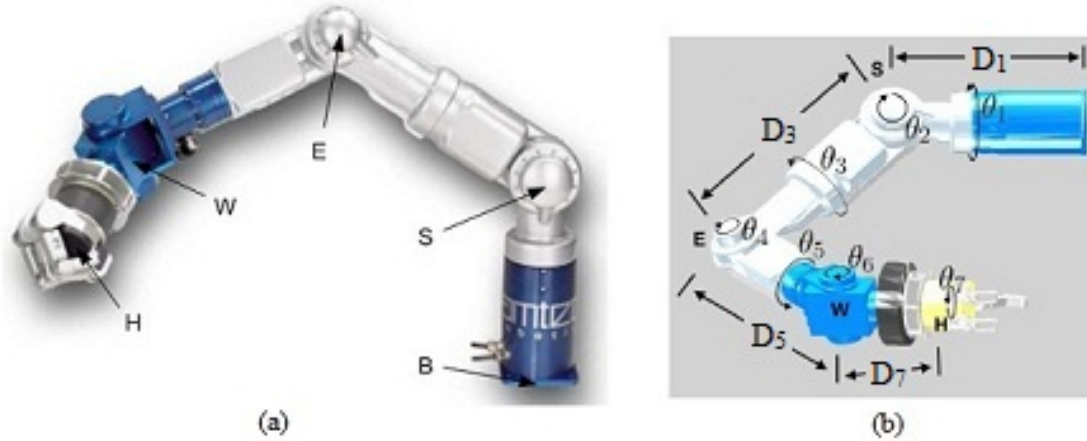
Figure 2.2: The 7-DOF Light Weight Arm from AMTEC Robotics/Schunk^{TM} and the hand of BH8-series from BarrettHand^{TM}: the real image of the arm and the hand (a) and their CAD models (b).

Table 2.1: Lengths of robotic arm links

Description	Notation	Length (mm)
Distance from the Base to the Shoulder	D_1	400
Distance from the Shoulder to the Elbow	D_3	395
Distance from the Elbow to the Wrist	D_5	370
Distance from the Wrist to the Hand	D_7	260

Derivative (PID) controller. The controller guarantees that tasks will be executed in desired time intervals unless the high level interface issues an error.

The robotic arm is equipped with a 6-DOF force sensor FCT50 from Schunk^{TM} at the wrist, which captures forces and torques acting on the end effector. The end effector is a robotic hand of the BH8-series from BarrettHand^{TM}. It has three fingers, each with one degree of freedom and two of the fingers have an extra degree of freedom, for providing lateral mobility and allows for objects to be grasped in different ways. Each of the fingers

is equipped with a force sensor that provides feedback of the grasped object.

Table 2.2: Characteristics of joints

	Joint limits	Max velocity	Max acceleration
	(deg)	(deg/sec)	(deg/sec^2)
θ_1	[-165,165]	52.2	208.8
θ_2	[-105,91]	52.2	208.8
θ_3	[-165,165]	52.2	208.8
θ_4	[-115,106]	41.2	164.8
θ_5	[-165,165]	41.2	164.8
θ_6	[-120,120]	240.0	960.0
θ_7	[-165,165]	360.0	1440.0

2.2 Dumbo-An anthropomorphic Mobile Manipulator

The architecture of the anthropomorphic mobile manipulator Dumbo, used in the second part of this work, is presented in Figure 2.3. The robot is also equipped with a Light Weight Arm 7-DOF from AMTEC Robotics/Schunk^{TM} with a robotic hand of the BH8-series from BarrettHand^{TM}. A 6-DOF force sensor FCT50 from Schunk^{TM} is mounted on the wrist, which captures forces and torques acting on the end effector. In addition, the anthropomorphic robotic arm is side-mounted on a nonholonomic 2-wheels mobile platform for providing human friendly interactions.

On the top of the mobile platform, there is a vision system which consists of two cameras, using stereo image processing to provide 3D coordinates of objects in real-time.
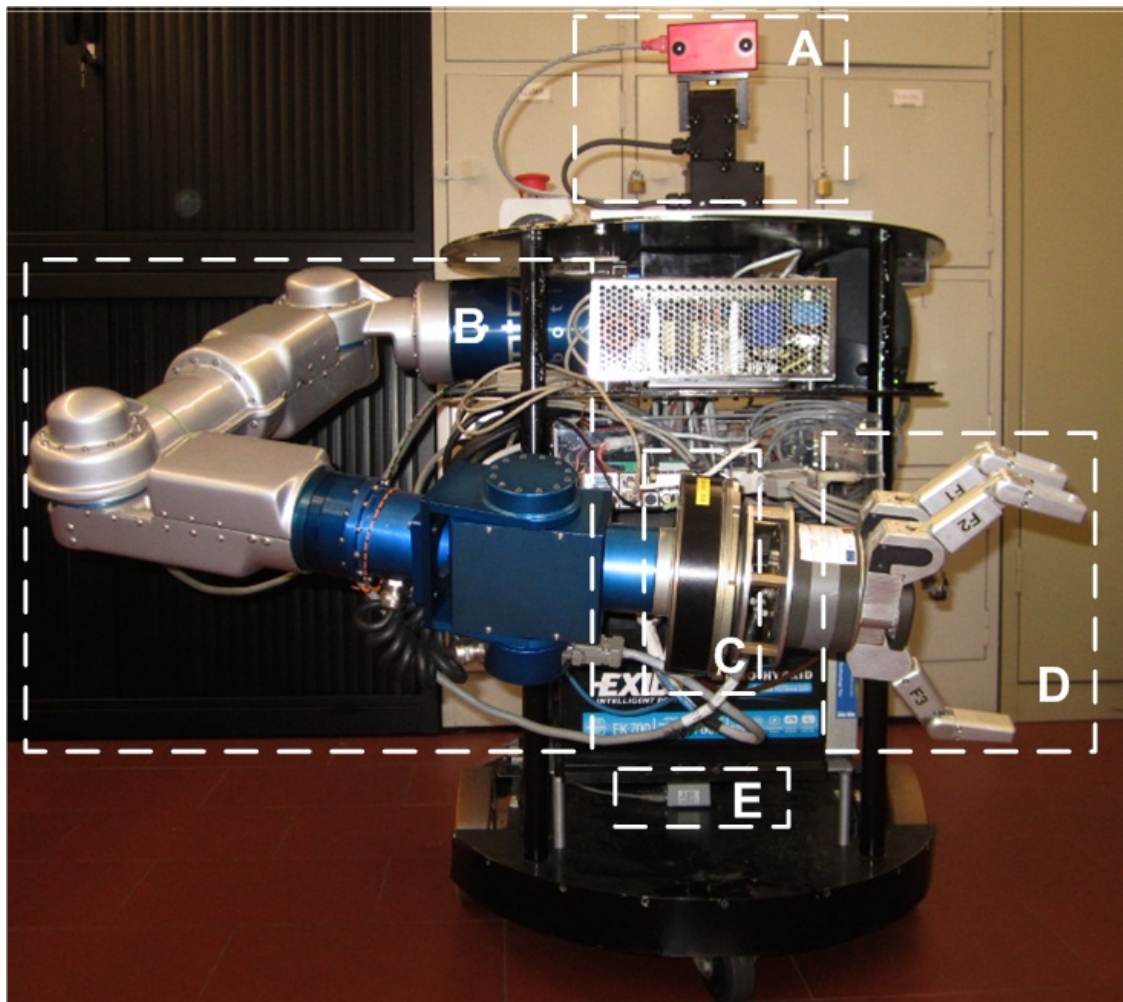
Figure 2.3: The experimental anthropomorphic mobile manipulators Dumbo consists of a stereo vision system with two cameras mounted on a pan-tilt unit (A), a 7-DOF robotic arm (B), side-mounted on a nonholonomic mobile platform, a 6 DOF force sensor (C), mounted at the Wrist, a 3 fingers robotic hand (D) for grasping objects and a laser range finder (E) for acquiring distances from obstacles. The robot is also equipped with a speaker for verbal communication and operates with two 24V batteries

The vision system is mounted on a pan-tilt module, acting like a neck to change the direction where the robot is looking. Verbal communication with the human partner during interactions is provided by equipping a speaker with speech synthesis from Speech Application Programming Interface that is available from Microsoft. The mobile platform

has also a laser range finder URG-04LX to acquire distances from obstacles up to 4 meters on the ground. The robot is powered by two 24V batteries which enables it to move long distances to perform tasks involving physical interactions with humans.

Chapter 3

Differential Kinematics for a redundant 7-DOF robotic arm

3.1 Basic concepts

3.1.1 Spatial descriptions and transformations

Consider {W} as the world coordinate system with unit vectors $\{\hat{x}, \hat{y}, \hat{z}\}$, any point P in the world can be expressed in this reference frame as $^W P = [p_x, p_y, p_z]^T$. The rotation of a reference frame {A} relative to {W} with unit vectors $\hat{x}_A$, $\hat{y}_A$, $\hat{z}_A$ expressed in {W} is a 3x3 matrix, called rotation matrix, $^W R_A$, whose columns are unit vectors.

$$^W R_A = [\hat{x}_A, \hat{y}_A, \hat{z}_A]. \tag{3.1}$$

Every rotation matrix is a proper orthonormal matrix since $(^W R_A)^{T}.^W R_A = I$ and its inverse is simply its transpose i.e. $(^W R_A)^{-1} = (^W R_A)^T$, defining the rotation of {W} relative to {A}.

Consider two frames {A} and {B} with their origins O_A and O_B, and the rotation matrix $^A R_B$ of {A} relative to {B}, we would like to determine the description of a vector

---

P in {A}, i.e. ^{A}P, given the known description of P in {B}, i.e. ^{B}P.

$$^{A}P =^{A} O_B +^{A} (O_B P) =^{A} O_B +^{A} R_B \, ^{B}P, \tag{3.2}$$

where $^{A}O_B$ is the description of the origin O_B in {A}. This expression can be written in another form:

$$\begin{bmatrix} ^{A}P \\ 1 \end{bmatrix} = \left[\begin{array}{c|c} ^{A}R_B & ^{A}O_B \\ \hline 0\,0\,0 & 1 \end{array} \right] \begin{bmatrix} ^{B}P \\ 1 \end{bmatrix}$$
$$^{A}P_h = \, ^{A}T_B^{B} P_h. \tag{3.3}$$

where h stands for homogeneous and the matrix $^{A}T_B$ is called the homogeneous transformation matrix from B to A, or simply the transformation matrix.

The rotation matrix $^{A}R_B = [^{A}\hat{x}_B,^{A} \hat{y}_B,^{A} \hat{z}_B]$ has nine elements but can be specified by only three parameters because of constraints of unit vectors. The orientation of a reference frame relative to another is represented by three rotations about three orthonormal axes. The most common rotation representations are X-Y-Z fixed angle, Z-Y-X Euler angle and Z-Y-Z Euler angle. In X-Y-Z fixed angle representation, which is used in this chapter, the rotation of the frame {B} relative to the frame {A} involves three steps: rotating a frame coinciding with {A} about x_A by an angle γ, then about y_A by an angle β and, finally, about z_A by an angle α. By using the roll, pitch, yaw angles, i.e. α, β and γ angles, the rotation matrix is determined by the following expression:

$$^{A}R_B(\gamma, \beta, \alpha) = R_z(\alpha).R_y(\beta).R_x(\gamma)$$

$$= \begin{bmatrix} c\alpha & -s\alpha & 0 \\ s\alpha & c\alpha & 0 \\ 0 & 0 & 1 \end{bmatrix} \begin{bmatrix} c\beta & 0 & s\beta \\ 0 & 1 & 0 \\ -s\beta & 0 & c\beta \end{bmatrix} \begin{bmatrix} 1 & 0 & 0 \\ 0 & c\gamma & -s\gamma \\ 0 & s\gamma & c\gamma \end{bmatrix}$$

$$= \begin{bmatrix} c\alpha.c\beta & c\alpha.s\beta.s\gamma - s\alpha.c\gamma & c\alpha.s\beta.c\gamma + s\alpha.s\gamma \\ s\alpha.c\beta & s\alpha.s\beta.s\gamma + c\alpha.c\gamma & s\alpha.s\beta.c\gamma - c\alpha.s\gamma \\ -s\beta & c\beta.s\gamma & c\beta.c\gamma \end{bmatrix}. \tag{3.4}$$

where the notations of c and s stand for cosine and sine of the associated angle, respectively.

3.1.2 Denavit-Hartenberg convention

In robotics, the Denavit-Hartenberg (D-H) convention is commonly used for describing robot arms. The robot arm will be reset to its zero position whose joint angles are equal to zero. The following procedure is used for attaching properly reference frames to robot links (Craig [2005]):

1. Assign the Z_i axis pointing along the ith joint axis.
2. Identify the common perpendicular between Z axes, or point of intersection. At the point of intersection, or at the point where the common perpendicular meets the ith axis, assign the link-frame origin.
3. Assign the X_i axis pointing along the common perpendicular, or, if the axes intersect, assign X_i to be normal to the plane containing the two axes.
4. Assign the Y axis to complete a right-hand coordinate system.
5. Assign the frame attaching to the robot base {0} to match frame {1} when the first joint variable is zero. For the last frame {N}, choose an origin location and X_N direction freely, but generally so as to cause as many linkage parameters as possible to become zero.

After reference frames are determined, Denavit-Hartenberg parameters (3.1) are defined as follows:

$$a_{i-1} = \text{the distance from } Z_{i-1} \text{ to } Z_i \text{ measured along } X_{i-1}$$

$$\alpha_{i-1} = \text{the angle from } Z_{i-1} \text{ to } Z_i \text{ measured about } X_{i-1}$$

$$d_i = \text{the distance from } X_{i-1} \text{ to } X_i \text{ measured along } Z_i$$

$$\theta_i = \text{the angle from } X_{i-1} \text{ to } X_i \text{ measured about } Z_i$$
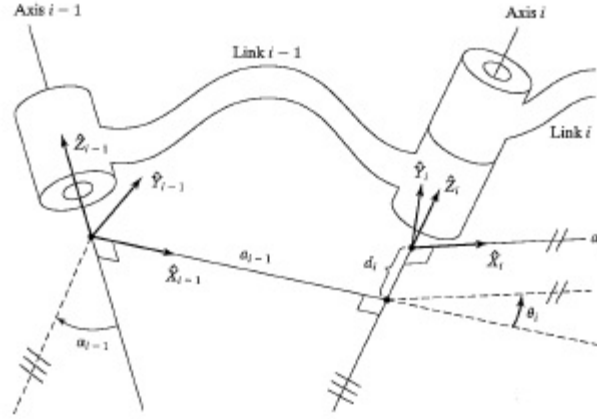
Figure 3.1: D-H parameters

Using those parameters, the transformation matrix $^{i-1}T_i$ that transforms vectors defined in {i} to their description in {i-1} is determined:

$$^{i-1}T_i = Rot(X_{i-1}, \alpha_{i-1}).Trans(X_{i-1}, a_{i-1}).Rot(Z_i, \theta_i).Trans(Z_i, d_i)$$

$$= \begin{bmatrix} 1 & 0 & 0 & 0 \\ 0 & c\alpha_{i-1} & -s\alpha_{i-1} & a_{i-1} \\ 0 & s\alpha_{i-1} & c\alpha_{i-1} & 0 \\ 0 & 0 & 0 & 1 \end{bmatrix} \begin{bmatrix} c\theta_i & -s\theta_i & 0 & 0 \\ s\theta_i & c\theta_i & 0 & 0 \\ 0 & 0 & 1 & d_i \\ 0 & 0 & 0 & 1 \end{bmatrix}$$

$$= \begin{bmatrix} c\theta_i & -s\theta_i & 0 & a_{i-1} \\ s\theta_i.c\alpha_{i-1} & c\theta_i.c\alpha_{i-1} & -s\alpha_{i-1} & -s\alpha_{i-1}.d_i \\ s\theta_i.s\alpha_{i-1} & c\theta_i.s\alpha_{i-1} & c\alpha_{i-1} & c\alpha_{i-1}.d_i \\ 0 & 0 & 0 & 1 \end{bmatrix}. \tag{3.5}$$

3.2 Geometric Kinematics of a 7 DOF manipulator

3.2.1 Direct Geometric Kinematics

The goal of the direct geometric kinematic is to determine the position and the orientation of the end effector from the joint angles $\{\theta_1, \theta_2, \theta_3, \theta_4, \theta_5, \theta_6, \theta_7\}$. Figure 3.2 depicts the
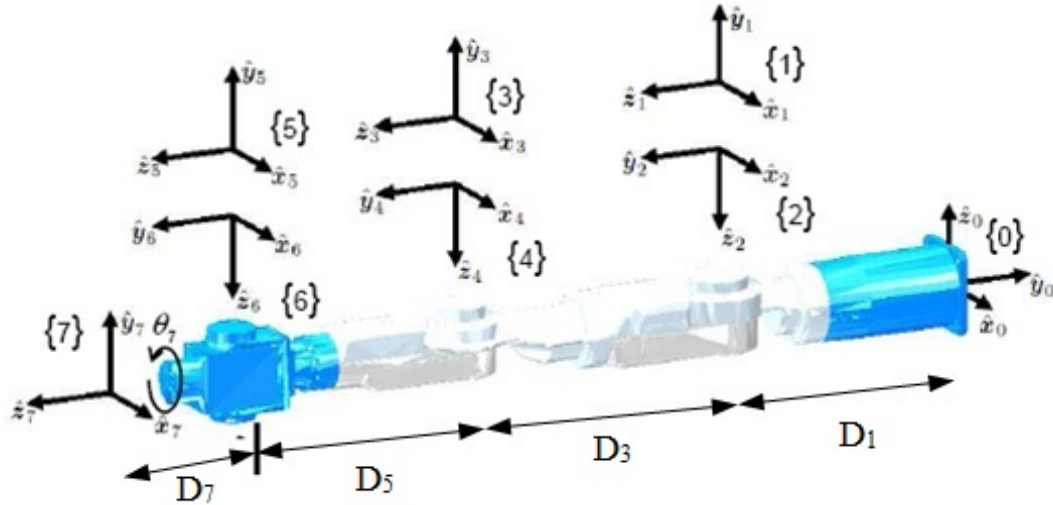
Figure 3.2: The 7-DOF manipulator with reference frames assigned by following the Denavit-Hartenberg convention ([Costa e Silva, 2011])

7-DOF manipulator at the zero position of joints with reference frames assigned by following the Denavit-Hartenberg convention. The D-H parameters for the arm is available in Table 3.1. All parameters are constant, except joint angles θ_i because all seven joints of ARoS are revolute.

For simplicity, let us denote $\cos(\theta_i)$ and $\sin(\theta_i)$ as $c\theta_i$ and $s\theta_i$ for $i = 1, ..., 7$. The transformation matrices are calculated by applying Eq 3.5 and presented in the following

Table 3.1: D-H parameters for a 7-DOF manipulator

i	α_{i-1}	a_{i-1}	d_i	θ_i
	(deg)	(mm)	(mm)	(deg)
1	90	0	340	θ_1
2	90	0	0	θ_2
3	-90	0	395	θ_3
4	90	0	0	θ_4
5	-90	0	370	θ_5
6	90	0	0	θ_6
7	-90	0	260	θ_7

equations:

$$
{}^0T_1 = \begin{bmatrix} c\theta_1 & -s\theta_1 & 0 & 0 \\ 0 & 0 & -1 & -D_1 \\ s\theta_1 & c\theta_1 & 0 & 0 \\ 0 & 0 & 0 & 1 \end{bmatrix}, \tag{3.6}
$$

For $i = 2, 4, 6$

$$
{}^{i-1}T_i = \begin{bmatrix} c\theta_i & -s\theta_i & 0 & 0 \\ 0 & 0 & -1 & 0 \\ s\theta_i & c\theta_i & 0 & 0 \\ 0 & 0 & 0 & 1 \end{bmatrix}, \tag{3.7}
$$

For $i = 3, 5, 7$

$$
{}^{i-1}T_i = \begin{bmatrix} c\theta_i & -s\theta_i & 0 & 0 \\ 0 & 0 & 1 & D_i \\ -s\theta_i & -c\theta_i & 0 & 0 \\ 0 & 0 & 0 & 1 \end{bmatrix}. \tag{3.8}
$$

The total transformation matrix ${}^0T_7$ is acquired by multiplying all seven transformation matrices. It is a 4x4 matrix and allowing to extract the position of the end effector, O_7, and also three axes of the hand reference frame, all expressed in the base reference frame {0}.

$$
{}^0T_7 = {}^0T_1 \, {}^1T_2 \, {}^2T_3 \, {}^3T_4 \, {}^4T_5 \, {}^5T_6 \, {}^6T_7 = \left[\begin{array}{ccc|c} {}^0\hat{X}_7 & {}^0\hat{Y}_7 & {}^0\hat{Z}_7 & {}^0\hat{O}_7 \\ \hline 0 & 0 & 0 & 1 \end{array} \right]. \tag{3.9}
$$

The orientation of the end effector is also determined by acquiring the roll, pitch and yaw angles $\{\alpha, \beta, \gamma\}$ from the rotation matrix ${}^0R_7$:

$$
{}^0R_7(\gamma, \beta, \alpha) = \begin{bmatrix} {}^0\hat{X}_7 & {}^0\hat{Y}_7 & {}^0\hat{Z}_7 \end{bmatrix} = \begin{bmatrix} r_{11} & r_{12} & r_{13} \\ r_{21} & r_{22} & r_{23} \\ r_{31} & r_{32} & r_{33} \end{bmatrix}. \tag{3.10}
$$

By comparing with the equation 3.4, in case of $c\beta \neq 0$, i.e. $r_{31} \neq \pm 1$, the solution will be:

$$
\beta = \arctan\left(-r_{31}, \sqrt{r_{11}^2 + r_{21}^2}\right), \tag{3.11}
$$

$$
\alpha = \arctan\left(\frac{r_{21}}{c\beta}, \frac{r_{11}}{c\beta}\right), \tag{3.12}
$$

$$
\gamma = \arctan\left(\frac{r_{32}}{c\beta}, \frac{r_{33}}{c\beta}\right), \tag{3.13}
$$

If $r_{31} = 1$,

$$
\beta = -\frac{\pi}{2}, \tag{3.14}
$$

$$
\alpha = 0, \tag{3.15}
$$

$$
\gamma = -\arctan(r_{12}, r_{22}), \tag{3.16}
$$

If $r_{31} = -1$,

$$\beta = \frac{\pi}{2}, \tag{3.17}$$

$$\alpha = 0, \tag{3.18}$$

$$\gamma = \arctan(r_{12}, r_{22}). \tag{3.19}$$

Similarly, the position and orientation of the Shoulder, the Elbow and the Wrist can be extracted from the transformation matrices $^0T_1$, $^0T_3$ and $^0T_5$, respectively.

3.2.2 Inverse Geometric Kinematics

The goal of the inverse geometric kinematics is to determine the joint angles $\{\theta_1, \theta_2, \theta_3, \theta_4, \theta_5, \theta_6, \theta_7\}$, given the position $\{x_e, y_e, z_e\}$ and the orientation of the end effector. The orientation will be specified by the roll, pitch and yaw angles $\{\alpha, \beta, \gamma\}$. Because the robotic arm is redundant, seven joint angles need to be solved from six equations. Thus, the inverse kinematics have an infinite number of solutions as illustrated in Figure 3.3. The position of the Shoulder is fixed relative to the Base and the position of the Wrist is also fixed if the position and orientation of the end effector are given. However, the arm is still able to rotate around the fixed axis Shoulder-Wrist (SW) without changing the pose of the hand and positions of the Elbow form a circle. Therefore, by introducing a new variable ψ, the angle between the plane formed by the Shoulder, the Elbow and the Wrist with the plane which is parallel to the floor and contains the Shoulder and the Wrist, only one solution for each value of the Arm plane angle ψ is acquired ([Costa e Silva, 2011]).

3.2.3 Solution of θ_4

From given values of angles $\{\alpha, \beta, \gamma\}$, the total rotation matrix $^0R_7$ is calculated by using Eq 3.4. Combining with the position of the end effector $^0O_7 = [x_e \ \ y_e \ \ z_e]^T$, the total transformation matrix $^0T_7$ is determined by Eq 3.9. The position of the Shoulder is fixed,
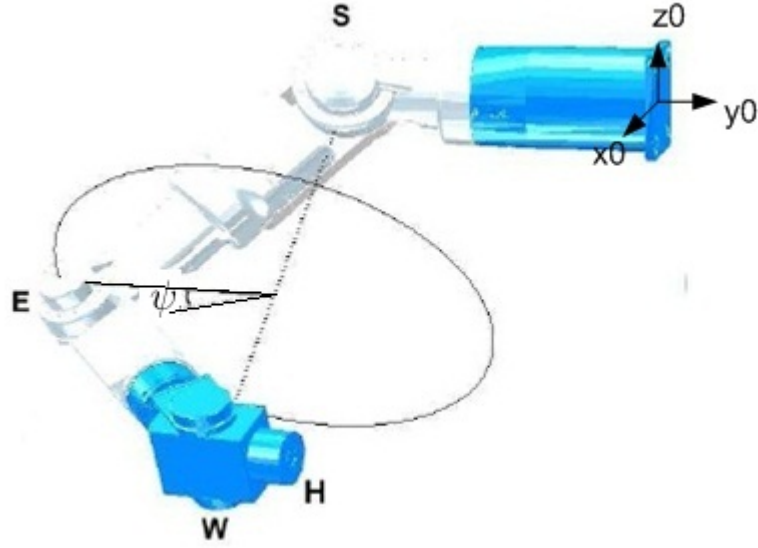
Figure 3.3: Infinite solutions for the inverse geometric kinematics in a 7-DOF manipulator

i.e. $S = \begin{bmatrix} 0 & -D_1 & 0 \end{bmatrix}^T$ and the position of the Wrist is computed by:

$$W = {}^0O_5 = {}^0O_7 - D_7 {}^0\hat{Z}_7, \tag{3.20}$$

Thus, the distance of the Shoulder-Wrist is:

$$L_{SW} = \sqrt{x_W^2 + (y_W + D_1)^2 + z_W^2}, \tag{3.21}$$

where x_W, y_W and z_W are the coordinates of the Wrist, computed from Eq 3.20. The joint angle θ_4 is determined by using the Cosine theorem in the triangle SEW as illustrated in Figure 3.4.

$$\theta_4 = -\arccos(\frac{L_{SW}^2 - D_3^2 - D_5^2}{2D_3 D_5}). \tag{3.22}$$

3.2.4 Determining the Elbow

Denote C as the center of the circle where the Elbow is located, using the Cosine theorem in the triangle SEW:

$$\cos(\eta) = \frac{D_3^2 + L_{SW}^2 - D_5^2}{2D_3 L_{SW}}, \tag{3.23}$$
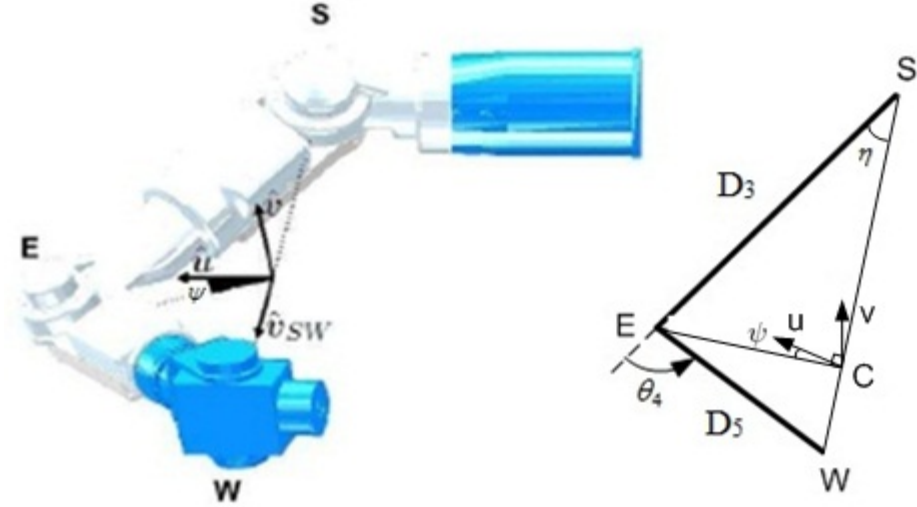
Figure 3.4: Introducing the Arm plane angle ψ for redundancy resolution in inverse geometric kinematics

Then, the distance from C to the Shoulder is

$$L_{SC} = D_3 cos(\eta) = \frac{D_3^2 + L_{SW}^2 - D_5^2}{2L_{SW}},$$

(3.24)

The position of the circle center C is

$$C = W + (W - S)\frac{L_{SC}}{L_{SW}},$$

(3.25)

where W and S are the coordinates of the Wrist and the Shoulder, respectively. The radius of the circle, R is computed by:

$$R = \sqrt{D_3^2 - L_{SC}^2}.$$

(3.26)

The unit vector $\hat{u}$ located in the plane which is parallel to the floor and containing the line SW is determined by:

$$\hat{u} = \frac{1}{L_{WS}}((W - S) \times Z_0),$$

(3.27)

and the unit vector $\hat{v}$ is computed from:

$$\hat{v} = \frac{1}{L_{WS}}(\hat{u} \times (W - S)).$$

(3.28)

By introducing the Arm plane angle ψ between the plane Shoulder-Elbow-Wrist and the plane containing the vector $\hat{u}$ and the line WS, the position of the Elbow is determined by:

$$E = C + R(\hat{u}\cos\psi - \hat{v}\sin\psi), \tag{3.29}$$

Then, the axes of the reference frame {4} are determined.

$$Z_4 = \frac{(W - E) \times (E - S)}{\|(W - E) \times (E - S)\|}, \tag{3.30}$$

$$Y_4 = \frac{W - E}{\|W - E\|}, \tag{3.31}$$

$$X_4 = Y_4 \times Z_4. \tag{3.32}$$

From here, the rotation matrices $^0R_4$ and $^3R_4$ are specified.

3.2.5 Solutions of θ_1, θ_2 and θ_3

The rotation matrix $^0R_3$ is computed from the rotation matrices $^0R_4$ and $^3R_4$:

$$^0R_3 = ^0R_4(^3R_4)^{-1} = ^0R_4(^3R_4)^T, \tag{3.33}$$

Simultaneouly, the matrix $^0R_3$ can also be calculated from values of θ_1, θ_2 and θ_3:

$$^0R_3 = \begin{bmatrix} c\theta_1 c\theta_2 c\theta_3 - s\theta_1 s\theta_3 & -c\theta_1 c\theta_2 s\theta_3 - s\theta_1 c\theta_3 & -c\theta_1 s\theta_2 \\ -s\theta_2 c\theta_3 & s\theta_2 s\theta_3 & -c\theta_2 \\ s\theta_1 c\theta_2 c\theta_3 + c\theta_1 s\theta_3 & -s\theta_1 c\theta_2 s\theta_3 + c\theta_1 c\theta_3 & -s\theta_1 s\theta_2 \end{bmatrix} = \begin{bmatrix} r_{11} & r_{12} & r_{13} \\ r_{21} & r_{22} & r_{23} \\ r_{31} & r_{32} & r_{33} \end{bmatrix}, \tag{3.34}$$

Then, the solution of θ_2 is:

$$\theta_2 = \arctan\left(-\sqrt{1 - r_{23}^2}, -r_{23}\right), \tag{3.35}$$

If $s\theta_2 \neq 0$, the solutions of θ_1 and θ_3 will be:

$$\theta_1 = \arctan\left(\frac{-r_{33}}{s_2}, \frac{-r_{13}}{s_2)}\right), \tag{3.36}$$

$$\theta_3 = \arctan\left(\frac{r_{22}}{s_2}, \frac{-r_{21}}{s_2)}\right), \tag{3.37}$$

If $s\theta_2 = 0$, this singularity will be overcome by choosing a value for θ_1:

$$\theta_1 = 0, \tag{3.38}$$

$$\theta_3 = \arctan(r_{31}, r_{11}). \tag{3.39}$$

3.2.6 Solutions of θ_5, θ_6 and θ_7

The rotation matrix ${}^{4}R_7$ is computed from the rotation matrices ${}^{0}R_7$ and ${}^{0}R_4$:

$$^{4}R_7 = ({}^{0}R_4)^{-1}({}^{0}R_7) = ({}^{0}R_4)^{T}({}^{0}R_7), \tag{3.40}$$

Simultaneously, the rotation matrix ${}^{4}R_7$ can also be calculated from values of θ_5, θ_6 and θ_7:

$$^{4}R_7 = \begin{bmatrix} c\theta_5 c\theta_6 c\theta_7 - s\theta_5 s\theta_7 & -c\theta_5 c\theta_6 s\theta_7 - s\theta_5 c\theta_7 & -c\theta_5 s\theta_6 \\ -s\theta_6 c\theta_7 & -s\theta_6 s\theta_7 & c\theta_6 \\ -s\theta_5 c\theta_6 c\theta_7 - c\theta_5 s\theta_7 & s\theta_5 c\theta_6 s\theta_7 - c\theta_5 c\theta_7 & s\theta_5 s\theta_6 \end{bmatrix} = \begin{bmatrix} r_{11} & r_{12} & r_{13} \\ r_{21} & r_{22} & r_{23} \\ r_{31} & r_{32} & r_{33} \end{bmatrix}, \tag{3.41}$$

Then, the solution of θ_6 is

$$\theta_6 = \arctan\left(-\sqrt{1 - r_{23}{}^2}, r_{23}\right), \tag{3.42}$$

If $s\theta_6 \neq 0$, the solutions of θ_5 and θ_7 will be:

$$\theta_5 = \arctan\left(\frac{r_{33}}{s_6}, \frac{-r_{13}}{s_6}\right), \tag{3.43}$$

$$\theta_7 = \arctan\left(\frac{-r_{22}}{s_6}, \frac{r_{21}}{s_6}\right), \tag{3.44}$$

If $s\theta_6 = 0$, this singularity will be overcome by choosing a value for θ_5:

$$\theta_5 = 0, \tag{3.45}$$

$$\theta_7 = \arctan(-r_{31}, r_{11}). \tag{3.46}$$

3.2.7 Discussion

The geometric kinematics approach allows to move the robotic arm from position to position. However, it requires the position and orientation of the end effector to be specified for solving joint angles. In case of the 7-DOF robotic arm, the value of the Arm plane angle ψ must be selected for redundancy resolution.

The differential kinematics approach gives many advantages over the geometric kinematics in term of flexibility. The dexterity of redundant robotic arms is exploited flexibly. More specifically, the method allows to specify only components of the end effector velocity vector that need to be controlled for solving the joint velocities and thus, leaving more degree of freedom of the manipulator to implement additional behaviors such as joint limits avoidance and obstacle avoidance.

3.3 Differential kinematics of a 7 DOF manipulator

3.3.1 Direct differential kinematics

In direct differential kinematics, the velocity of the end effector, V_E, (attached to the reference frame {7}), with respect to the base reference frame {0}, can be obtained from the velocities of joints by:

$$V_E = {}^0 J_7 \dot{q}, \tag{3.47}$$

where V_E and $\dot{q}$ are the velocity of the end effector and the joints respectively.

$$V_E = \begin{bmatrix} v_X & v_Y & v_Z & \omega_X & \omega_Y & \omega_Z \end{bmatrix}^T, \tag{3.48}$$

$$\dot{q} = \begin{bmatrix} \dot{\theta}_1 & \dot{\theta}_2 & \dot{\theta}_3 & \dot{\theta}_4 & \dot{\theta}_5 & \dot{\theta}_6 & \dot{\theta}_7 \end{bmatrix}^T. \tag{3.49}$$

and ${}^0 J_7$ is the direct Jacobian matrix.

In the 7 DOF robotic arm, all seven joints are revolute, therefore the direct Jacobian

can be computed from:

$$
{}^0 J_7 = \begin{bmatrix} {}^0 Z_1 \times ({}^0 O_7 - {}^0 O_1) & ... & {}^0 Z_7 \times ({}^0 O_7 - {}^0 O_7) \\ {}^0 Z_1 & ... & {}^0 Z_7 \end{bmatrix},
\tag{3.50}
$$

where the vectors ${}^0 Z_i$ and ${}^0 O_i$, used for constructing the columns of the Jacobian matrix ${}^0 J_7$, are extracted from the transformation matrices ${}^0 T_i$.

$$
{}^0 T_i = \prod_{j=1}^{i} {}^{j-1} T_j = \left[\begin{array}{ccc|c} {}^0 \hat{X}_i & {}^0 \hat{Y}_i & {}^0 \hat{Z}_i & {}^0 O_i \\ \hline 0 & 0 & 0 & 1 \end{array} \right].
\tag{3.51}
$$

and the individual transformation matrices ${}^{i-1} T_i$ are computed by using Eq 3.6, 3.7 and 3.8.

3.3.2 Inverse differential kinematics

To control the robotic arm, the joints velocity $\dot{q}$ needs to be calculated from the velocity of the end effector V_E which involves the inverse differential kinematics problem. In the case of the redundant robotic arm, the direct Jacobian ${}^0 J_7$ is a non-squared 6x7 matrix, thus the pseudo-inverse ${}^0 J_7^*$ will be used instead of the inverse Jacobian which does not exist. The pseudo-inverse matrix which satisfies the Moore-Penrose condition (Siciliano & Khatib [2008]), is computed from :

$$
{}^0 J_7^* = {}^0 J_7^T ({}^0 J_7 \, {}^0 J_7^T)^{-1},
\tag{3.52}
$$

where ${}^0 J_7^T$ is the transpose of the direct Jacobian. The general solution for the inverse differential kinematics is :

$$
\dot{q} = {}^0 J_7^* \, V_E + {}^0 J_{7,null} \, \dot{q}_{opt},
\tag{3.53}
$$

where the vector $\dot{q}_{opt}$ is an arbitrary joint-space velocity and the matrix ${}^0 J_{7,null}$ is a squared 7x7 matrix, computed from:

$$
{}^0 J_{7,null} = (I - {}^0 J_7^* \, {}^0 J_7).
\tag{3.54}
$$

where I is the 7x7 identity matrix.

3.3.3   Redundancy exploitation

The first term in Eq 3.53 is a direct mapping from a desired velocity V_E of the end effector to a joints velocities vector $\dot{q}$ with minimum norm (Whitney [1972]) while the second term is a null-space velocity that can be added to the joints velocity vector $\dot{q}$ without changing the end effector velocity. Therefore, the nullspace is quite useful to exploit the dexterity of the arm for other tasks while the end effector is still kept moving with a desired velocity. The square 7x7 matrix $^0J_{7,null}$ enables the conversion of an arbitrary vector $\dot{q}_{opt}$ in joint-space to a nullspace velocity. The construction of the vector $\dot{q}_{opt}$ from criterion functions which need to be optimized for addition behaviors including the singularity avoidance, joints limits avoidance and real-time obstacle avoidance is dedicated in Chapter 4.

One of the advantages of the differential kinematics approach is the capability of increasing the dimension of the nullspace, based on the task which the manipulator needs to perform. During normal operations, i.e. the robotic arm is not in a singularity configuration, the Jacobian $^0J_7$ has a full rank of 6 when all six components of the end effector need to be controlled. Thus, the rank of the matrix $^0J_{7,null}$, i.e. the dimension of the nullspace, is equal to 1. For performing tasks, some of the six components of the velocity of the end effector are constrained. For instance, moving the center of the hand along a curve only requires three linear components of the end effector velocity to be controlled while three angular velocity components can be left floating. For tasks requiring less degrees of freedom, a modified Jacobian, formed by removing the respective rows associated with the uncontrolled velocity components from the Jacobian matrix, will be used instead. Thus, the rank of the matrix $^0J_{7,null}$ or the dimension of the nullspace is increased by the same number of uncontrolled velocity components.

3.3.4   Jacobian decomposition technique

This section allows to decompose the Jacobian matrix $^0J_7$ into three simpler matrices, which benefits the singularity analysis in the section 3.3.5. According to Dombre & Khalil

[2007], the Jacobian matrix will become simpler if it is represented in the kth reference frame with k - the integer number closest to the dividend of N - the number of links and 2. This makes sense because the Jacobian matrix is computed from N transformation matrices ^kT_i ($i = 1, .., N$) formed by multiplying $|k - i|$ matrices. If k is chosen to be equal to $N/2$, these transformation matrices will be in their simplest forms. By changing the reference frame from {0} to {3}, the Jacobian matrix $^0J_7$ is decomposed into two matrices as in the following equation:

$$^0J_7 = \left[\begin{array}{c|c} ^0R_3 & 0 \\ \hline 0 & ^0R_3 \end{array} \right] \, ^3J_7, \tag{3.55}$$

The matrix $^3J_7$ can be decomposed further by:

$$^3J_7 = \left[\begin{array}{c|ccc} & 0 & -L_z & L_y \\ I & L_z & 0 & -L_x \\ & L_y & L_x & 0 \\ \hline 0 & & I & \end{array} \right] \, ^3J_5 \tag{3.56}$$

where L_x, L_y, L_x are components of vector $^3L_{7,5}$. To calculate this vector, vector $^0L_{5,7}$ is extracted from the fourth column of the transformation matrix $^5T_7$ and is represented in reference frame {3} by using the rotation matrix $^3R_0$:

$$\begin{aligned} ^3L_{7,5} &= -^3R_0 \, ^0L_{5,7} \\ &= D_7 \begin{bmatrix} c_4c_5s_6 + c_6s_4 \\ s_5s_6 \\ c_5s_4s_6 - c_4c_6 \end{bmatrix}, \end{aligned} \tag{3.57}$$

The matrix $^3J_5$ is computed by the following equation:

$$^3J_5 = \begin{bmatrix} ^3Z_1 \times (^3O_5 - ^3O_1) & \cdots & ^3Z_7 \times (^3O_5 - ^3O_7) \\ ^3Z_1 & \cdots & ^3Z_7 \end{bmatrix}, \tag{3.58}$$

Because three z axes of reference frames {5}, {6} and {7} intersect themselves at one point, i.e. the origin of the reference frame {5} attaching to the Wrist, the matrix $^3J_5$ has a simple

structure of:

$$
{}^{3}J_5 = \begin{bmatrix} J_{11} & 0 \\ J_{21} & J_{22} \end{bmatrix},
\tag{3.59}
$$

where,

$$
J_{11} = \begin{bmatrix} -s_2 s_3 (D_3 + D_5 c_4) & -c_3 (D_3 + D_5 c_4) & 0 & -D_5 c_4 \\ -D_5 c_2 s_4 - c_3 s_2 (D_3 + D_5 c_4) & s_3 (D_3 + D_5 c_4) & -D_5 s_4 & 0 \\ -D_5 s_2 s_3 s_4 & -D_5 c_3 s_4 & 0 & -D_5 s_4 \end{bmatrix},
\tag{3.60}
$$

$$
J_{21} = \begin{bmatrix} c_3 s_2 & -s_3 & 0 & 0 \\ -s_2 s_3 & -c_3 & 0 & -1 \\ c_2 & 0 & 1 & 0 \end{bmatrix},
\tag{3.61}
$$

$$
J_{22} = \begin{bmatrix} -s_4 & c_4 s_5 & -c_6 s_4 - c_4 c_5 s_6 \\ 0 & -c_5 & -s_5 s_6 \\ c_4 & s_4 s_5 & c_4 c_6 - c_5 s_4 s_6 \end{bmatrix}.
\tag{3.62}
$$

In summary, the Jacobian matrix ${}^{0}J_7$ can be decomposed into three simple matrices:

$$
{}^{0}J_7 = \left[\begin{array}{c|c} {}^{0}R_3 & 0 \\ \hline 0 & {}^{0}R_3 \end{array} \right] \left[\begin{array}{c|ccc} & 0 & -L_z & L_y \\ I & L_z & 0 & -L_x \\ & L_y & L_x & 0 \\ \hline 0 & & I & \end{array} \right] {}^{3}J_5.
\tag{3.63}
$$

where ${}^{3}L_{7,5} = [L_x, L_y, L_z]^T$ and ${}^{3}J_5$ are determined by Eq 3.57 and 3.59, respectively.

3.3.5 Singularity analysis

The solution of the inverse differential kinematics, i.e. the mapping from a desired velocity V_E of the end effector to a joints velocities vector $\dot{q}$, exists only if the pseudo-inverse of the Jacobian (Eq 3.52) exists. Thus, sets of joints value $q = [\theta_1, \theta_2, \theta_3, \theta_4, \theta_5, \theta_6, \theta_7]^T$ that

satisfy the following equation, are singularity configurations:

$$\det({}^{0}J_7 \, {}^{0}J_7^{T}) = 0. \tag{3.64}$$

However, the Jacobian matrix ${}^{0}J_7$ can be decomposed into three simple matrices (Eq 3.63). The determinants of the first and the second matrix in Eq 3.63 are always different from 0 because of their structures. Therefore, the condition in Eq 3.64 becomes:

$$\det({}^{3}J_5 \, {}^{3}J_5^{T}) = 0. \tag{3.65}$$

Thus, singularities can be computed by using the simple matrix ${}^{3}J_5$ (Eq 3.59) instead of the complex ${}^{0}J_7$. The technique for singularity analysis that is used by Cheng et al. [1998], separates the singularity problem into the position singularities

$$det(J_{11} J_{11}^{T}) = 0, \tag{3.66}$$

and the orientation singularities

$$\det([J_{21} J_{22}][J_{21} J_{22}]^{T}) = 0. \tag{3.67}$$

However, Eq 3.67 is a strong condition which makes the method fail to detect all singularities. The following technique which allows to explore exhaustively all singularities of the redundant manipulator, is proposed.

The singularity configurations in Eq 3.65 makes the rank of the 6x7 matrix ${}^{3}J_5$ be lesser or equal to 5. This happens when the matrix ${}^{3}J_5$ loses the linear independence of one row or two columns. The conditions that meet this requirement are listed in the following table.

The condition 1 and 2 are the solution of Eq 3.66. To solve it, let denote the 3x4 matrix $J_{11} = [J_{11}^1 \ J_{11}^2 \ J_{11}^3 \ J_{11}^4]^T$ with J_{11}^i is the ith column vector of J_{11}. By using the Binet−Cauchy identity, Eq 3.66 becomes:

$$det(J_{11} J_{11}^{T}) = \sum_{i=1}^{4} M_{11,i}^2 = 0, \tag{3.68}$$

Table 3.2: Singularity conditions for the 7-DOF manipulator

Condition	Requirements
1	J_{11} loses the linear independence of 1 row
2	J_{11} loses the linear independence of 2 columns
3	J_{22} loses the linear independence of 1 row
4	J_{22} loses the linear independence of 2 columns
5	J_{22} and $[J_{11}\ J_{21}]^T$, each one loses the linear independence of 1 column

where $M_{11,1}, M_{11,2}, M_{11,3}, M_{11,4}$ are the determinants of 3x3 submatrices of J_{11}:

$$M_{11,1} = det([J_{11}^1\ J_{11}^2\ J_{11}^3]) = 0, \tag{3.69}$$

$$M_{11,2} = det([J_{11}^2\ J_{11}^3\ J_{11}^4]) = -D_3 D_5^2 c_3 s_4^2, \tag{3.70}$$

$$M_{11,3} = det([J_{11}^3\ J_{11}^4\ J_{11}^1]) = -D_3 D_5^2 s_2 s_3 s_4^2, \tag{3.71}$$

$$M_{11,4} = det([J_{11}^4\ J_{11}^1\ J_{11}^2]) = D_3 D_5 s_4 (D_3 s_2 + D_5 s_2 c_4 + D_5 s_4 c_2 c_3). \tag{3.72}$$

Thus, singularities are configurations that make all four determinants be zero simultaneously (Table 3.3). The combined condition is:

$$s_4 = 0, \tag{3.73}$$

$$s_2 = 0 \wedge c_3 = 0. \tag{3.74}$$

By considering the 3x3 matrix J_{22}, the condition

$$s_6 = 0 \wedge c_5 = 0. \tag{3.75}$$

makes it lose the linear independence of 1 row, thus leads to singularities while the condition $s_6 = 0$ makes it lose the linear independence of 1 column. Therefore, the joints

Table 3.3: Rank-deficient conditions of J_{11}

Condition	Solution
$M_{11_1} = 0$	any configuration
$M_{11_2} = 0$	$s_4 = 0 \vee c_3 = 0$
$M_{11_3} = 0$	$s_4 = 0 \vee s_3 = 0 \vee s_2 = 0$
$M_{11_4} = 0$	$s_4 = 0 \vee D_3 s_2 + D_5 s_2 c_4 + D_5 s_4 c_2 c_3 = 0$

configurations make the matrix $[J_{11} \ J_{21}]^T$ lose the linear independence of 1 column, are the last singularities. Let us consider the matrix J_{21}:

$$\det(J_{21} J_{21}^T) = \sum_{i=1}^{4} M_{21,i}^2 = 0, \tag{3.76}$$

where $M_{21,1}, M_{21,2}, M_{21,3}, M_{21,4}$ are the determinants of 3x3 submatrices of J_{21}:

$$M_{21,1} = \det([J_{21}^1 \ J_{21}^2 \ J_{21}^3]) = -s_2, \tag{3.77}$$

$$M_{21,2} = \det([J_{21}^2 \ J_{21}^3 \ J_{21}^4]) = -s_3, \tag{3.78}$$

$$M_{21,3} = \det([J_{21}^3 \ J_{21}^4 \ J_{21}^1]) = c_3 s_2, \tag{3.79}$$

$$M_{21,4} = \det([J_{21}^4 \ J_{21}^1 \ J_{21}^2]) = s_3 c_2. \tag{3.80}$$

The condition 5 in Table 3.2 requires submatrices of J_{11} and J_{21} be rank-deficient in pairs as listed in Table 3.4. The combined condition is

$$s_6 = 0 \wedge s_2 = 0. \tag{3.81}$$

By taking into account of joint limits in Table 2.2, all singularities of the 7-DOF manipulator in the 6D taskspace (Eq 3.73, 3.75, 3.81) are listed in Table 3.5.

In fact, the number of singularities depends on the dimension of the taskspace, i.e. a joint configuration is a singularity for tasks requiring 6 degrees of freedom but it may

Table 3.4: Rank-deficient conditions for submatrices of J_{11} and J_{21}

Condition	Condition for J_{11}	Condition for J_{21}
$M_{11,1} = M_{21,1} = 0$	Any configuration	$s_2 = 0$
$M_{11,2} = M_{21,2} = 0$	$c_3 = 0$	$s_2 = 0$
$M_{11,3} = M_{21,3} = 0$	$s_3 = 0$ or $s_2 = 0$	$c_3 = 0$ or $s_2 = 0$
$M_{11,4} = M_{21,4} = 0$	$L_3 s_2 + L_5 s_2 c_4 + L_5 s_4 c_2 c_3 = 0$	$s_3 = 0$ or $c_2 = 0$

Table 3.5: All singularities in 6D task-space

Singularity	Condition	Value of joints (degree)
1	$s_4 = 0$	$\theta_4 = 0$
2	$c_3 = 0;\ s_2 = 0$	$\theta_3 = 90;\ \theta_2 = 0$
3	$c_3 = 0;\ s_2 = 0$	$\theta_3 = -90;\ \theta_2 = 0$
4	$s_6 = 0;\ c_5 = 0$	$\theta_6 = 0;\ \theta_5 = 90$
5	$s_6 = 0;\ c_5 = 0$	$\theta_6 = 0;\ \theta_5 = -90$
6	$s_6 = 0;\ s_2 = 0$	$\theta_6 = 0;\ \theta_2 = 0$

be not for the tasks requiring less degree of freedom. Singularities for tasks requiring less degree of freedom are a subset of 6D taskspace singularities. The singularity analysis allows us to acknowledge all singularities of the 7-DOF manipulator which is necessary before applying the differential kinematics approach for controlling the velocity of the end effector. The manipulator is not supposed to start its movements in these singularity configurations because excessive joint velocities may damage the robotic arm. The singularity avoidance during tasks is implemented in Chapter 4.

Chapter 4

Control of a 7-DOF anthropomorphic robotic arm in velocity-constrained tasks with real-time obstacle avoidance

4.1 Introduction

Redundant anthropomorphic robotic arms with seven degrees of freedom (DOF), possessing more dexterity to perform complex movements, have become very popular, especially within the field of service robotics. In the effort of imitating the structure of human arms with three DOF in the shoulder, one DOF in the elbow and three DOF in the wrist, these robotic arms are expected to operate safely in dynamic environments. For instance, in applications such as tracking, grasping a mobile object or moving the end effector with desired velocity profiles, the end effector needs to move at an equal or higher velocity to keep up with the moving target. In the case of using control strategies which allow the end effector to move from position to position by generating trajectories, such as motion planning, changes in the target's position or its moving direction will most likely result in recalculating trajectories. Therefore, in such dynamic target applications, these control

strategies become inadequate because of the high computational burden and also lack of flexibility. Adequate control strategies must be able to control the velocity of the end effector in a flexible way while ensuring the safety of the robotic arm, for instance, the joints should not exceed their physical limits in term of position, velocity and also acceleration.

Figure 4.1: An application of tracking and grasping a mobile object in a dynamic obstacle environment with the experimental Anthropomorphic Robotic System - ARoS

The control of anthropomorphic robotic arms faces more challenges in dynamic obstacle environments. While the end effector moves with a desired velocity, the challenge is keeping the links of robotic arms free from collisions with mobile obstacles. Moreover, sudden appearance or disappearance of obstacles in the workspace may result in undesired reactions of the robotic arm if the adopted control strategy is not prepared for these situations.

This chapter contributes with a solution that enables the control of a 7-DOF anthropomorphic robotic arm in such dynamic environments (e.g. Figure 4.1), using a differential kinematics approach. The 7-DOF anthropomorphic manipulator is a Light Weight Arm 7DOF from AMTEC Robotics/Schunk^{TM}, which is equipped on the robot ARoS

(Section 2.1) and studied in the previous Chapter 3.

4.2   Related Work

In kinematics approaches that allow the end effector to move from point to point, the position and orientation of the end effector must be specified to solve the inverse kinematics problems for joint values. For redundancy resolution, another parameter needs to be introduced to select a suitable configuration of the arm among infinite number of solutions, for instance, the Swivel angle (or Arm plane angle) for changing the position of the elbow ([Tarokh & Kim, 2007, Tolani et al., 2000]). The desired position of joints can also be obtained with an analytical solution, taking account of joint limits ([Shimizu et al., 2008]). The trajectories can be generated and optimized through motion planning ([Costa e Silva et al., 2011]). This approach allows robotic arms to avoid obstacles in the workspace and also ensures the values of joints are within their limits, thus achieving higher safety during movements. However, in dynamic environments with mobile targets and mobile obstacles, recalculating trajectories makes motion planing approaches become inadequate because of the high computational burden and also lack of flexibility.

Redundant robotic arms can be controlled by using a dynamical system approach ([Iossifidis & Schoner, 2009]). Changing the Arm plane angle enables the obstacle avoidance from the shoulder to the wrist. By imposing the hand aligned with the tangent to the end effector path, the obstacle avoidance from the wrist to the end effector is achieved. The joint limits are avoided locally by changing the value of the Arm plane angle, which may lead to infeasible solution when the end effector tries to avoid obstacles.

The velocity of the end effector can be controlled directly by using differential kinematics. The solution from pseudo-inverse Jacobian method minimizes the norm of joint velocities for achieving a desired velocity of the end effector ([Siciliano & Khatib, 2008]). Moreover, this approach will give more flexibility in controlling the velocity of the end effector since it allows to control only velocity components which are required for the

task. For instance, moving the center of the hand along a curve requires three linear velocity components to be constrained while three angular velocity components can be left floating. The pseudo-inverse Jacobian matrix which transforms an end effector velocity vector to a joint velocity vector, enables the control of robotic arms in 6D task-space. For tasks requiring less degrees of freedom, a modified Jacobian, formed by removing the respective rows associated with the uncontrolled velocity components from the Jacobian matrix before the calculation of the pseudo-inverse Jacobian matrix, will be used instead. Thus, robotic arms will have more flexibility to ensure the safety during movements such as avoiding joint limits and obstacles.

In differential kinematics, redundancy can be resolved by specifying both velocities of the hand and the changing rate of the Arm plane angle, then constructing the augmented Jacobian for mapping these velocities into joint velocities ([Seraji et al., 1993]). The limitation of this approach is that only the elbow is kept away from obstacles by increasing the Arm plane angle. The artificial potential field approach, where virtual forces from obstacles are transformed into torques by the statics relation ([Khatib, 1986]), can achieve the obstacle avoidance behavior but this method has computational burdens. Another approach is by using a performance criterion for maximizing the minimum distance from the obstacle to links ([Liu et al., 2008]), but this method is limited to some pre-defined models including spheres and column obstacles. Obstacles can be avoided by determining control points in the robotic arm and their velocities in order to move them away from obstacles, using the Jacobian transpose method. But this method is only suitable for applications that do not require accurate movements of the end effector ([Lee & Buss, 2007]). Joint limits avoidance can be implemented, for instance, by using the pseudo-inverse Jacobian and a criterion function that characterizes the distance of the current joint values to the middle of the joint limits range ([Wang et al., 2010]) but the method has not addressed the joint velocity limits problem.

Therefore, the objective of this chapter is to flexibly control the velocity of the end effector by using a differential kinematics approach, while ensuring the safety of the robotic

arm from exceeding the joints' physical limits in terms of position, velocity and also acceleration. A real-time obstacle avoidance strategy for controlling a 7-DOF anthropomorphic robotic arm in dynamic environments, taking account of sudden appearances or disappearances of mobile obstacles, is also developed.

4.3 Velocity control of a 7-DOF anthropomorphic robotic arm

To control the robotic arm, the velocity of joints $\dot{q}$ needs to be calculated from the velocity of the end effector V_E which involves the inverse differential kinematics problem. The solution, given by the first term in Eq.3.53, is a direct mapping from a desired velocity V_E of the end effector to a joints velocity vector $\dot{q}$ with minimum norm. The second term is a nullspace velocity that can be added to the joints velocity vector $\dot{q}$ without changing the end effector velocity. This term is useful to exploit the dexterity of the arm for other tasks while the end effector is still kept moving with a desired velocity. The total joints velocity for moving the end effector with a desired velocity, V_E, while keeping joints from their physical limits and singularities is:

$$\dot{q} = \dot{q}_{need} + \dot{q}_{jlim} + \dot{q}_{sing}, \tag{4.1}$$

where $\dot{q}_{need}$ is the first term in Eq 3.53, $\dot{q}_{jlim}$ and $\dot{q}_{sing}$ are nullspace joint velocity vectors for avoiding joint limits and singularities, respectively.

$$\dot{q}_{jlim} = \alpha_{jlim} \cdot {}^0J_{7,null} \, \nabla \xi_{jlim,mod}, \tag{4.2}$$

$$\dot{q}_{sing} = \alpha_{sing} \cdot {}^0J_{7,null} \, \nabla \mu. \tag{4.3}$$

where ${}^0J_{7,null}$ is the nullspace matrix, defined in Eq 3.54.

By using the gradient projection method (see, e.g. [Dombre & Khalil, 2007], [Liu et al., 2010]), in order to avoid the physical position limits of joints, the distance of the

current joint values to the middle of the joints' limit ranges is chosen as a criterion function that needs to be minimized:

$$\xi_{jlim} = \frac{1}{2} \sum_{i=0}^{7} \left(\frac{\theta_i - \theta_{i,mid}}{\theta_{i,max} - \theta_{i,min}} \right)^2,\tag{4.4}$$

where $\theta_{i,min}$, $\theta_{i,max}$ and $\theta_{i,mid}$ are the minimum, maximum and middle value of the ith joint range. The gradient of the criterion function $\nabla \xi_{jlim} = \begin{bmatrix} \frac{\partial \xi_{jlim}}{\partial \theta_1} & \cdots & \frac{\partial \xi_{jlim}}{\partial \theta_7} \end{bmatrix}^T$ is computed from the following equation:

$$\frac{\partial \xi_{jlim}}{\partial \theta_i} = \frac{\theta_i - \theta_{i,mid}}{\theta_{i,max} - \theta_{i,min}},\tag{4.5}$$

For better performance in the joint limits avoidance, the modified gradient of the criterion function is proposed.

$$\frac{\partial \xi_{jlim,mod}}{\partial \theta_i} = \frac{\partial \xi_{jlim}}{\partial \theta_i} \left(1 + \exp\left(\frac{\frac{\partial \xi_{jlim}}{\partial \theta_i} - K_{j1}}{K_{j2}} \right) \right).\tag{4.6}$$

The value of the modified coefficient is almost equal to 1 when the criterion gradient is small. However, when the criterion gradient becomes high, i.e. the joint is near its
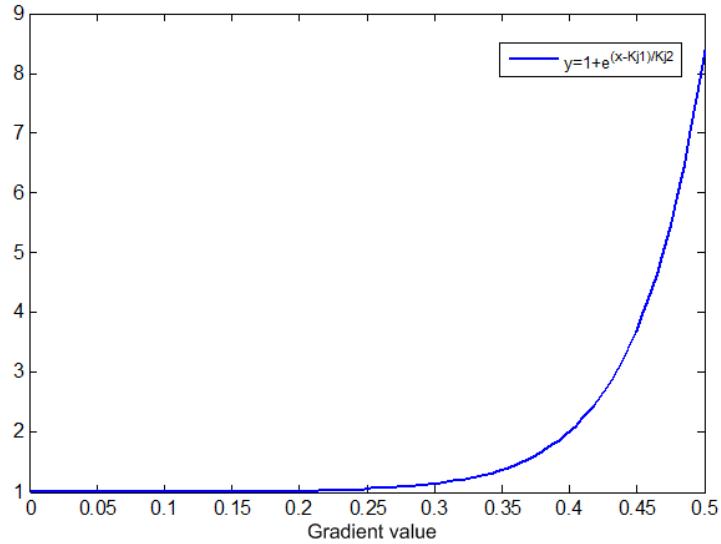
Figure 4.2: The modified coefficient for gradients of the joint limits criterion function (see Eq 4.6 with $K_{j1} = 0.4$, $K_{j2} = 0.05$)

physical position limits, the modified gradient is amplified so that more effort is spent for ensuring the joint staying in its ranges (Figure 4.2). The coefficient K_{j1} is used to control the threshold when the modified gradient begins to increase quickly and K_{j2} is used to control the increasing rate.
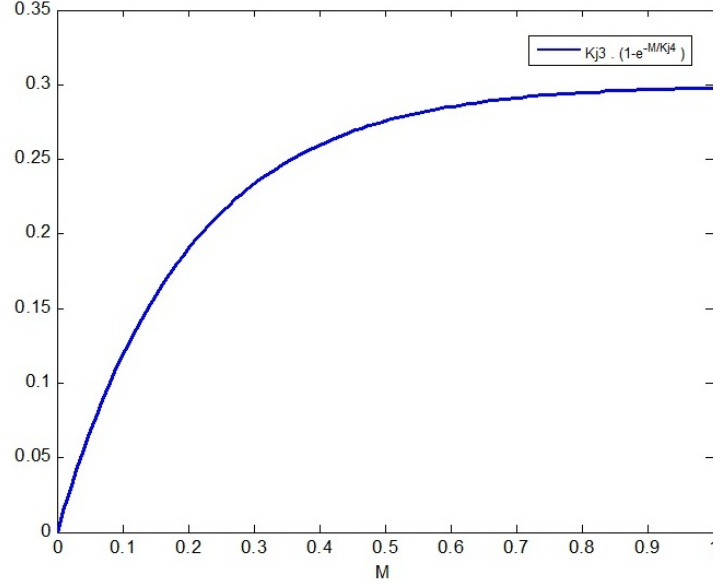
Figure 4.3: Ensuring the nullspace joint velocities from exceeding their limits (see Eq 4.7 with $K_{j3} = 0.3$, $K_{j4} = 0.2$)

The coefficient α_{jlim} (Eq 4.2) is chosen negative to minimize the criterion function and acts like a scaling coefficient to ensure that joints do not exceed their physical velocity limits:

$$\alpha_{jlim} = -\frac{K_{j3}(1 - \exp\left(-M_{jlim}/K_{j4}\right)}{M_{jlim} + \epsilon}, \tag{4.7}$$

where M_{jlim} is the maximum value of the nullspace joint velocities

$$M_{jlim} = max(\,^0 J_{7,null} \, \nabla \xi_{jlim,mod}). \tag{4.8}$$

and the coefficient K_{j3} relates to the maximum allowed nullspace velocity (Figure 4.3). For instance, K_{j3} can be the minimum of the joints' maximum allowed velocities. The coefficient K_{j4} is used to control the increasing rate of α_{jlim} and ϵ is a small positive value

to overcome the situation when $M_{jlim} = 0$. The problem of joint physical acceleration limits which occurs when obstacles appear or disappear suddenly, is solved in Section 4.4.

The singularities avoidance behavior can be implemented by using the manipulability measure that characterizes the distance from singularities ([Siciliano & Khatib, 2008]).

$$\mu = \sqrt{\det({}^0J_7\,{}^0J_7{}^T)}, \tag{4.9}$$

The gradient of the manipulability measure $\nabla\mu = \begin{bmatrix} \frac{\partial\mu}{\partial\theta_1} & \cdots & \frac{\partial\mu}{\partial\theta_7} \end{bmatrix}^T$ is computed by the finite difference numerical method.

$$\frac{\partial\mu}{\partial\theta_i} = \frac{\mu(\theta_i + \Delta\theta_i) - \mu(\theta_i)}{\Delta\theta_i}. \tag{4.10}$$

The coefficient α_{sing} (Eq 4.3) is chosen positive to maximize the manipulability measure, i.e. the distance to singularities. The same strategy as in joint limits avoidance is used to ensure the nullspace joint velocities from exceeding their limits.

$$\alpha_{sing} = \frac{K_{s1}\left(1 - \exp\left(-M_{sing}/K_{s2}\right)\right)}{M_{sing} + \epsilon}, \tag{4.11}$$

where M_{sing} is the maximum value of the nullspace joints velocities

$$M_{sing} = max({}^0J_{7,null}\,\nabla\mu). \tag{4.12}$$

and the coefficient K_{s1} relates to the maximum allowed nullspace velocity and the coefficient K_{s2} is used to control the increasing rate of α_{sing} and ϵ is a small value to overcome the situation when $M_{sing} = 0$.

Figure 4.4 depicts a scenario showing how the redundant robotic arm benefits from both of the joint limits and singularities avoidance behaviors in a task requiring six degrees of freedom. The initial joint configuration is $q = [0^0, -10^0, 100^0, -90^0, -60^0, 120^0, 40^0]^T$ and the hand of the robot needs to move in the negative direction of the x_0 axis of the base reference frame {0} at the velocity 20 mm/s while maintaining the position in y_0, z_0 axis and also its orientation (Figure 4.4-C). Without any behavior implemented, the arm
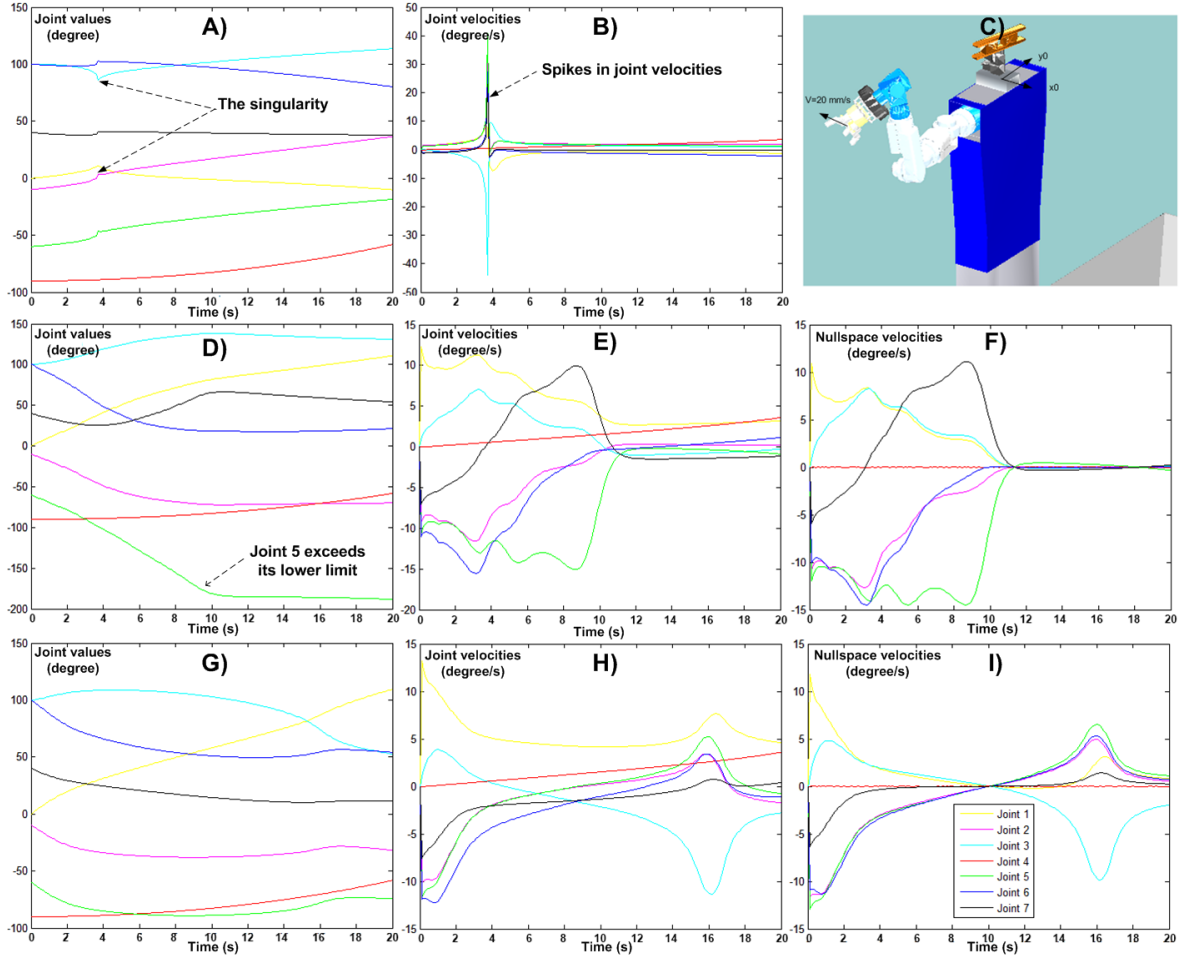
Figure 4.4: The scenario shows the effectiveness of the joint limits and singularities avoidance behaviors: Without any behaviors, the arm crosses the singularity $\{\theta_2 = 0 \wedge \theta_3 = 90^0\}$ with spikes in joint velocities (A,B). By using the singularities avoidance behavior, the manipulator passes the singularity successfully but Joint 5, θ_5, exceeds its lower limit (D,E,F). The robotic arm overcomes the singularity successfully and also keeps its joints in their limits by integrating the two behaviors (G,H,I).

crosses the singularity $\{\theta_2 = 0 \wedge \theta_3 = 90^0\}$ during the task and the spikes in joint velocities occur (Figure 4.4-A,B). By using the singularities avoidance behavior (Figure 4.4-D,E,F), the robotic arm passes the singularity successfully but Joint 5, θ_5, exceeds its lower limit (-165^0). With the integration of the two behaviors, the robotic arm overcomes the singularity successfully and also keeps its joints in their limits (Figure 4.4-G,H,I).

4.4 Real-time obstacle avoidance

The proposed obstacle avoidance strategy is depicted in Fig.4.5. The mobile segments of the anthropomorphic robotic arm, i.e. the Shoulder-Elbow, the Elbow-Wrist and the Wrist-Hand should be kept away from collisions with obstacles. To improve the obstacle avoidance performance, especially when the robotic arm needs to avoid a surface or a plane, the Elbow and the Wrist are also taken into account. The Shoulder is fixed to the trunk and the Hand moves with a desired velocity V_E, defined by the task that the manipulator is performing. Thus they are excluded from the obstacle avoidance behavior.
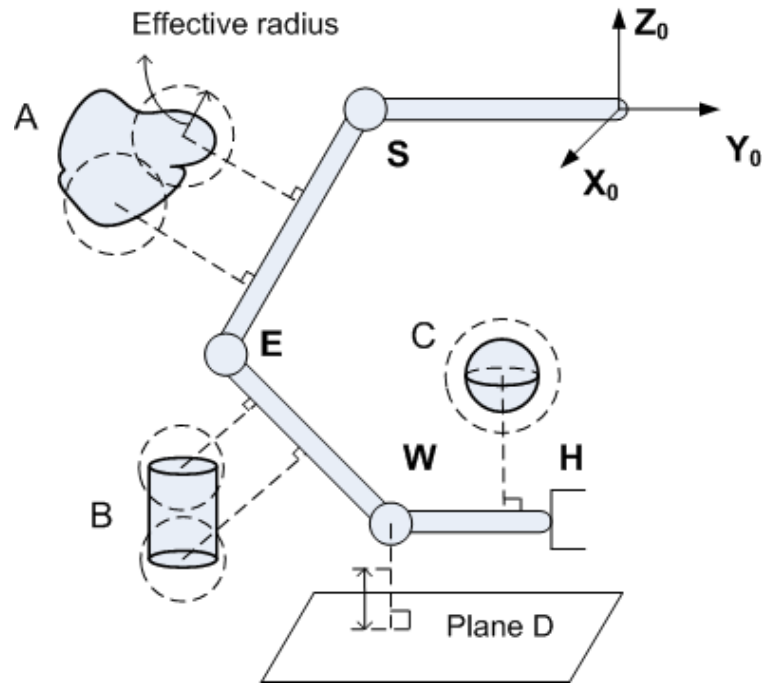
Figure 4.5: The anthropomorphic robotic arm and obstacles

Therefore, the nullspace joint velocity vector $\dot{q}_{obs}$ for obstacle avoidance, which can be added to the total joints velocity (Eq 4.1) without changing the desired velocity of the end effector, is computed from:

$$\dot{q}_{obs} = \dot{q}_{obs,SE} + \dot{q}_{obs,EW} + \dot{q}_{obs,WH} + \dot{q}_{obs,E} + \dot{q}_{obs,W},\tag{4.13}$$

Each individual component is calculated from the general expression:

$$\dot{q}_{obs,k} = \alpha_{obs,k} \cdot {}^0J_{7,null} \cdot \nabla \xi_k. \tag{4.14}$$

where k is a notation of SE, EW, WH, E, W segments, and the matrix ${}^0J_{7,null}$ is given by Eq 3.54. The coefficients $\alpha_{obs,k}$ act like scaling coefficients to ensure that all joints do not exceed their physical velocity limits. The values of the coefficients $\alpha_{obs,k}$ are determined in the same approach as in Eq 4.7.

From the fact that obstacles may have different sizes and shapes, modeling obstacles is limited to some well-defined models, such as spheres and columns obstacles ([Liu et al., 2008]) or line obstacles ([Lee & Buss, 2007]), and calculating the minimum distance from obstacles requires extra computational resources. By choosing some points near the boundary of obstacles and specifying an "effective radius" to cover each part of obstacles, the proposed method can deal with many obstacles with higher computational efficiency.

The individual performance criteria ξ_k that characterize distances from obstacles to the segment k of the robotic arm, are chosen as:

$$\xi_k = \sum_{j=1}^{N} \xi_{k,j}, \tag{4.15}$$

where

$$\xi_{k,j} = \frac{1}{K_{off} + d_{j,k} - R_j}. \tag{4.16}$$

with $d_{j,k}$ is the distance from the center of the jth obstacle to the kth arm segment, R_j is the effective radius of the obstacle, and the constant coefficient K_{off} is used to stabilize the performance criterion, acting as a safe distance when the robotic arm approaches obstacles. The reciprocals of distances are chosen as performance criteria for the purpose of gradients from obstacle distance criteria increase faster when the robotic arm gets closer to them. The coefficients $\alpha_{obs,k}$ (Eq 4.14) are chosen negative to minimize the performance criteria, i.e. the reciprocals of distances from obstacles.

Let us consider the scenario depicted in Figure 4.6, where the distance from the obstacle j to the Shoulder-Elbow segment needs to be computed. The area of the triangle
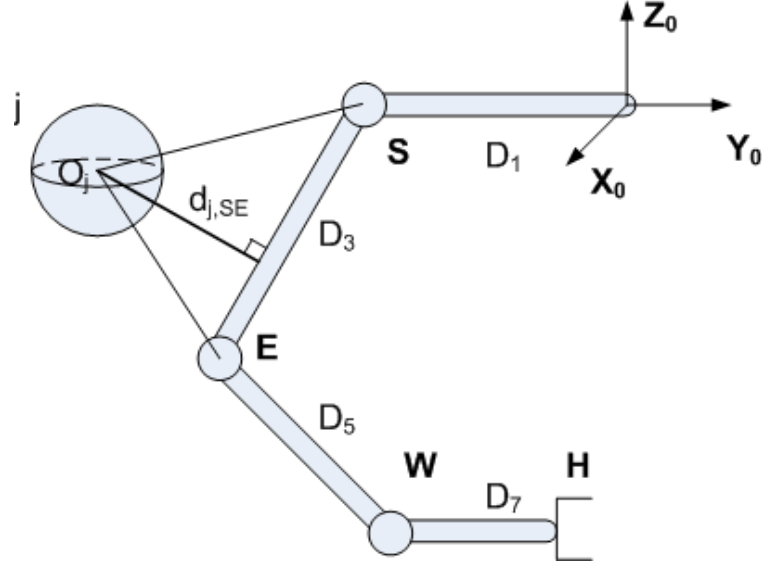
Figure 4.6: The distance from the obstacle j to the segment SE

$O_j SE$ is computed from:

$$S_{O_j SE} = \frac{\left\|\vec{SO_j}\right\| \cdot \left\|\vec{SE}\right\| \cdot sin(\widehat{O_j SE})}{2},$$

(4.17)

and the cosine theorem gives:

$$\vec{SO_j} \cdot \vec{SE} = \left\|\vec{SO_j}\right\| \cdot \left\|\vec{SE}\right\| \cdot cos(\widehat{O_j SE}),$$

(4.18)

Thus, the distance from the obstacle j to the segment Shoulder-Elbow can be computed by:

$$d_{j,SE}^2 = \frac{4S_{O_j SE}^2}{\left\|\vec{SE}\right\|} = \left\|\vec{SO_j}\right\|^2 - \frac{(\vec{SO_j} \cdot \vec{SE})^2}{D_3^2},$$

(4.19)

or written in matrix form:

$$d_{j,SE}^2 = (O_j - S)^T (O_j - S) - \frac{((O_j - S)^T (E - S))^2}{D_3^2}.$$

(4.20)

Similarly, the distances from the obstacle j to other segments are:

$$d_{j,EW}^2 = \|O_j - E\|^2 - \frac{((O_j - E)^T (W - E))^2}{D_5^2}.$$

(4.21)

$$d_{j,WH}^2 = \|O_j - H\|^2 - \frac{((O_j - H)^T (W - H))^2}{D_7^2}. \tag{4.22}$$

$$d_{j,E}^2 = (O_j - E)^T (O_j - E). \tag{4.23}$$

$$d_{j,W}^2 = (O_j - W)^T (O_j - W). \tag{4.24}$$

where O_j is the coordinate of the obstacle j and S, E, W, H are the coordinates of the Shoulder, Elbow, Wrist and Hand, extracted from the transformation matrices $^0T_1$, $^0T_3$, $^0T_5$, $^0T_7$ respectively (Eq.3.51).

In order to calculate the gradient of individual performance criteria ξ_k (Eq 4.15), the gradient of the performance criterion $\xi_{k,j}$ is computed by:

$$\nabla \xi_{k,j} = \frac{-\nabla d_{j,k}}{(K_{off} + d_{j,k} - R_j)^2} = \frac{-\nabla (d_{j,k}^2)}{2\, d_{j,k} (K_{off} + d_{j,k} - R_j)^2}, \tag{4.25}$$

where the squared distance from the jth obstacle to the kth segment of the robotic arm (Eq 4.20, 4.21, 4.22, 4.23 and 4.24) has its gradient $\nabla(d_{j,k}^2) = \left[\frac{\partial(d_{j,k}^2)}{\partial \theta_1} \quad \cdots \quad \frac{\partial(d_{j,k}^2)}{\partial \theta_7} \right]$ given by the following equations.

For the Shoulder-Elbow segment,

$$\nabla(d_{j,SE}^2) = -\frac{2(O_j - S)^T (E - S)}{L_3^2} \left((O_j - S)^T \nabla E \right), \tag{4.26}$$

For the Elbow-Wrist segment,

$$\nabla(d_{j,EW}^2) = -2(O_j - E)^T \nabla E$$
$$- \frac{2(O_j - E)^T (W - E)}{L_5^2} \left((O_j - E)^T (\nabla W - \nabla E) - (W - E)^T \nabla E \right), \tag{4.27}$$

For the Wrist-Hand segment,

$$\nabla(d_{j,WH}^2) = -\frac{2(O_j - H)^T (W - H)}{L_7^2} \left((O_j - H)^T \nabla W \right), \tag{4.28}$$

For the Elbow,

$$\nabla(d_{j,E}^2) = -2(O_j - E)^T \nabla E, \tag{4.29}$$

For the Wrist,

$$\nabla(d_{j,W}^2) = -2(O_j - W)^T \, \nabla W. \tag{4.30}$$

where O_j is the coordinate of the obstacle j and S, E, W, H are the coordinates of the Shoulder, the Elbow, the Wrist and the Hand. The gradient of the Elbow coordinates $\nabla E = \begin{bmatrix} \frac{\partial E}{\partial \theta_1} & \cdots & \frac{\partial E}{\partial \theta_7} \end{bmatrix}$ are calculated by the finite difference numerical method.

$$\frac{\partial E}{\partial \theta_i} = \frac{E(\theta_i + \Delta \theta_i) - E(\theta_i)}{\Delta \theta_i}. \tag{4.31}$$

The gradient of the Wrist is also computed in the same way. Because the Shoulder is fixed in the base reference frame and the Hand is constrained by the performing task, the gradients of their coordinates are equal to zero and do not appear in the gradients of performance criteria.

A coefficient is used to modify the gradients of performance criteria (Eq 4.25), taking account of the range that the robotic arm begins to avoid obstacles:

$$\nabla \xi_{k,j,mod} = \nabla \xi_{k,j} \, K_{r1} / \left(1 + \exp \left(\frac{K_{off} + d_{j,k} - R_j}{K_{r2}} \right) \right). \tag{4.32}$$

where R_j is the effective radius of the ith obstacle and K_{off} is an offset, acting like a safe distance. The coefficient K_{r1} is used to control the maximum value of the modified gradient while K_{r2} is used to control the transition slope when the obstacle approaches the kth links of the manipulator (Figure 4.7).

Because only coordinates of the Shoulder, the Elbow, the Wrist and the Hand are used and most of the terms are repeated in the calculations of performance criteria gradients, the proposed method allows to generate quickly the individual obstacle avoidance criteria ξ_k, from an array of obstacles coordinates, making the method suitable for real-time applications.

In real-time obstacle avoidance applications, the sudden appearance or disappearance of obstacles produces spikes in the joint velocity values, which may stop the robotic arm because of the limitations in the maximum acceleration of joints. Moreover, the coordinate values of objects, acquired from the vision system, always contain noises because
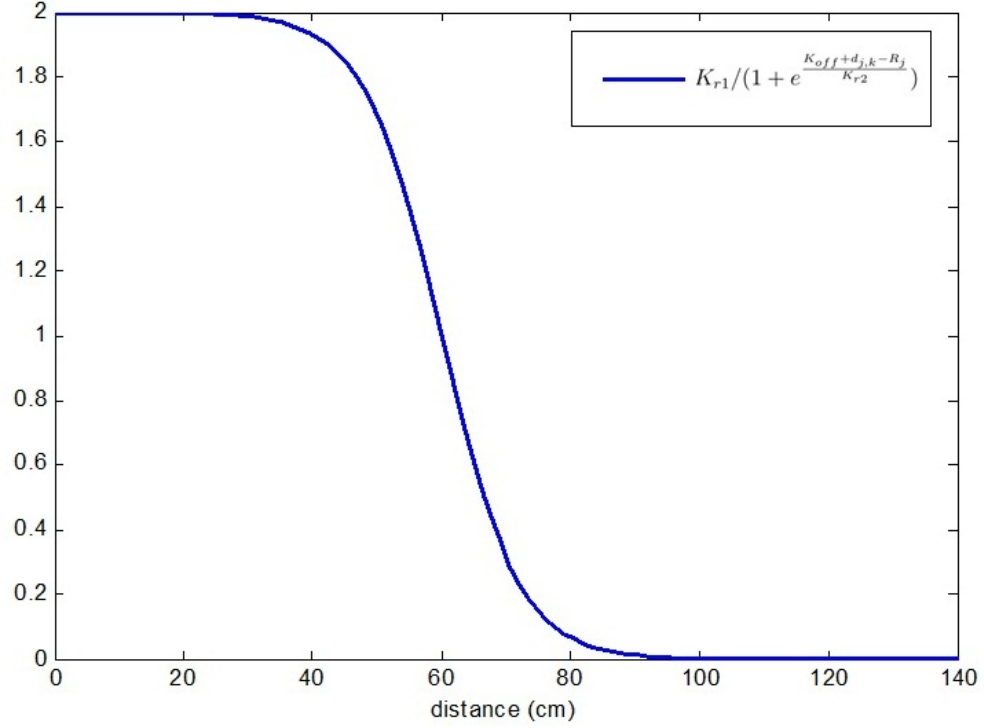
Figure 4.7: Modification of the distance criteria gradients for taking account of the range that the robotic arm begins to avoid obstacles (Eq 4.32 with $K_{r1} = 2$, $K_{off} = 70$, $R_j = 10$ and $K_{r2} = 6$).

of the imperfection of vision systems. This problem makes the robotic arm to vibrate in the presence of obstacles. These problems are demonstrated in the following simulation scenario (Figure 4.8). The robotic arm needs to draw an ellipse on a horizontal plane, i.e. parallel to the XY plane of the base reference frame. The ellipse has the dimension of 300mm along the Y axis and 200mm along the X axis. The initial position of the end effector was (500,-400,-400)mm with respect to the base reference frame. A velocity profile has been defined by differentiating the equation of the ellipse and the end effector would track an imaginary object moving with that velocity profile. In this task, only three linear velocities of the end effector need to be controlled:

$$V_E = [40\cos(0.2t - \pi/2) \ -60\sin(0.2t - \pi/2) \ 0]^T. \tag{4.33}$$

The time for accomplishing the task is 31.14s. An obstacle appears at the coordinates
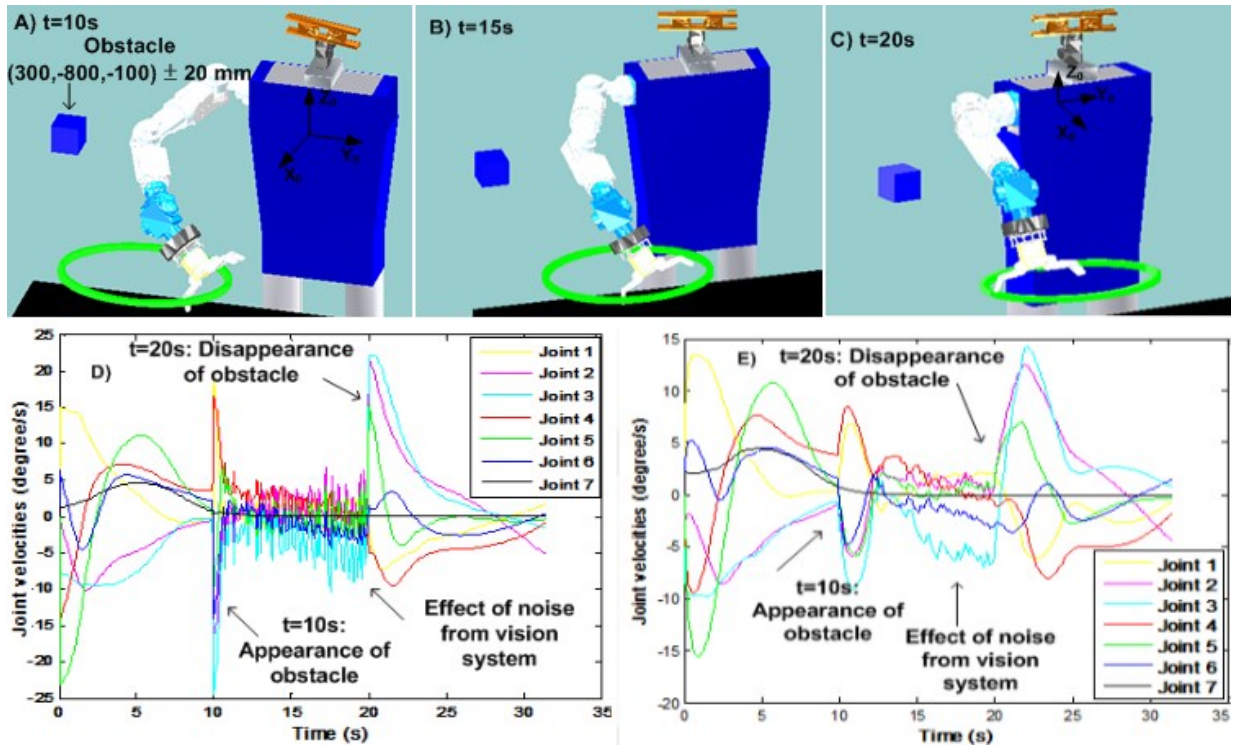
Figure 4.8: The simulation scenario which the robotic arm needs to track an ellipse while avoiding an obstacle that appears at t=10s and vanishes at t=20s: A) t=10s B) t=15s C) t=20s D) Joint velocities without a dynamic filter E) Joint velocities when a dynamic low-pass filter is used

of (300,-800,-100) mm at t=10s and disappears at t=20s. The imperfection of the vision system is simulated by a random noise in obstacle coordinates with maximum value of 20mm. Figure 4.8D illustrates the effect of the sudden appearance, disappearance of obstacles and the imperfection of the vision system on the joint velocities of the robotic arm.

The proposed control strategy for these problems is to smooth the gradients of performance criteria before converting them to a nullspace joints velocity because the nullspace velocities can not be smoothed directly unless the velocity of the end effector changes. The smoothing can be done by using a low-pass filter. However, using a filter will slow down the response of the robotic arm continuously and this problem may lead to a failure in obstacle avoidance. Therefore, the proposed approach is to use a dynamic

filter on the gradients of the individual obstacle avoidance criteria (Eq 4.15 and 4.25)

$$\nabla\xi_{k,fil}(t) = \beta_f\nabla\xi_k(t) + (1-\beta_f)\nabla\xi_{k,fil}(t-\Delta t), \tag{4.34}$$

where the filtering coefficient β_f is computed from:

$$\beta_f = \frac{\Delta t}{\Delta t + K_f}, \tag{4.35}$$

This low-pass filter with the cutoff frequency $f = 1/(2\pi K_f)$ becomes dynamic when the value of the coefficient K_f can adapt to the gradient of the performance criteria:

$$K_f = K_{f1}\left(1 - \exp\left(-M_f/K_{f2}\right)\right), \tag{4.36}$$

where M_f is the maximum difference between the old gradient and the current gradient:

$$M_f = max(|\nabla\xi_k(t) - \nabla\xi_{k,fil}(t-\Delta t)|). \tag{4.37}$$

The coefficient K_{f1} controls the maximum value of K_f and K_{f2} adjusts the effect of M_f on K_f. When the gradient variation of the performance criteria increases, the cutoff frequency will decrease because of the rising of K_f. Thus, the filtering effect becomes stronger when an obstacle appears or vanishes suddenly. Figure 4.8-E shows the efficiency of the method when facing the problem of sudden appearance, disappearance of obstacles and the imperfection of the vision system.

4.5 Experiments

This section presents experiments with the real robotic platform, performing tasks in dynamic environments. The control of the 7-DOF anthropomorphic robotic arm is challenged in two tasks. Figure 4.9 depicts the first task which requires the robotic arm to track a mobile target (the green object), grasp, and drop it in a target location (the red box) while avoiding obstacles (magenta objects) that may eventually appear and disappear in the workspace. The information about the object coordinates is given in real-time
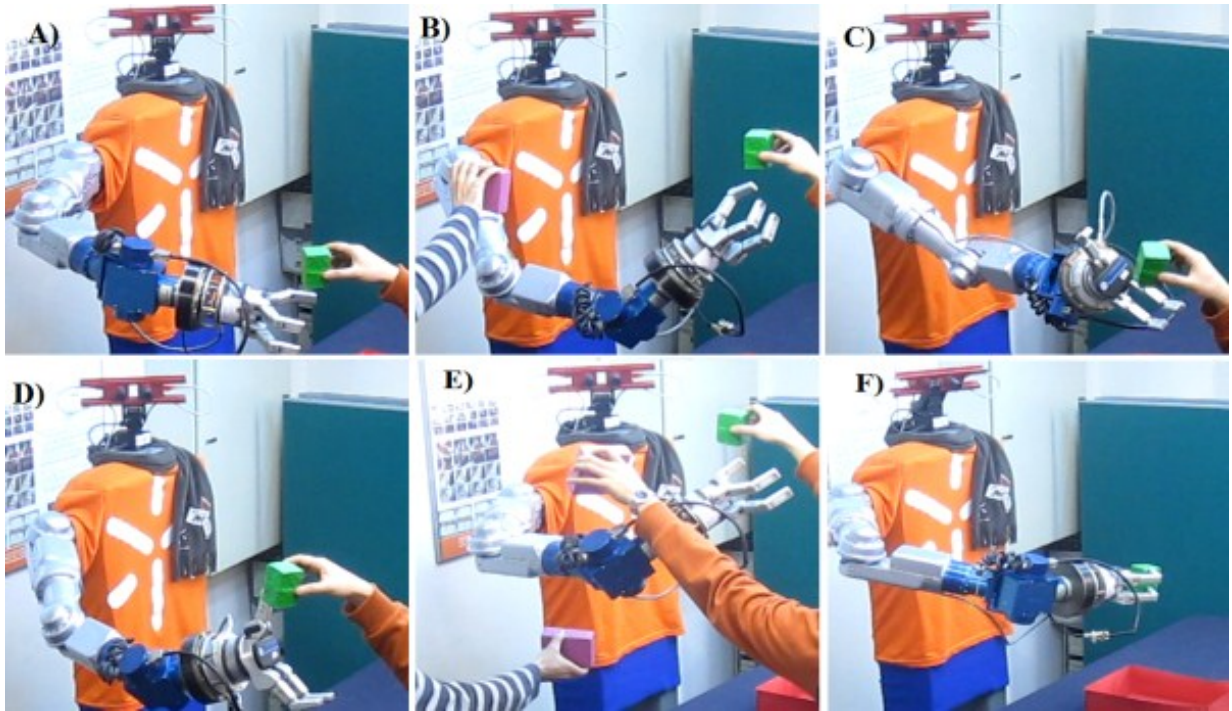
Figure 4.9: Tracking and grasping a mobile object in a dynamic obstacle environment. A)Tracking a mobile target. B)Avoid an obstacle that appears suddenly. C,D)Flexible movement with joints physical limits avoidance. E)Multiple mobile obstacles avoidance. F)Grasping and dropping the object in the target location (Video 1).

by the vision system. After avoiding an obstacle that appears suddenly in the workspace (Fig.4.9B), the robotic arm recovers (Fig.4.9C,D) as a contribution of the joints physical limit avoidance behavior. The arm is capable of keeping its links free from collision with multiple mobile obstacles appearing in the workspace (Fig.4.9E). Then the robot grasps the green object. Because its fingers are equipped with torque sensors, this provides feedback whether the object has been grasped or not. Finally, the robot rotates its head towards the target area and drops the object in the red box.

Figure 4.10 depicts the second task, which consists of drawing an ellipse on a paper sheet in a dynamic obstacle environment, by tracking an imaginary object, moving with a velocity profile which is defined by differentiating the equation of the ellipse. In Fig.4.10A, the ellipse is drawn without the presence of obstacles (magenta objects). With

the same paper, the robotic arm draws almost the same ellipse under sudden appearances and disappearances of obstacles in the workspace (Fig.4.10B,C).
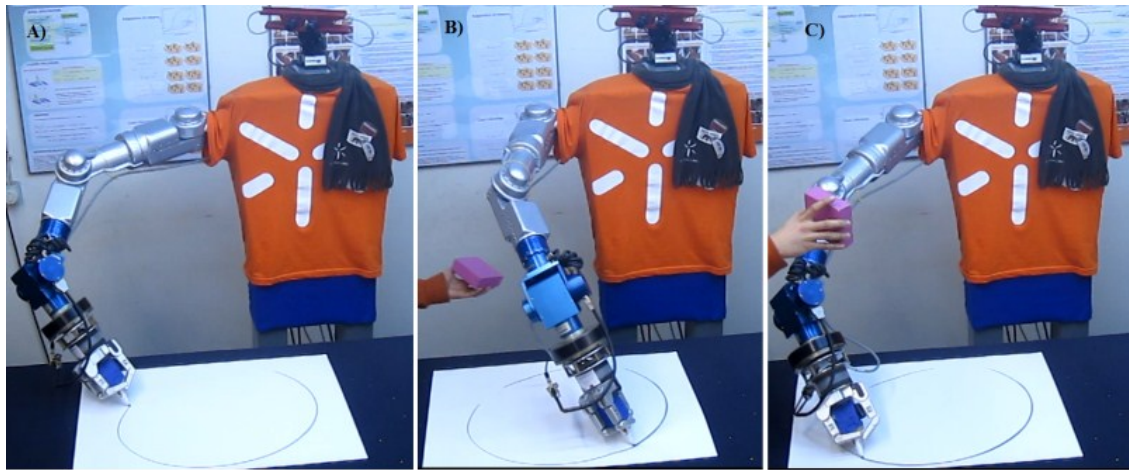
Figure 4.10: Drawing an ellipse on a paper sheet by controlling the velocity of the end effector with real-time obstacle avoidance. A)When no obstacle present in the workspace. B,C)The robotic arm keeps drawing the same ellipse while avoiding the obstacle that appears in the workspace (Video 2).

4.6 Conclusion

This chapter has contributed a method of controlling a 7-DOF anthropomorphic robotic arm for velocity-constrained tasks in dynamic target and obstacle environments, using a differential kinematics approach. The developed method deals not only with the sudden appearance and disappearance of mobile obstacles but also the noise that results from the vision system's imperfection, while keeping the robotic arm safe from the joints physical limits, in terms of position, velocity and acceleration. Two experiments were performed which consisted of: *i)* drawing an ellipse on a sheet of paper and *ii)* tracking and grasping a mobile object in dynamic obstacle environments. These experiments show the efficiency of the developed control method in such challenging applications.

Chapter 5

Forces and torques compensations for the end effector orientation

5.1 Introduction

In physical Human Robot Interaction scenarios, a reliable force, torque feedback, which increases significantly the task performance, is highly desired. Differences in forces, torques that act on sensors, can be measured with high accuracy because of sensor calibrations. However, from the fact that every component in sensors has its own weight and sensors are not perfectly symmetric, most of force sensors are subjected to errors when its orientation in 3D-space changes even without any forces acting on it. When an end effector is mounted on a force sensor, the weight of the end effector and its asymmetric distribution contributes more errors when the orientation of the end effector changes during tasks. Errors from an end effector can be compensated by modelling it as a mass and determining its 3D coordinates in the force sensor reference frame, but errors from a force sensor are difficult to compensate because they depend on the internal structure of the sensor. For instance, force and torque measurements in a FCT50 sensor from Schunk^{TM} are based on the displacement of two parallel discs. Spring elements connect the plates,

and forces and moments are calculated from the displacements using a rigidity matrix. The weight of the movable disc contributes to reading errors when the orientation of the end effector changes.

Therefore, this chapter presents a method to remove the effect of force sensors' orientation on the force and torque readings, independent of the structure of force sensors. The method also allows to compensate the errors from end effectors without modelling them.

5.2 Forces and torques compensations
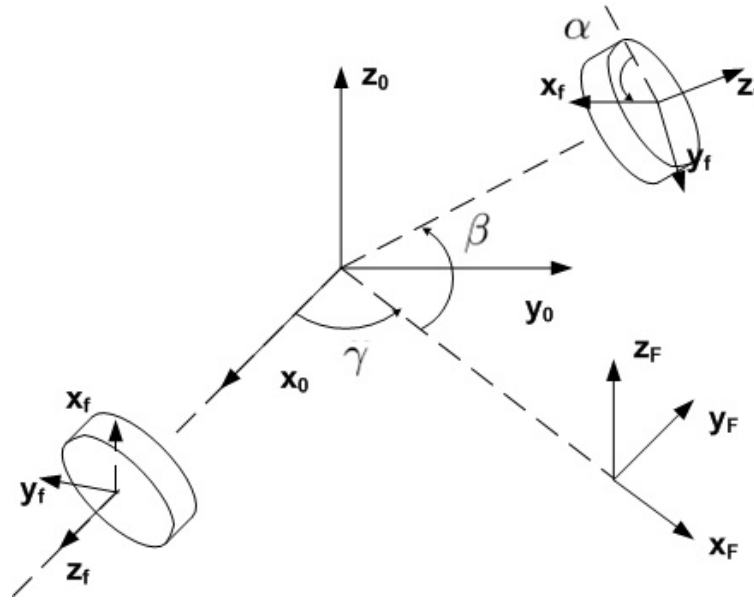
Figure 5.1: Roll, pitch angles, α and β respectively, are used as parameters for compensating the end effector orientation effect on force and torque readings

Let us consider an arbitrary force sensor with an end effector that has already been mounted on it. From the mechanical point of view, forces and torques, acting on force sensors, are functions of the roll angle α and pitch angle β as illustrated in Figure 5.1. The change in yaw angles γ only affects the force, torque distribution on the reference frame,

it does not contribute to the sensing errors when the end effector moves in 3D space.

In this thesis, the biquadratic spline interpolation is proposed to approximate force, torque errors as functions of the roll angle α and the pitch angle β. The force vector in 3D space has 6 components, including F_x, F_y, F_z, T_x, T_y and T_z. The jth force error component, which is represented in the reference frame $\{x_F, y_F, z_F\}$, is approximated by:

$$^{F}F_{c,j}(\alpha, \beta) = \sum_{i=0}^{4} \sum_{k=0}^{4} a_{ik} \cdot \alpha^i \cdot \beta^k \tag{5.1}$$

or in matrix form:

$$^{F}F_{c,j}(\alpha, \beta) = [\,\alpha^0\beta^0 \ ... \ \alpha^i\beta^k \ ... \ \alpha^4\beta^4\,] \cdot A \tag{5.2}$$

where $\alpha = [-\pi; \pi]$; $\beta = [-\frac{\pi}{2}; \frac{\pi}{2}]$ and A is the vector of coefficients

$$A = [\,a_{00} \ \cdots \ a_{ik} \ \cdots \ a_{44}\,]^T \tag{5.3}$$

which is calculated by matching values of the interpolation function $^{F}F_{c,j}$ at some specific values of α and β:

$$A = \begin{bmatrix} \alpha_1^0\beta_1^0 & \cdots & \alpha_1^4\beta_1^4 \\ \vdots & \ddots & \vdots \\ \alpha_5^0\beta_5^0 & \cdots & \alpha_5^4\beta_5^4 \end{bmatrix}^{-1} \begin{bmatrix} ^{F}F_{c,j}(\alpha_1, \beta_1) \\ \vdots \\ ^{F}F_{c,j}(\alpha_5, \beta_5) \end{bmatrix} \tag{5.4}$$

The value of the roll and pitch angles, used in force, torque sampling must not be symmetric so that the square matrix in Eq 5.4 is invertible.

Forces and torques errors are represented in the base reference frame by:

$$\begin{bmatrix} ^{0}F_{c,x} \\ ^{0}F_{c,y} \\ ^{0}F_{c,z} \\ ^{0}T_{c,x} \\ ^{0}T_{c,y} \\ ^{0}T_{c,z} \end{bmatrix} = \begin{bmatrix} cos(\gamma) & -sin(\gamma) & 0 & 0 & 0 & 0 \\ sin(\gamma) & cos(\gamma) & 0 & 0 & 0 & 0 \\ 0 & 0 & 1 & 0 & 0 & 0 \\ 0 & 0 & 0 & cos(\gamma) & -sin(\gamma) & 0 \\ 0 & 0 & 0 & sin(\gamma) & cos(\gamma) & 0 \\ 0 & 0 & 0 & 0 & 0 & 1 \end{bmatrix} \cdot \begin{bmatrix} ^{F}F_{c,x} \\ ^{F}F_{c,y} \\ ^{F}F_{c,z} \\ ^{F}T_{c,x} \\ ^{F}T_{c,y} \\ ^{F}T_{c,z} \end{bmatrix} \tag{5.5}$$

Given a specific value for the set of angles $\{\alpha, \beta, \gamma\}$, force and torque readings from a sensor will be converted to the base reference frame $\{0\}$ and then be subtracted with the force/moment errors $^{0}F_{c}$ (Eq 5.5) to remove the effect of the end effector orientation.
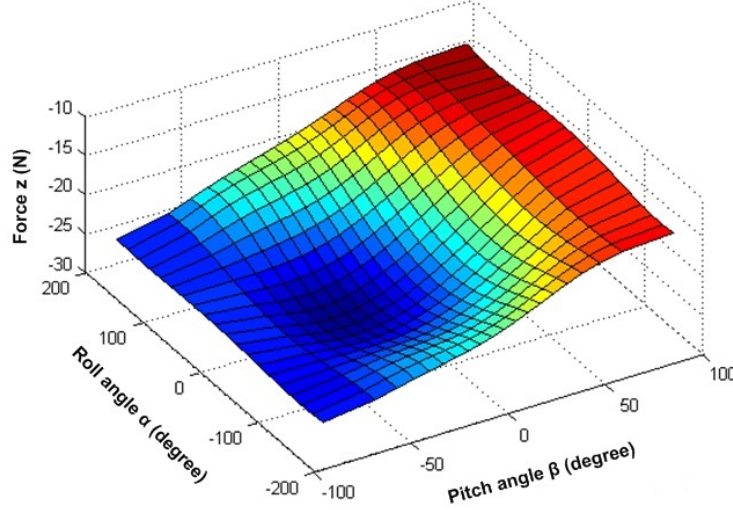
Figure 5.2: The value of the interpolation function compensating the z axis force component by sampling force, torque readings of a FCT50 sensor at $\alpha = -\pi; -1.2; 0; 1; \pi$ and $\beta = -\pi/2; -\pi/6; 0; \pi/4; \pi/2$

Figure 5.2 presents the value of a z-axis force compensation function $^{F}F_{c,z}$ for a FCT50 sensor as an example to give an insight about how much the orientation of the end effector affects reading errors. By Eq 5.5, this force component is also the same as in the base reference frame $\{0\}$. Therefore, with a perfect sensor, the value of this component is a constant, representing the weight of the end effector. However, when the pitch angle is constant and the roll angle α changes, the force varies about 1-2 N because of the asymmetry of the sensor and the end effector. When the pitch angle β changes from $\frac{-\pi}{2}$ to $\frac{\pi}{2}$, i.e. the end effector orientation changes from a point-down to a point-up position, the force changes about 10 N, which is quite large to be ignored. This error, as previously explained, comes from the sensor itself because of the weight of the moving plate inside the sensor which can be approximated by 0.5 kg.

The compensation method provides a more reliable force/torque feedback which is

very useful in force control applications. For instance, in tasks requiring the end effector to keep in contact with a very fragile surface, changes in force reading due to variations in the end effector orientation occurring during tasks may be enough to destroy the object or lose physical contact.

Figure 5.3: Drawing an ellipse upon the fragile surface of a stretched and floating paper sheet with the compensation of the end effector orientation in the force and torque readings (Video 3).

Figure 5.3-A depicts a task that an ellipse needs to be drawn upon the delicate surface of a stretched and floating paper sheet. Two ends of the A1 paper sheet are taped to two supports so that the paper can float in space. In this task, the velocities in the x and y axis and the force in the z axis of the base reference frame {0} need to be controlled so that the paper sheet is not penetrated during the drawing. Because of the fragility of the stretched paper, before starting the task, the end effector is lowered so that the brush only touches slightly the paper surface with a contact force in z axis with the intensity of 2 N. During the drawing task, the force z will be controlled to be equal to this value. The

magenta obstacle is used to interfere with the robotic arm so that large changes in the orientation of the end effector happen during the task and the performance of the developed method can be evaluated.

When there is no obstacle appearing in the workspace, the task finishes successfully either in the case of using the end effector orientation compensating method (Figure 5.3-A,B) or without the compensation (Figure 5.4-A,B). Large changes in the end effector orientation occurs when the robotic arm tries to avoid the magenta obstacle which appears in the workspace. In case of using the compensation method, the task is still accomplished successfully without destroying or losing contact with the paper (Figure 5.4-C,D,E,F). Repeat the experiment but without using the compensation of the end effec-
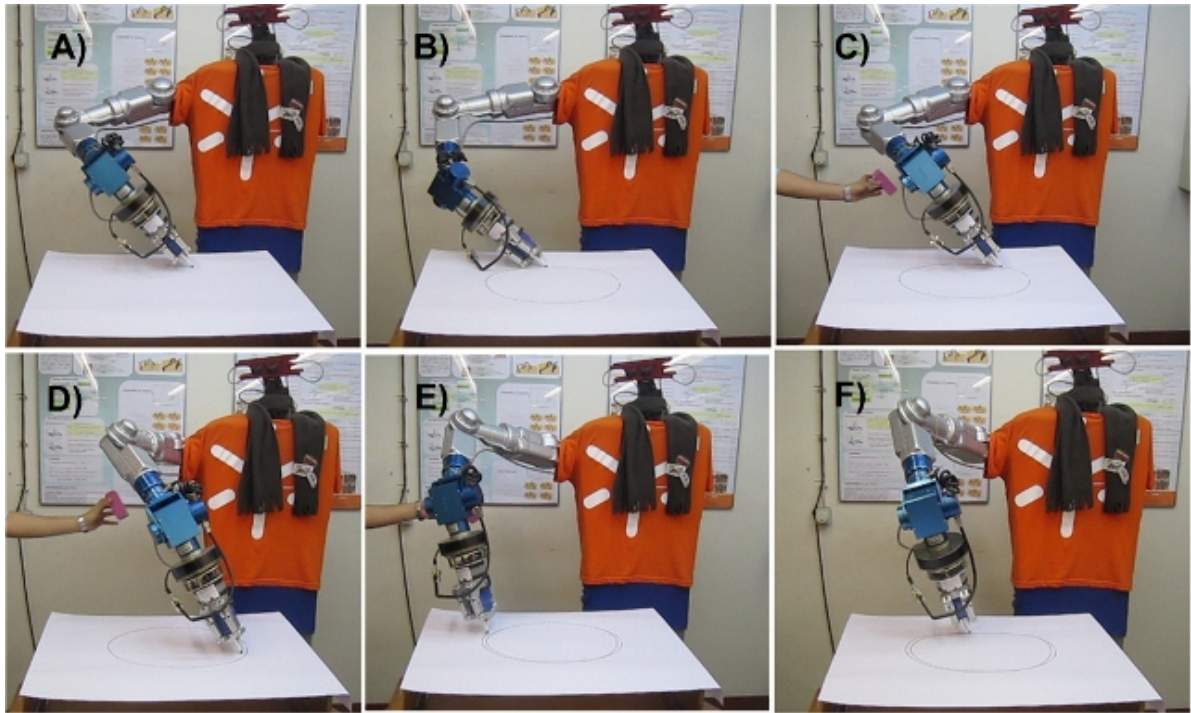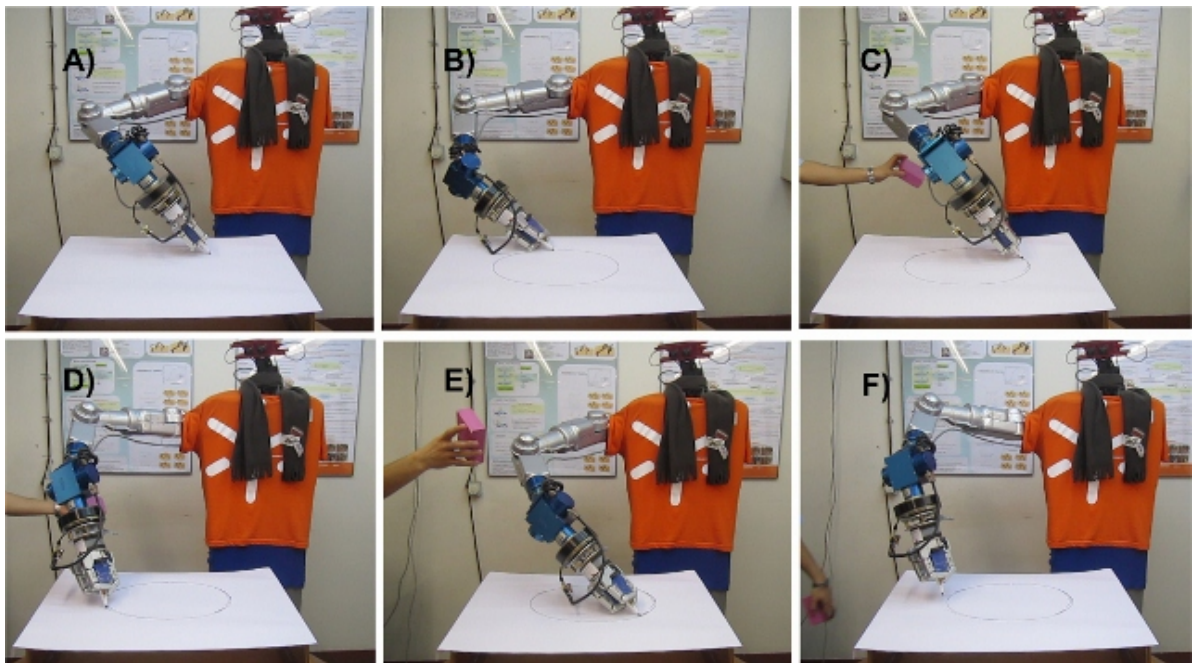

Figure 5.4: Drawing a ellipse upon the fragile surface of a stretched and floating paper sheet without the compensation for variations in the end effector orientation (Video 3).

tor orientation (Figure 5.4). The brush loses its contact with the paper surface when the end effector orientation varies too much due to the obstacle avoidance (Figure 5.4-F).

Let us consider the z-axis contact force, shown in Figure 5.5, during the drawing

task with the compensation method. Figure 5.5-A depicts the contact force, which is controlled during the task, after using the compensation method for eliminating the effect from the variation of the end effector orientation. Figure 5.5-B shows the contact force reading, before applying the compensation method, which does not represent correctly the contact force and its changes. The graph shows that with such variation of the end effector orientation, the z axis force increases more than 2 N. Because the error due to the variation of the end effector orientation is greater than the contact force that needs to be controlled, the end effector is lifted up when the compensation method is not being used. Without the compensating method, controlling small forces and torques becomes impossible in applications where the error, due to changes of the end effector orientation, is greater than the forces and torques requiring to be controlled.
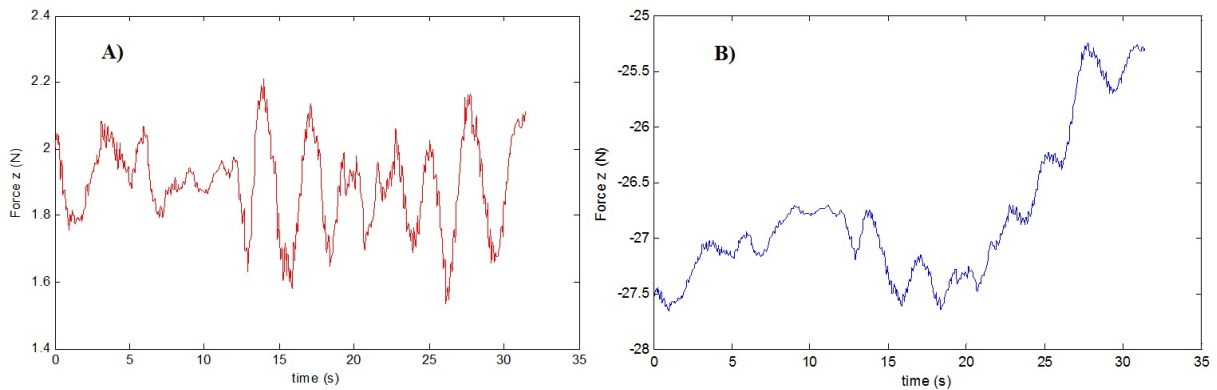
Figure 5.5: The force in z axis during the drawing task with the compensation method. A) The force after applying the compensation method. B) The force before compensating the effect of the end effector orientation, does not represent correctly the contact force and its changes.

Figure 5.6 illustrates the use of the developed method in applications that require high sensitivity in force sensing. By using the forces and torques compensating method, the anthropomorphic robot ARoS uses its three fingers hand to grasps a plate, and responds sensitively to physical interactions from a human (Figure 5.6), proving that the method allows to achieve high efficiency in force control applications.

Figure 5.6: The robot ARoS reacts sensitively to forces, torques interations from a human (Video 4).

Chapter 6

Virtual Elastic System: A solution to control anthropomorphic mobile manipulators for physical Human-Robot Interactions in dynamic environments

6.1   Introduction

Recent research has been focused on Human-Robot Interaction, especially physical Human-Robot Interaction (pHRI) ([Santis et al., 2007]). For life quality improvements, robots are supposed to expand human capabilities, e.g. force, speed and precision while humans bring experience, knowledge and understanding to accomplish tasks. Not only new robot designs have been developed to provide more safety, dependability and compliance (see, e.g. [Zinn et al., 2004], [Wyrobek et al., 2008] and [Quigley et al., 2011]) but control methods, which enable robots to perform pHRI tasks, have been also studied actively (see, e.g. [Buerger & Hogan, 2007], [Calinon et al., 2010] and [Flacco & Luca, 2011]).

Redundant 7-DOF anthropomorphic robotic arms, whose structure imitates human

arms with three DOF on the shoulder, one DOF on the elbow and three DOF on the wrist, possess more dexterity to perform complex movements and are more promising in tasks involving physical contacts with humans. By mounting these robotic arms on mobile platforms, the capability of robotic systems is increased further with the extention of workspaces. When performing pHRI tasks in dynamic environments, the robotic arm must react according to forces and torques applied by the human while the mobile platform keeps it away from the workspace boundary, and the whole system must be free from collision with static and dynamic obstacles. In many conventional mobile ma-

Figure 6.1: Dumbo, an anthropomorphic mobile manipulator, is performing a cooperative object transportation task

nipulators, a robotic arm is mounted on the top of a mobile platform and it has a joint whose rotary axis is aligned with the pure rotary axis of the mobile platform. Thus, the mobile platform can rotate without changing the pose of the manipulator even when the

end effector is being kept still. In anthropomorphic mobile manipulators, 7-DOF robotic arms can be side-mounted on mobile platforms to provide friendly human interactions. However, these types of mobile manipulators possess more geometric and kinematric constraints because rotational movements of the mobile platform change strongly the manipulator configuration and may lead to a collision between the arm and the body. In the case of using a nonholonomic mobile platform, its limited movements make control strategies face even more challenges in ensuring that the mobile platform supports the robotic arm properly, while still having enough flexibility to navigate through unstructured and dynamic environments. The control methods, e.g. [Janiak & Tchon, 2010] and [Luca et al., 2010], which involve the calculation of an extended Jacobian matrix for unifying the control of mobile platforms and manipulators, become inadequate because local optimisations, based on the nullspace of the associated Jacobian, can not garantee that all constraints between manipulators and mobile platform are satisfied. Free obstacles navigation for both the manipulator and the mobile platform simultaneously is also a challenging issue.

Moreover, in pHRI scenarios, robotic systems must respect some safety requirements because they and human partners share the same workspaces to perform cooperative tasks. As a specific task, we consider here Human-Robot Joint Transportation tasks, and we impose the following contraints:

1. The robot must carry a bulky load with a human partner while avoiding collisions with obstacles either static or dynamic (e.g. people) that may appear in its vicinity.

2. For safety, the robot must strictly respect physical interactions from the human, i.e. the robot is not supposed to move or rotate the object without forces/torques exerted by the human.

3. The whole robot, i.e the manipulator and mobile platform must protect itseft from collision with obstacles. In the case that human movements lead the robot to a dangerous situation, which it can not overcome itself, the robot must be capable to instruct the human partner to move in a more favorable direction so that the object

transportation task can proceed successfully.

The objective of this chapter is to develop a novel method which enables controlling of anthropomorphic mobile manipulators for pHRI tasks in dynamic environments. By proposing a Virtual Elastic System for linking a 7-DOF anthropomorphic robotic arm with a nonholomic mobile platform, a powerful control strategy is achieved through an integration of different control methods for each system. More specifically, movements of the end effector, which are coordinated through contact forces and torques exerted by the human, are controlled by using Inverse Differential Kinematics (see, e.g. [Wang et al., 2010], [Papadopoulos & Poulakakis, 2000]) while the mobile platform is kept away from obstacles with Dynamical Systems (see, e.g. [Bicho et al., 2000], [Soares et al., 2007]). Experiments in Human-Robot Interaction scenarios have proved the developed method to be a powerful control approach for mobile manipulators in tasks which involve physical contacts with human and also requiring free obstacle motions for the whole system. Extensions of the Virtual Elastic System for holonomic mobile platforms or higher degrees of freedom manipulators are presented through simulations to give insights about how to apply the Virtual Elastic System for other types of mobile manipulators.

6.2   Related Work

In ([Ellekilde & Christensen, 2009]), a mobile manipulator is controlled by using a Dynamical System approach to achieve obstacle avoidance for both the mobile platform and the robotic arm. A competitive dynamics is used to fuse behaviors of the two systems, where the manipulator is retracted and the mobile heads to the target when it is not within the reaching range of the manipulator. When the target is in the workspace, the mobile platform stops and the manipulator moves to the target. Thus, the method is suitable to move the end effector from place-to-place without taking account of its trajectory constraints, for instances, to maintain physical contacts in interaction with human. The nonlinear Dynamical Systems approach is also used in ([Bicho et al., 2003]) for controlling a mobile

robot to transport a large size object in cooperation with a human partner. The mobile platform maintains a predefined formation with human by using feedback from a free rotational joint coupled to a free prismatic joint which support the object. However, without a proper manipulator, interactions involving contacts with human are limited.

In ([Bayle et al., 2003]), a planar 2-DOF manipulator, mounted on top of a non-holonomic car-liked platform is controlled by using an Inverse Differentpial Kinematics approach. The method calculates Jacobian matrices and the manipulability of mobile manipulators and controls the end effector velocity. However, the problem of obstacle avoidance has not been addressed. In ([Tchon & Jakubiak, 2002]), an Inverse Differential Kinematics approach is also used to control car-liked mobile platform with a top mounted manipulator. The Extended Jacobian Inverse Kinematics algorithms allows to unify the control of manipulators with mobile platforms. The method has been extended for constrained movements, more specifically, the turn angle of the front wheels is restricted ([Janiak & Tchon, 2010])but the obstacle avoidance problem has not been considered. The method in ([Luca et al., 2006]) of controlling a plannar mobile platform with a 2R manipulator is also based on Inverse Differential Kinematics with the Projected Gradient and the Reduced Gradient optimization-based methods for redundacy resolution. The nullspace optimisation has been added to the method in ([Luca et al., 2010]), taking account of velocity inputs of steering wheels which contributes to task execution. Although Inverse Differential Kinematics approaches can be used to control directly velocity of the end effector and implement additional behaviours such as joint limits and obstacle avoidance for manipulators by optimizing respective criterion functions, these local optimisation can not ensure the success of behaviors for the whole system, especially in the presence of strong affections from movements of nonholonomic mobile platforms on the configuration of side-mounted manipulators. Therefore, in our approach, an Inverse Differential Kinematics for controlling the redundant manipulator is combined with a Dynamical System approach for the mobile platform in order to achieve free obstacles movements for the whole system.

In (Brock & Khatib [2002]), the Elastic Strip Framework, which allows the integration of motion planning and task-oriented control, is used to control mobile manipulators with real-time obstacle avoidance. The method assumes that mobile manipulators move in an elastic tunnel which will be deformed by repulsive forces computed as a function of distances from obstacles. However, the problems of nonholonomic mobile platforms and strong affections from their movements to the configuration of side-mounted robotic arms, have not been addressed because the method uses a holonomic mobile platform with 3 actuated wheels and the 6-DOF manipulator is mounted on the top, center of the mobile platform. In (Vannoy & Xiao [2008]), the Real-Time Adaptive Motion Planning allows to control mobile manipulators in dynamic environments. A planner is used to choose the fitest path of knot configurations of mobile platforms and manipulators. The method has been validated with simulations for dynamic obstacle avoidance including other mobile manipulators. Nevertheless, the method have focused on the place-to-place end effectors moving task and 6-DOF manipulators are mounted on the top, center of holonomic mobile platforms.

In (Takubo et al. [2002]), a 7-DOF manipulator cooperates with a human to transport a long object for a short distance. The impedance control of the method allows to control contact forces during tranportation but a mobile platform has not been used. In (Portillo-Velez et al. [2011]), an optimal admittance force controller has been proposed to allow the modification of the end effector trajectory to control forces during human interaction. A 3-DOF manipulator is used in experiments to respond to forces from a human palm. In (Nozaki & Murakami [2009]), a 6-DOF manipulator, mounted on top, center of the mobile platform through a passive rotary joint, is used for cooperative object transportation tasks. The manipulator is controlled by Inverse Differential Kinematics and the control of the mobile platform is based on the performance index. The movement control of the system and the stability of the mobile platform have been validated through simulations with force inputs from the impedance model. In (Lawitzky et al. [2010]), the problem of manipulating bulky objects has been addressed and validated in a virtual environment

with inputs from a force/torque sensor. The method has focused on the effort distribution between human and robot, which is achieved by Effort sharing policies, derived from the geometric and dynamic task properties. However, the mobile robot has been assumed to be a holonomic one and the problem of dynamic environments has not been taken into account.

6.3 The proposed Virtual Elastic System

Anthropomorphic mobile manipulators, for instance, a 2-wheels mobile platform with a side-mounted redundant 7-DOF anthropomorphic robotic arm, provide more friendly human interactions. However, the robotic system possesses more geometric and kinematic constraints because of limited movements of the nonholonomic mobile platform and the strong affection of its movements on the robotic arm configuration. The control problem becomes more challenging in pHRI scenarios where the end effector needs to maintain physical contact with a human partner and the whole system needs to avoid dynamic obstacles.

This section presents a control approach which combines different control strategies of each system, i.e. the mobile platform and the manipulator, to achieve a powerful control method for anthropomorphic mobile manipulators (Figure 6.2). The Virtual Elastic System is proposed to link the two controllers. A Nonlinear Dynamical System approach is used in the Mobile Platform Controller to generate imaginary forces and torques from obstacles information, i.e. sensed distances and orientations. These forces are supplied to the Virtual Elastic System to generate a new state of its virtual tension and torsion springs, taking account of mass and damping effects. The state transition is commited in the real world by converting the changes in lengths of the springs into linear and angular velocities of the mobile platform. In the case that the velocity of the end effector is constrainted by tasks, for instance, by physical contacts with human, the movement of the end effector needs to be decoupled from the movement of the mobile platform. Thus, an end effec-
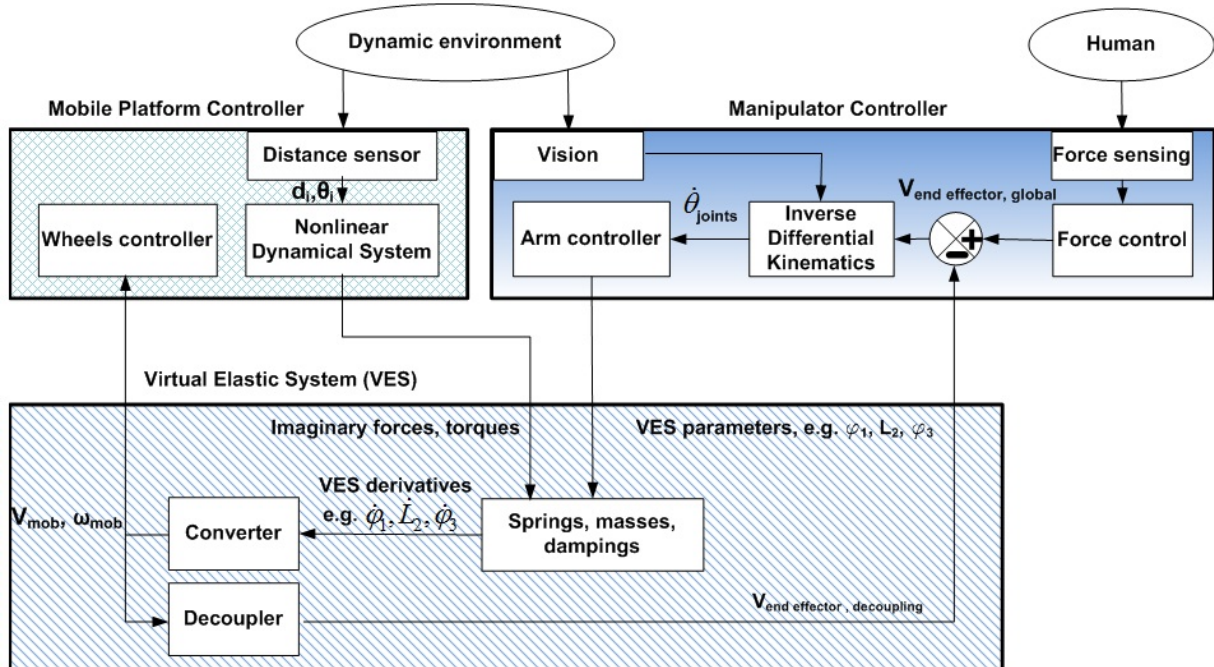
Figure 6.2: The proposed control approach for anthropomorphic mobile manipulators uses a Virtual Elastic System which enables the combination of a Dynamical System approach for the mobile platform and an Inverse Differential Kinematics for the manipulator

tor velocity vector which results from the mobile platform movement, is subtracted from the desired end effector velocity. The manipulator controller is composed of a force sensing method which allows to capture contact forces and torques and represents them in the same reference frame of the end effector velocity. These forces are converted into the desired linear and angular velocity for the end effector and an Inverse Differential Kinematics approach is adopted to calculate velocities of joints from the task-space velocity. The obstacle avoidance behavior for the manipulator is achieved by acquiring obstacles coordinates through a vision system and applying a nullspace optimisation technique.

The fundamental idea of the Virtual Elastic System (VES) is to consider that the relative configuration between the manipulator and the mobile platform is maintained by a set of tension, torsion springs with mass and damping effects. In 7-DOF anthropomorphic mobile manipulators, the robotic arm can be kept away from its workspace boundary by
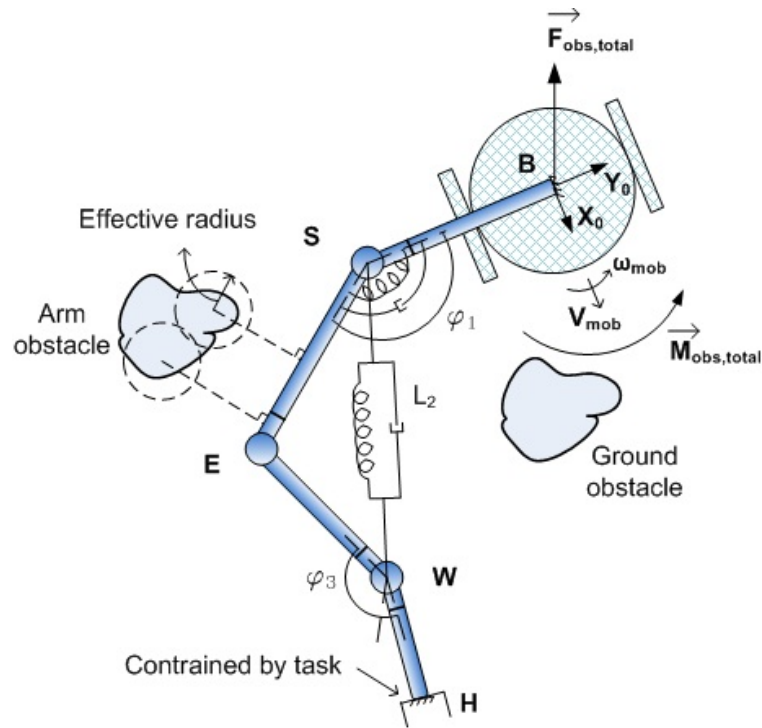
Figure 6.3: Virtual Elastic System is a set of tension and torsion springs with masses and dampings which connects the mobile platform with the manipulator

maintaining three parameters $\{\varphi_1, L_2, \varphi_3\}$ (Figure 6.3) which characterize the opening angle of the arm from the body, the arm stretching length and the wrist angle respectively, in their limit ranges. In case of a nonholonomic 2-wheels mobile platform, two parameters $\{\varphi_1, L_2\}$ can be controlled independently and featured in the the Virtual Elastic System as a torsion spring and a tension one. The third parameter φ_3 can not be controlled directly because the mobile platform only has two degrees of freedom. However, controlling two parameters $\{\varphi_1, L_2\}$ gives a satisfactory performance and in most cases, can make the parameter φ_3 to converge to a value in the middle of its range. Moreover, control of the angle φ_3 is proved to give a poor performance for nonholonomic mobile manipulators. Instead of controling this parameter, another solution should be used when φ_3 approaches its limits, for instance, the robot uses a speech synthesis to tell the human to support him by moving toward a more favorable direction. These problems are presented in the Section 6.6 with discussions about extensions of the Virtual Elastic System for holonomic mobile

platforms or manipulators with higher degrees of freedom.

In the case of anthropomorphic mobile manipulators with a nonholonomic mobile platform, two parameters $\{\varphi_1, L_2\}$ can be controlled independently and governed by the following equations:

$$K_{m1}\ddot{\varphi}_1 + K_{v1}\dot{\varphi}_1 + K_{e1}(\varphi_1 - \varphi_{1,0}) = K_{f1}M_1, \tag{6.1}$$

$$K_{m2}\ddot{L}_2 + K_{v2}\dot{L}_2 + K_{e2}(L_2 - L_{2,0}) = K_{f2}F_2. \tag{6.2}$$

The coefficients K_{m1} and K_{m2} represent the inertial property of the elastic system. More specifically, K_{m1} has the dimension of an inertia moment while K_{m2} has the dimension of a mass. The damping property is provided by the coefficients K_{v1} and K_{v2}. The elastic coefficients K_{e1} and K_{e2} feature the stiffness of the virtual system while $\varphi_{1,0}$ and $L_{2,0}$ are equilibrium values when there is no external force F_2 or moment M_1, derived from sensed obstacles in the ground, acting on the system. The coefficients K_{f1} and K_{f2} are used to control the effect of external repulsive forces and torques from obstacles. All coefficients of the Virtual Elastic System can change dynamically, which makes the system robust in unstructured, dynamic environments.

Let us consider the dynamic equation which governs the angular length φ_1 of the torsion spring 1:

$$\ddot{\varphi}_1 = \frac{K_{f1}M_1}{K_{m1}} - \frac{K_{v1}}{K_{m1}}\dot{\varphi}_1 - \frac{K_{e1}}{K_{m1}}(\varphi_1 - \varphi_{1,0}). \tag{6.3}$$

The block diagram is available in Figure 6.4. This is a second order system with the damping ratio:

$$\varsigma_1 = \frac{K_{v1}}{2\sqrt{K_{m1}K_{e1}}}. \tag{6.4}$$

An underdamping system is undesirable because the robot may be damaged by oscillations. Thus, the elastic system should be a critically damped system for fast responses without oscillations, which is achieved by setting the damping ratio ς_1 equal to 1. The
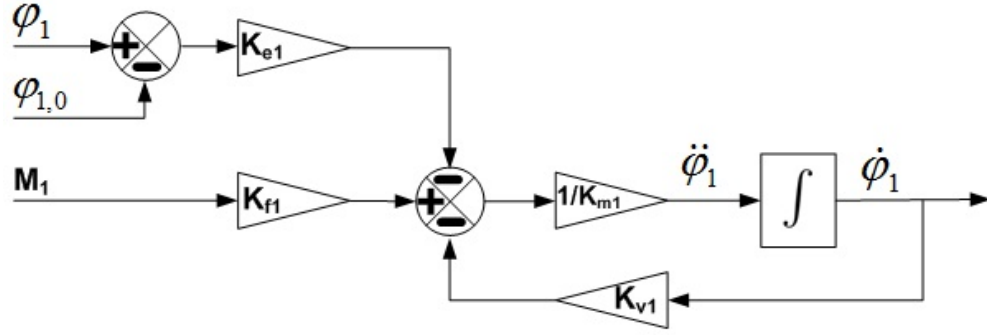
Figure 6.4: Block diagram for generating the derivatives of the VES parameter φ_1

current value of φ_1 is computed from the configuration of the robotic arm:

$$\varphi_1 = \arccos \left(\frac{\vec{SB} \cdot \vec{SE}}{L_{SB} \, L_{SE}} \right) \tag{6.5}$$

$$= \begin{cases} \arccos \left(\dfrac{y_E + L_{SB}}{L_{SE}} \right) & \text{if } x_E > 0 \\[2ex] 2\pi - \arccos \left(\dfrac{y_E + L_{SB}}{L_{SE}} \right) & \text{if } x_E < 0 \end{cases} \tag{6.6}$$

where x_E, y_E are coordinates of the Elbow in the base reference frame {0} which is attached to the mobile platform and L_{SB}, L_{SE} are the length of links Shoulder-Base and Shoulder-Elbow respectively.

Under effects of the external moment M_1, the parameter φ_1 tends to reach to a steady equilibrium value:

$$\varphi_{1,steady} = \frac{K_{f1} M_1}{K_{e1}} + \varphi_{1,0}. \tag{6.7}$$

When the external moment M_1 is high, for instance, obstacles could approach the mobile platform so close, the steady value $\varphi_{1,steady}$ may exceed the limits of the parameter φ_1, which is determined by geometric constraints or physical joint limits of the robotic arm. Therefore, the coefficient K_{f1} is used to control the effect of the repulsive moment M_1:

$$K_{f1} = \frac{1}{1 + \exp\left(-\frac{\varphi_1 - \varphi_{1,min}}{\sigma_{f1}}\right)} + \frac{1}{1 + \exp\left(\frac{\varphi_1 - \varphi_{1,max}}{\sigma_{f1}}\right)} - 1. \tag{6.8}$$

where $\varphi_{1,min}$, $\varphi_{1,max}$ are minimum and maximum allowed value of φ_1 and the coefficient σ_{f1} controls the decay rate of K_{f1} when φ_1 approaches to its limits. In normal operation,
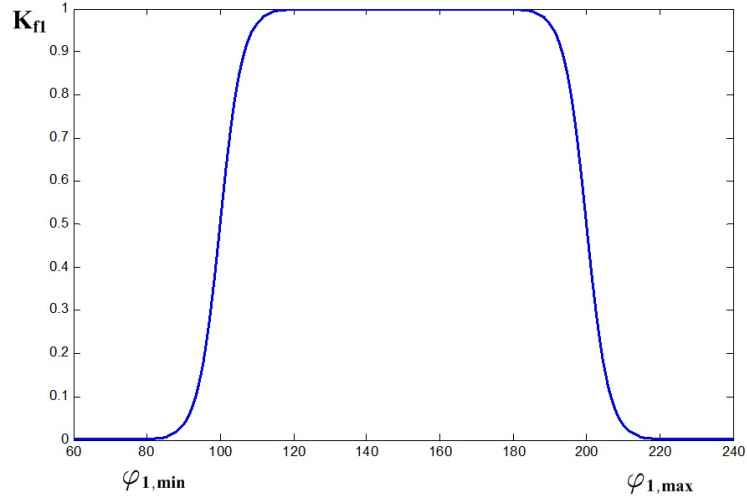
Figure 6.5: Graph of the coefficient K_{f1} which protects φ_1 from reaching to its limits when the obstacles repulsive torque becomes excessive (See Eq 6.8).

K_{f1} is equal to 1 and the repulsive moment M_1 exerts its full effects on φ_1. When φ_1 reaches to its limits, K_{f1} becomes 0 and φ_1 is protected from excessive moments due to obstacles (Figure 6.5).

The stiffness of the virtual system is defined by the elastic coefficients, i.e. K_{e1} and K_{e2}. A high stiffness makes the mobile platform to respond quickly for supporting the manipulator (Figure 6.6-A,B,C). It means that the opening angle of the arm from the body φ_1 and the arm stretching length L_2 are kept close to their equilibrium values, defined by a desired pose of the mobile manipulator. Meanwhile, if the stiffness is low, the robotic arm is loosed from the mobile platform (Figure 6.6-D,E,F). When navigating close to obstacles, a high stiffness limits the mobile manipulator's flexibility for obstacles avoidance. The higher stiffness the virtual system has, the stronger imaginary forces and torques from obstacles must be generated to move the mobile platform. To exploit the capability of the mobile manipulator for obstacle avoidance, the robotic arm is expected to stretch out as much as possible, i.e. the Virtual Elastic System works near the limits of its parameters φ_1 and L_2 when obstacles appear close to the mobile platform. With high stiffness, VES parameters will change with high speed if these obstacles disappear suddenly, which

may not be supported by the robot hardware. A soft link between the manipulator and the mobile platform will allow the robot to avoid obstacles more elegantly.
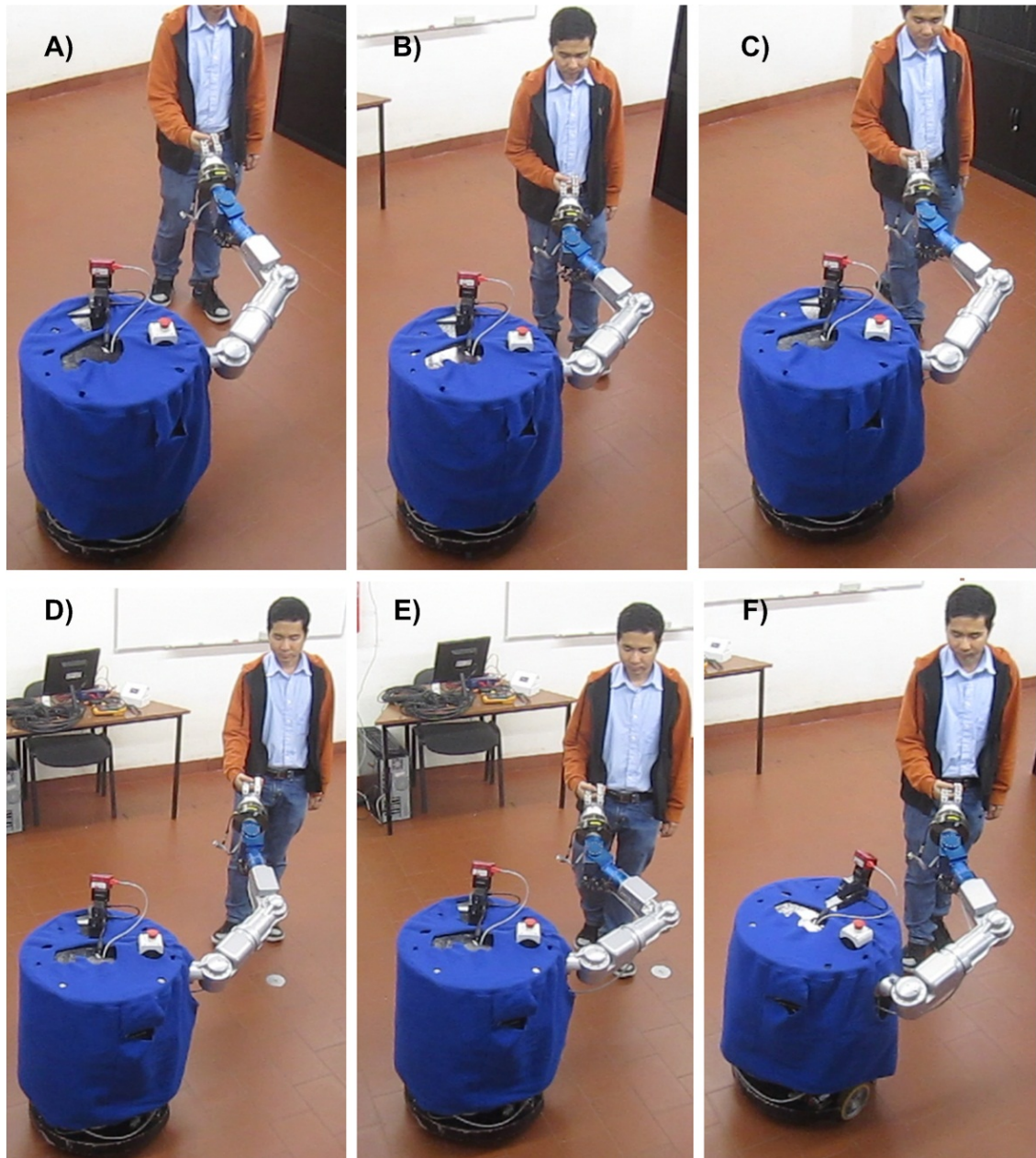

Figure 6.6: Stiffness of the virtual system and its effect on the mobile manipulator performance. A high stiffness makes the mobile platform to respond quickly for supporting the manipulator (A,B,C) while a low stiffness allows the mobile platform loosed from the mobile platform (D,E,F) (Video 5).

Thus, the elastic coefficient K_{e1} which represents the stiffness of the torsion spring 1, can be computed by:

$$K_{e1} = \lambda_{e1} + \frac{\kappa_{e1}}{1 + \exp\left(\frac{-(\varphi_1 - \varphi_{1,min})}{\sigma_{e1}}\right)} + \frac{\kappa_{e1}}{1 + \exp\left(\frac{\varphi_1 - \varphi_{1,max}}{\sigma_{e1}}\right)} - \kappa_{e1}. \quad (6.9)$$

where λ_{e1} is the basic stiffness which allows to soften the torsion spring 1 when it operates near its limits, for instance, to avoid obstacles while the coefficient κ_{e1} is an increased stiffness which allows the mobile platform to react quickly in order to keep a desired pose of the mobile manipulator. The coefficient σ_{e1} is used to control the stiffness transition rate.

When the difference between the current pose and the desired pose of the mobile manipulator is large or the strength of the external moment M_1 changes sharply, for example, obstacles appear so close to the mobile platform or nearby obstacles disappear suddenly, the high acceleration of φ_1 may not be supported by the robotic hardwares, especially the robotic arm. Therefore, the acceleration $\ddot{\varphi}_1$ needs to be adjusted by the inertia coefficient K_{m1}. A system with high inertial property has more protection from shocks but slower settling time. The inertia momentum K_{m1} can be adjusted by using the following equation:

$$K_{m1} = \lambda_{m1} + \frac{|\varphi_1 - \varphi_{1,steady}|}{\sigma_{m1}}. \quad (6.10)$$

where the first term is a basic momentum which allows the virtual system to reach to its steady state quickly. The second term is an increased inertia momentum for regularizing the system response when the difference between the current φ_1 and its steady value $\varphi_{1,steady}$ (Eq.6.7) is relatively large in comparison with the value of the coefficient σ_{m1}. This increment is useful in situations that the mobile manipulator needs to recover from an arbitrary configuration to a desired pose. For instance, Figure 6.7 depicts a scenario where the robot needs to transform from a compact resting configuration to a desired pose and be ready to interact with a human partner when he exerts forces on the end effector by holding it. The increased inertia momentum protects the system from high accelerations of VES parameters which are resulted from the large difference between the

current configuration and the desired pose of the mobile manipulator. The transformation is dynamic, i.e. the mobile manipulator will avoid obstacles which may appear during the transformation.
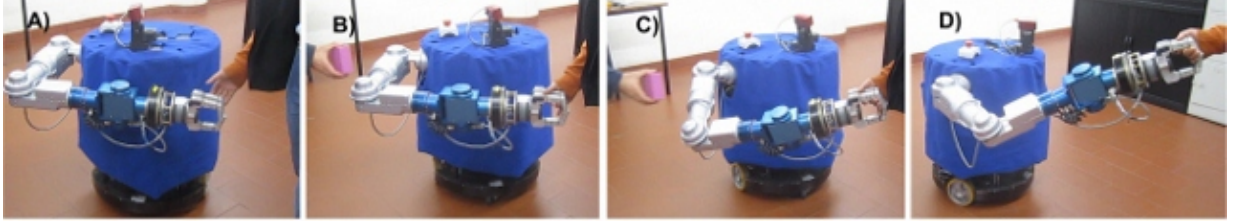

Figure 6.7: The inertial property of the Virtual Elastic System is adjusted to protect the system from high accelerations during the transformation from a compact configuration of the mobile manipulator. The mobile manipulator is resting in a compact configuration (A) and begins to tranform to a comfortable configuration when a human interacts with it by touching the hand (B). An obstacle appears close to the robotic arm during the tranformation and the robot avoids the obstacle (C). The robot finish its tranformation and the human takes the robot going around by holding its hand (D) (Video 6).

The damping coefficient K_{v1} relates to other coefficients by the critically damping condition with the damping ratio ς_1 (Eq.6.4) equal to 1:

$$K_{v1} = 2\sqrt{K_{e1}K_{m1}}. \tag{6.11}$$

Similarly, the length L_2 of the tension spring 2 is governed by the dynamic equation:

$$\ddot{L}_2 = \frac{K_{f2}F_2}{K_{m2}} - \frac{K_{v2}}{K_{m2}}\dot{L}_2 - \frac{K_{e2}}{K_{m2}}(L_2 - L_{2,0}), \tag{6.12}$$

The current value L_2 is computed from the configuration of the robotic arm:

$$L_2 = \left\|\vec{SW}\right\| = \sqrt{x_W^2 + (y_W + L_{SB})^2 + z_W^2}. \tag{6.13}$$

where x_W, y_W and z_W are coordinates of the Wrist in the base reference frame {0} and L_{SB} is the length of the Shoulder-Base link. Under the effect of the repulsive force F_2 due to obstacles on the ground, the arm stretching length L_2 tends to reach to a steady value

$L_{2,steady}$:

$$L_{2,steady} = \frac{K_{f2}F_2}{K_{e2}} + L_{2,0}. \tag{6.14}$$

The coefficients K_{f2}, K_{e2}, K_{m2} and K_{v2} in Eq.6.12 are determined from the following equations:

$$K_{f2} = \frac{1}{1 + \exp\left(-\frac{L_2 - L_{2,min}}{\sigma_{f2}}\right)} + \frac{1}{1 + \exp\left(\frac{L_2 - L_{2,max}}{\sigma_{f2}}\right)} - 1. \tag{6.15}$$

where F_2 is the total external repulsive force, exerted by obstacles on the ground and the coefficient K_{f2} will prevent the robotic arm from stretching or retracting beyond its limits when obstacles appear so close to the mobile platform. The stiffness of the spring, governed by the elastic coefficient K_{e2}, is kept high to give fast response of the mobile platform for keeping a desired pose for the mobile manipulator. However, the elastic coefficient K_{e2} should become low for enabling the manipulator to stretch as much as possible when the mobile platform navigates close to obstacles.

$$K_{e2} = \lambda_{e2} + \frac{\kappa_{e2}}{1 + \exp\left(-\frac{L_2 - L_{2,min}}{\sigma_{e2}}\right)} + \frac{\kappa_{e2}}{1 + \exp\left(\frac{L_2 - L_{2,max}}{\sigma_{e2}}\right)} - \kappa_{e2}. \tag{6.16}$$

The inertia mass property, represented by K_{m2}, protects the system from shocks when the acceleration $\ddot{L}_2$ becomes too high.

$$K_{m2} = \lambda_2 + \frac{|L_2 - L_{2,steady}|}{\sigma_{m2}}. \tag{6.17}$$

The damping coefficient K_{v2} is determined by the critically damping condition which ensures fast responses without oscillations.

$$K_{v2} = 2\sqrt{K_{e2}K_{m2}}. \tag{6.18}$$

After the new state of the Virtual Elastic System is determined with a set of parameters $\{\varphi_1, L_2\}$ and their derivatives, these changes need to be commited in the real world by converting these parameters into linear and angular velocity of the mobile platform.

$$\omega_{mob} = \dot{\varphi}_1, \tag{6.19}$$

$$V_{mob} = -\dot{L}_2 \, \cos\left(\vec{x0}, \vec{SW}\right) = -\dot{L}_2 \frac{x_W}{L_2}. \tag{6.20}$$

where x_W is the x coordinate of the Wrist in the reference frame {0}.

Whenever the VES parameters $\{\varphi_1, L_2\}$ changes, for instance, because the end effector is performing tasks or the manipulator is avoiding obstacles, the mobile platform will move to restore the robot pose to a desired one. Therefore, in order to decouple the movement of the end effector and the mobile platform, the end effector velocity, which results from the mobile platform movement, needs to be substracted from the desired velocity for the Hand (Figure 6.8). The end effector velocity for decoupling is calculated by:

$$V_{H,decoupling} = \begin{bmatrix} v_X \\ v_Y \\ v_Z \\ \omega_X \\ \omega_Y \\ \omega_Z \end{bmatrix} = \begin{bmatrix} V_{mob} - \omega_{mob} \, y_H \\ \omega_{mob} \, x_H \\ 0 \\ 0 \\ 0 \\ \omega_{mob} \end{bmatrix}. \tag{6.21}$$

where x_H and y_H are coordinates of the center of the Hand in reference frame {0}.

6.4   Control of an anthropomorphic mobile manipulator

6.4.1   Control of a nonholonomic mobile platform

The obstacle avoidance behavior for the mobile platform is implemented, using a Nonlinear Dynamical Systems approach (Bicho et al. [2000]). Static or dynamic obstacles exert their repulsive forcelets on the mobile platform as functions of sensed distances and orientations. The effects of these forcelets on the Virtual Elastic System are represented as a total moment M_1 and a total force F_2. The total repulsive moment M_1, which makes the mobile platform to rotate away from obstacles, is computed by the following equation:

$$M_1 = \sum_i M_{1,i} = \sum_i \lambda_i (\phi - \psi_i) \exp\left(\frac{-(\phi - \psi_i)^2}{2\sigma_i^2}\right), \tag{6.22}$$
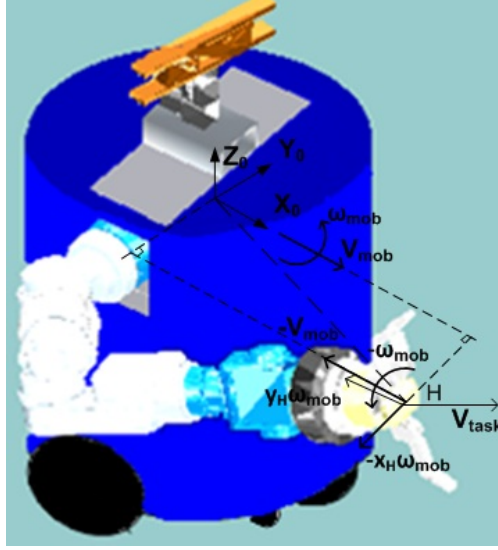
Figure 6.8: The end effector velocity vector, which results from the movement of the mobile platform, needs to be substracted from the desired end effector velocity in order to decouple the movement of the mobile platform and the end effector

where ϕ is the heading direction of the mobile platform, ψ_i is the orientation of the ith obtacle to the mobile platform in the world as illustrated in Figure 6.9. The term $(\phi - \psi_i)$ is the relative direction from the robot to the ith obstacle:

$$\phi - \psi_i = -\theta_i, \tag{6.23}$$

where θ_i is the relative pointing angle of the ith distance sensor which is constant due to the sensor position. The method allows to aquire orientations from obstacles to the mobile platform without the information about the position and orientation of the mobile platform and obstacles in the world. Thus, a set of low level sensors such as infra-red sensors can be used for distance sensing. In the robot Dumbo, a laser range finder allows to define the number of distance sensors and their respective pointing angles.

The term λ_i in Eq.6.22 represents the strength of repulsion, decreasing by the sensed distance d_i:

$$\lambda_i = \beta_1 \exp\left(\frac{-d_i}{\beta_2}\right), \tag{6.24}$$

The coefficient β_1 determines the maximum strength while the coefficient β_2 affects the
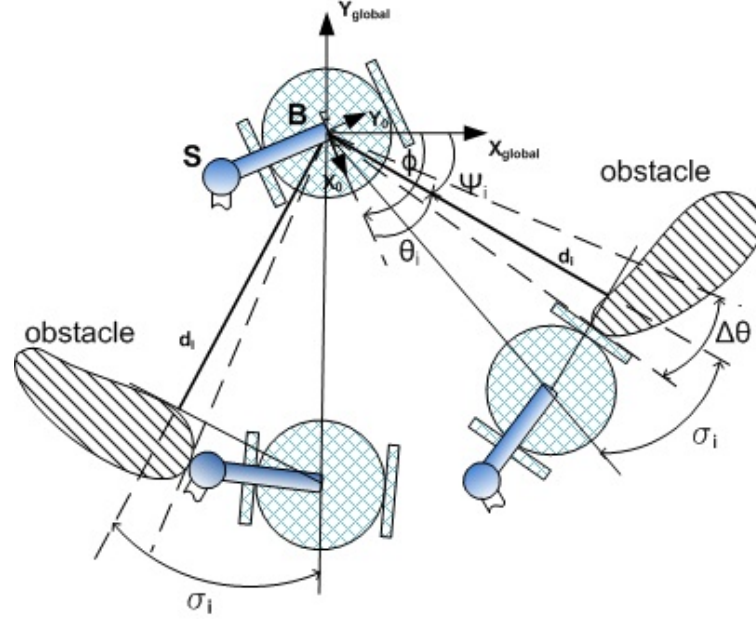
Figure 6.9: A dynamical system approach which achieves the obstacles avoidance behavior for the mobile platform, takes account of the Shoulder of the side-mounted robotic arm

decay rate of the repulsive forcelet as the distance to the obstacle d_i increases.

The term σ_i in Eq 6.22 determines the angular range over which the obstacle exerts its repulsive effect. Taking account of the position of the Shoulder which is fixed in the base reference frame {0}, the angular range σ_i is computed from:

$$\sigma_i = \begin{cases} \arctan\left(\tan(\dfrac{\Delta\theta}{2}) + \dfrac{R_{robot}}{d_i}\right) & \text{if } \theta_i > 0 \\ \arctan\left(\tan(\dfrac{\Delta\theta}{2}) + \dfrac{L_{SB}}{d_i}\right) & \text{if } \theta_i < 0 \end{cases} \tag{6.25}$$

where $\Delta\theta$ is the angular detection range of the ith sensor, R_{robot} is the radius of the mobile platform and L_{SB} is the length of the link Shoulder-Base. When the ith obtacle is in the left of the mobile platform, i.e. $\theta_i > 0$, the robot's size should be taken into account when it passes next to an obstacle. If the obstacle is in the right, the length from the Shoulder to the center of the mobile platform should be taken into account.

The total repulsive force F_2, which pushes the mobile platform from obstacles, is

computed by the following equation:

$$F_2 = \sum_i -\kappa \, \exp\left(\frac{-d_i}{D}\right) \cos(\phi - \psi_i) = \sum_i -\kappa \, \exp\left(\frac{-d_i}{D}\right) \cos(\theta_i). \qquad (6.26)$$

where the constant coefficient κ represents the maximum strength of each repulsive force contribution, D is to control the distance from which the ith obstacle pushes the mobile platform and the term $\phi - \psi_i = -\theta_i$ is the relative direction of the obstacle to the robot heading orientation for taking account that a nonholonomic mobile platform only moves forward or backward directly.

The total moment M_1 and the total force F_2 are inputs to the Virtual Elastic System and the linear and angular velocities of the mobile platform are generated by Eq 6.19 and Eq 6.20, respectively.

6.4.2   Control of a 7-DOF anthropomorphic robotic arm

The nullspace optimisation technique which was developed in Chapter 4, allows to specify the joint-space vector $\dot{q}_{opt}$ from criterion functions which need to be optimised for adding behaviors including the joints limits avoidance and real-time obstacles avoidance.

Figure 6.10 illustrates the ability of the mobile manipulator to avoid obstacles interfering with the robotic arm while the robot is holding an handle in its hand and transporting an object with a human. When an obstacle appears below the robotic arm, the arm is lifted up. When an obstacle appears above the arm and keeps approaching the arm, the robot keeps lowering its arm to avoid collisions with the obstacle while the end effector keeps doing the transportation task without disturbances.

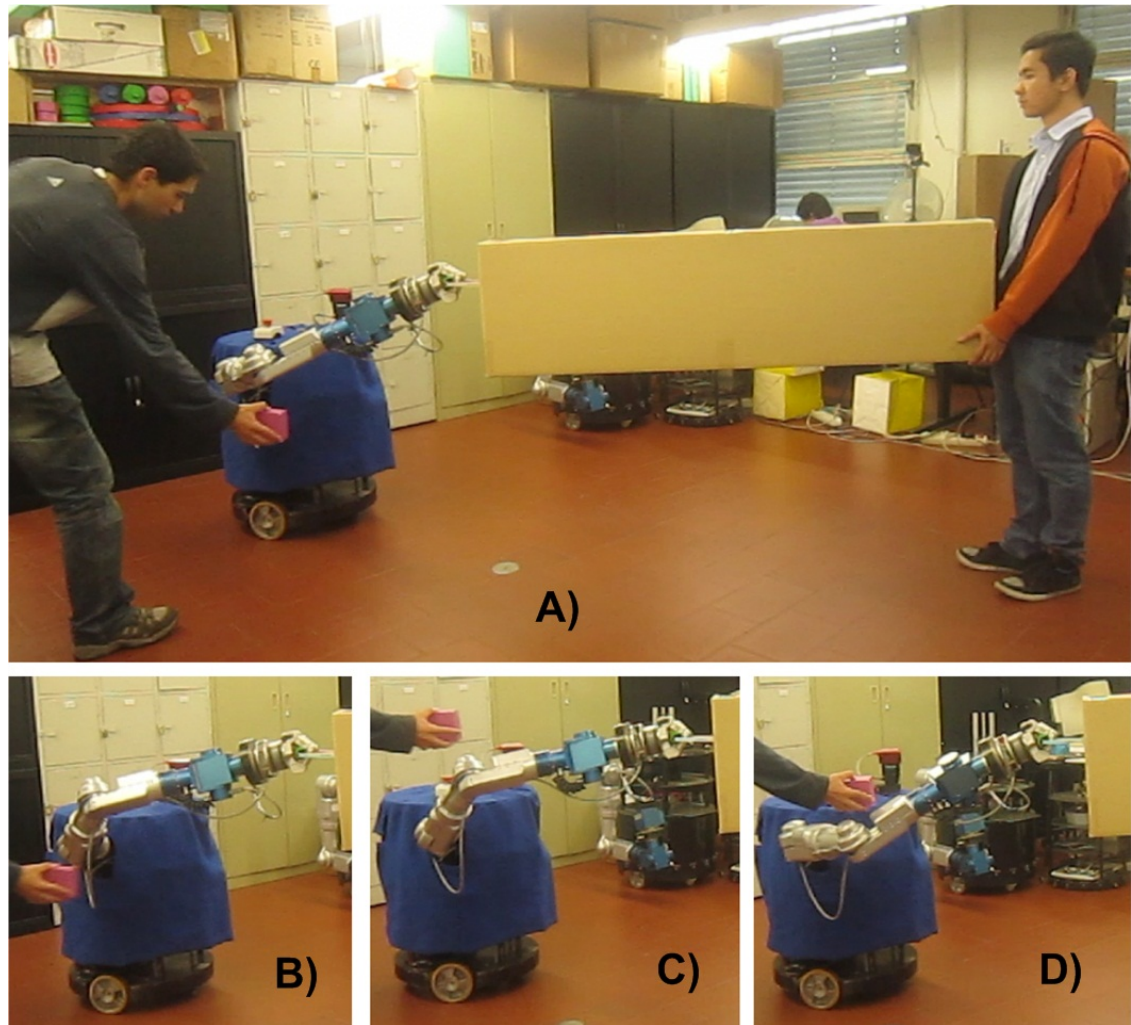Figure 6.10: Real-time obstacle avoidance and joints limit avoidance makes the robotic arm to avoid dynamic obstacles flexibly while the end effector is performing an object transportation task. When an obstacle appears below the robotic arm (A), the arm is lifted up (B). When an obstacle appears above the arm (C), the robot keeps lowering its arm when the obstacle approaches the arm (D) (Video 7).

6.5 Experiments in physical Human-Robot Interaction scenarios

This section presents experiments of controlling an anthropomorphic mobile manipulator, using the Virtual Elastic System approach in tasks that involve physical contacts with a human in unstructured and dynamic environments.

Figure 6.11 depicts a scenario in which the mobile platform needs to pass through a small passage without collisions while a human holds the robotic hand and moves the end effector. The experiment shows that the mobile platform can pass through the small passage successfully while the movement of the end effector is constrained, regardless of whether the passage is on its left (Figure 6.11-A,B,C) or right side (Figure 6.11-D,E,F).

Figure 6.12 illustrates the ability of the Virtual Elastic System for achieving flexible movements in difficult situations which require the mobile manipulator to use up its capability for avoiding collisions with obstacles. In Figure 6.12-A, the robot approaches a passage on its left side. Because the passage is smaller than its size, the repulsive force and torque from obstacles pushes the robot to rotate away (Figure 6.12-B). The robot manages to go around and avoid all obstacles flexibly while the end effector is constrained by physical contact with the human partner (Figure 6.12-C,D).

Because the Virtual Elastic System controls the relative configuration between the manipulator and the mobile platform, the VES parameters, i.e. the opening angle of the arm from the body φ_1 and the arm stretching length L_2 reflect the state of the mobile manipulator. Therefore, the robot knows its limits whenever human movements lead the robot to a dangerous situation. When values of the VES parameters reach close to their limits which are defined by physical limits of joints and geometric constraints of the mobile manipulator, the robot can use a speech synthesis to instruct the human partner to move to a more favorable direction. The robot will tell the human to move to its right if the opening angle of the arm from the body φ_1 becomes smaller than an allowed value $\varphi_{1,low}$,
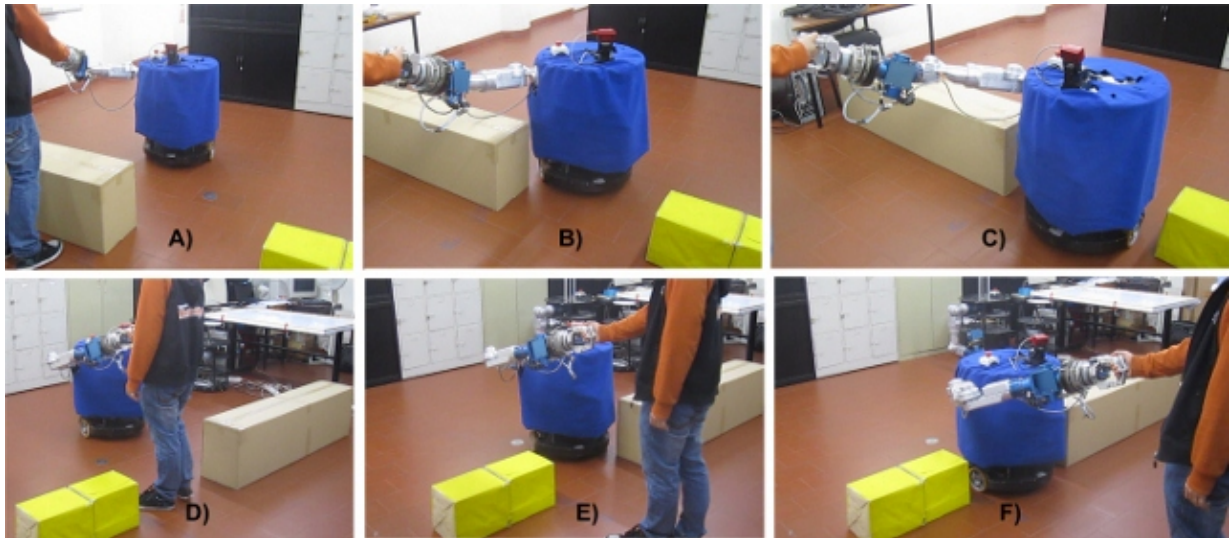
Figure 6.11: Scenario for demonstrating the obstacle avoidance of the mobile platform while the movement of the end effector is constrained by physical contacts with humans. The anthropomorphic mobile manipulator needs to pass through a small passage which is formed by obstacles on the ground while the robotic hand is held and pulled by a human. The mobile platform turns and passes through a passage on its right side (A,B,C). And the mobile platform also turns and goes through a passage on its left side without collisions (D,E,F) (Video 8).
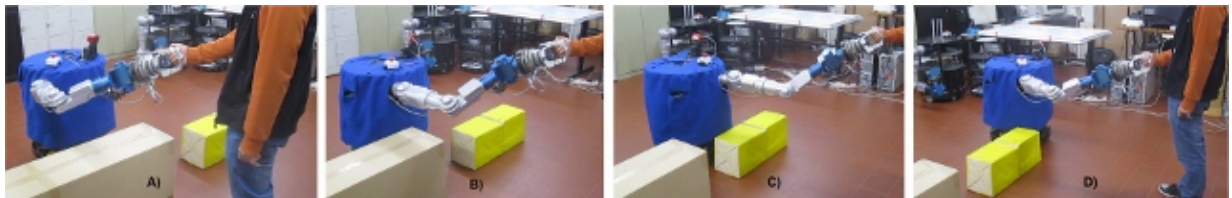
Figure 6.12: Scenario for showing that the Virtual Elastic System allows to achieve flexbile movements in difficult situations which require the mobile manipulator to use up its capability for avoiding collisions with obstacles. The robot attempts to pass through a passage on its right (A). Because the passage is smaller than the size of the mobile platform, the repulsive force and torque from obstacles pushes the robot away (B). The robot manages to go around and avoid all obstacles flexibly (C,D) while the end effector is constrained by physical contacts with the human partner (Video 9).

the arm stretching length L_2 is larger than an allowed value $L_{2,high}$ and the repulsive force F_2 is strong enough.

$$To\ right\ side\ if \begin{cases} \varphi_1 < \varphi_{1,low} \\ L_2 > L_{2,high} \\ F_2 > F_{2,high} \end{cases} \tag{6.27}$$

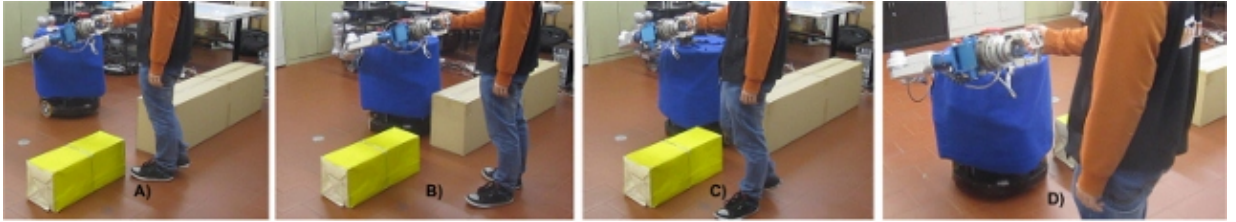This situation is shown in Figure 6.13. A human holds and moves the robotic hand

Figure 6.13: Scenario for illustrating that VES parameters allow the robot to know its limits. The robot attempts to go through a passage in its right (A). Because the passage is too small for the robot to go through, repulsive force and torque from obstacles on the ground prevent the mobile platform from forwarding while the end effector still keeps moving by forces and torques exerted by a human partner (B). The robot tells the human to support him by moving to its right (C). When the repulsive force become weak enough, the robot tells the human to proceed as he wishes and the robot passes through obstacles sucessfully (D) (Video 10).

and the mobile platform encounters obstacles which are blocking its way (Figure 6.13-A). There is a passage nearby but it is too small for the mobile manipulator to go through. The robot tries to pass the passage but repulsive force and torque from obstacles push it to rotate away (Figure 6.13-B). The mobile platform can not come closer to obstacles but the end effector still moves by physical contacts with the human. When the condition in Eq.6.27 meets i.e. the robot can not avoid obstacles itself, the robot tells the human to move to its right side so that the robot can continue to avoid obstacles (Figure 6.13-C). When repulsive forces become low enough, the robot tells the human to proceed as he wishes (Figure 6.13-D).

The mobile manipulator will tell the human to move to its left if the opening angle of the arm from the body φ_1 becomes large, the arm stretches all the way it can and the repulsive force F_2 is still strong.

$$To\ left\ side\ if \begin{cases} \varphi_1 > \varphi_{1,high} \\ L_2 > L_{2,high} \\ F_2 > F_{2,high} \end{cases} \tag{6.28}$$
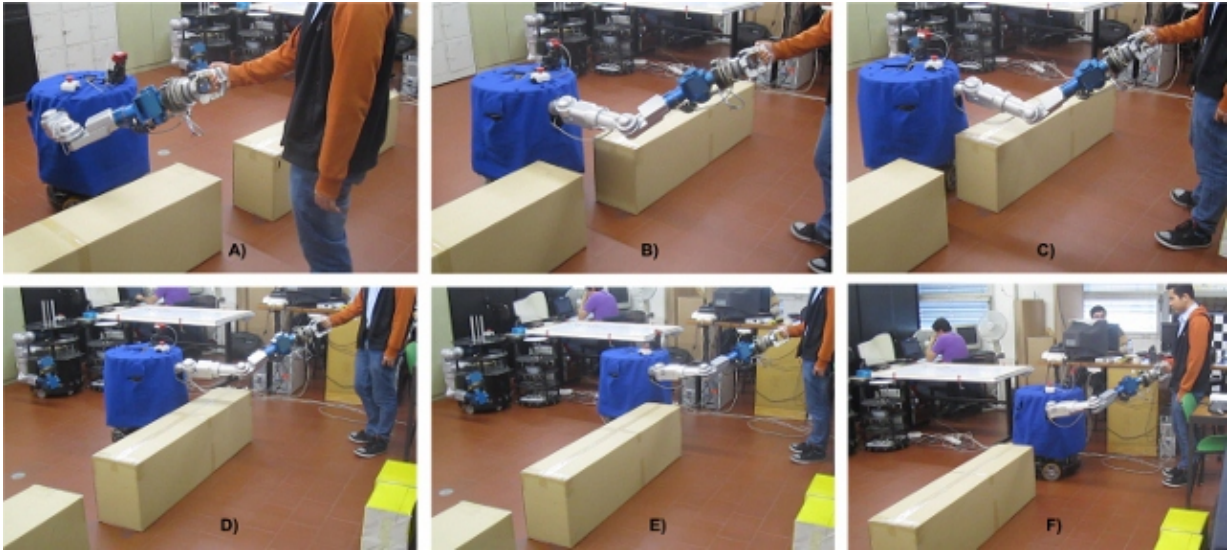

Figure 6.14: Scenario of a difficult situation which the robot can not overcome itself and it needs to tell the human to support him. The robot attempts to go through a passage in its left (A). Because the passage is too small for the robot to go through, the robot rotates and tries to go around while the end effector still keeps moving by forces and torques exerted by the human partner (B). Because the blocking obstacle is too long, the robot tries to stretch its arm but still not enough to pass through the obstacles. The robot tells the human to help him by moving to its left (C). When the repulsive force becomes low, the mobile manipulator tell the human to proceed as he wish and the robot avoids obstacles sucessfully (D,E,F) (Video 11).

An example situation is shown in Figure 6.14 where the robot is blocking by long obstacles. The mobile platform tries to pass through a nearby passage in its left but repul-

sive forces from obstacles are strong enough to push the robot away because of the small size of the passage (Figure 6.14-B). The robot tends to go around the obstacles. However, the obstacle is long, the robotic arm stretches close to its limit and the condition in Eq.6.28 meets. The anthropomorphic mobile manipulator tells the human to move to its right (Figure 6.14-C) and the robot passes the long obstacle (Figure 6.14-D,E,F).

Other states of the mobile manipulator can be acknowledged from VES parameters. For instance, if the robotic arm stretches too much, i.e. $L_2 > L_{2,high}$ without repulsive forces from obstacles, the robot says "You pull my hand so hard". Similarly, when the arm is retracted close to its limit, i.e. $L_2 < L_{2,low}$, the robot says "You push so hard". When the opening angle of the arm from the body φ_1 comes close to its limits and there is no significant repulsive force from obstacles, the robot says "You move too fast". These verbal feedback allows the human to adjust himself and thus, achieving successful physical interactions. These situations are illustrated in Figure 6.15.

The Virtual Elastic System approach allows to achieve the obstacles avoidance behavior for both the manipulator and the mobile platform simultaneously as illustrated in Figure 6.16. A human interacts with the robot by holding its hand and moves toward a small passage. There is a magenta object which is nearby the passage and high enough to interfere with the robotic arm if the mobile platform passes through the passage (Figure 6.16-A). When the robot approaches the passage, it tries to lower the arm to avoid the magenta obstacle (Figure 6.16-B,C,D). The mobile manipulator goes through the passage elegantly without any obstacle collision of the manipulator or the mobile platform (Figure 6.16-E,F,G). When there is no obstacle interfering with the robotic arm, the anthropomorphic mobile manipulator recovers its pose (Figure 6.16-H). The experiment proves the efficiency of the developed method in achieving free obstacles navigations for the whole mobile manipulator while the movement of the end effector is constrained by physical contacts with the human.

Finally, the effectiveness of the developed method in controlling anthropomorphic mobile manipulator for physical human robot interaction tasks in unstructured and dy-
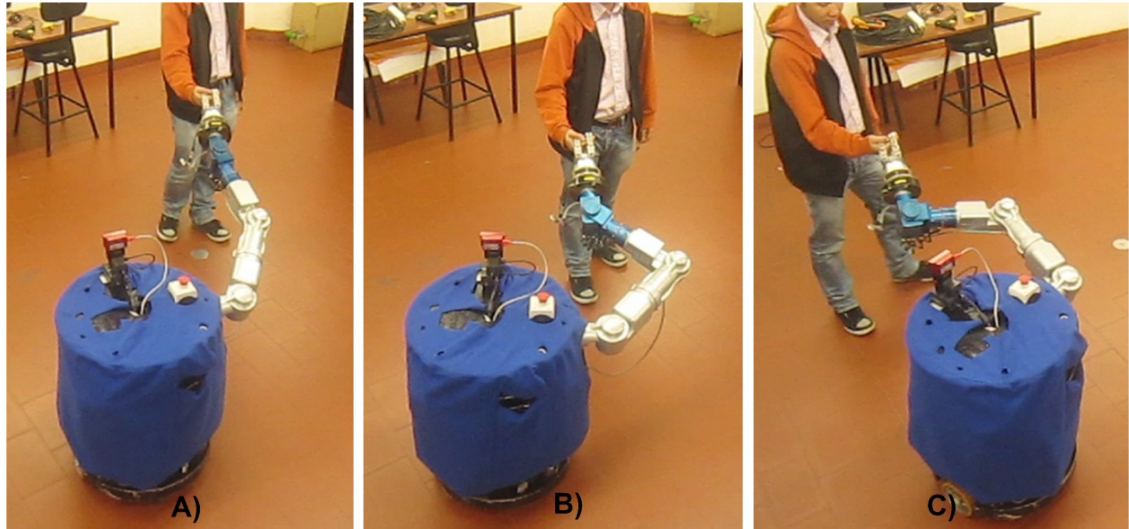
Figure 6.15: Some situations that the robot tells the human partner to adjust his physical interactions because the anthropomorphic mobile manipulator has difficulties to keep up with him. When the arm stretches too much, the robot says "You pull my hand so hard" (A). When the arm retracts close to its limit, the robot says "You push so hard" (B). When the human moves the end effector too quickly for the mobile platform to react and the opening angle of the arm from the body φ_1 becomes small and the robot says "You move too fast" (C) (Video 12).

namic environments is presented by the scenario in Figure 6.17 which covers many sub-tasks of the Human-Robot Joint Transportation. From Figure 6.17-A to Figure 6.17-I, a human partner holds the robotic hand and takes the robot to the object that he wants to transport. When the robot has difficulties to avoid a long object which appears and blocks the way of the robot (Figure 6.17-B,C) while the movement of the end effector is constrained by physical contacts with the human, the robot tells the human to move to its left (Figure 6.17-D) and the robot manages to go around the long obstacle (Figure 6.17-E). Next, it navigates safety around some obstacles (yellow ones) of an unstructured environment (Figure 6.17-F). When another human is walking near the robot (Figure 6.17-G), the stereo vision system captures coodinates of the human, based on the red color of the T-shirt of the human. Then, the robot avoids collision with the human by lifting up its
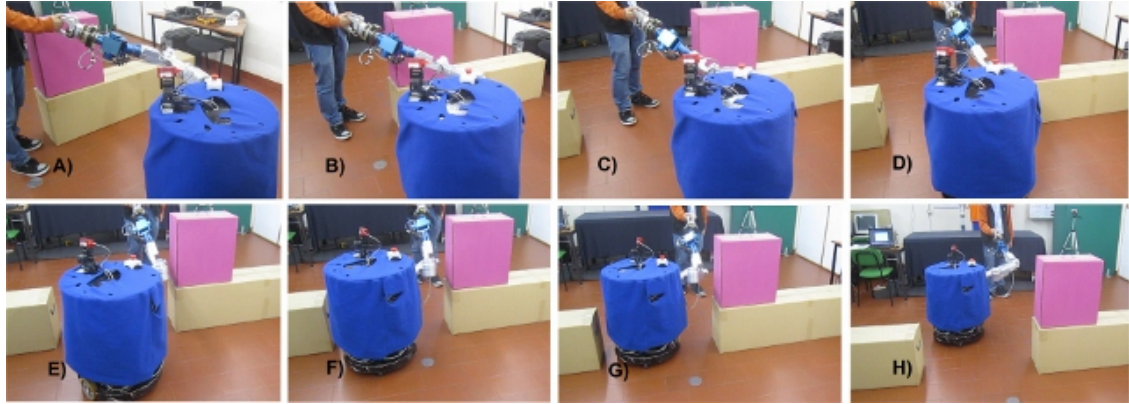
Figure 6.16: Scenario that requires the obstacles avoidance ability of both the manipulator and the mobile platform at the same time. A human takes the robot to move toward a small passage with a magenta object nearby (A). When the robot approaches the passage, it tries to lower the arm to avoid the magenta obstacle (B,C,D). The robot passes through the passage sucessfully with elegant obstacles avoidances from both the manipulator and the mobile platform (E,F,G). When there is no obstacle interfering with the robotic arm, the anthropomorphic mobile manipulator recovers its pose (H) (Video 13).

arm (Figure 6.17-H). When there is no obtacle interfering with the robotic arm, the mobile manipulator recovers its pose (Figure 6.17-I). The robot knows it has reached to the object that needs to be transported when the human partner lowers the robotic hand down enough (Figure 6.17-J). The robot rotates its neck and looks at the green handle of the object. After that, the robot opens its hand, comes closer to the target object and picks up the handle (Figure 6.17-K). The object is lifted up (Figure 6.17-L) and the mobile manipulator transports it cooperatively with the human around the yellow obstacle distributed on the ground (Figure 6.17-M). When a long obstacle appears and blocks its way (Figure 6.17-N), the robot tells the human partner to move to its left (Figure 6.17-O) and avoids collisions with the obstacle successfully (Figure 6.17-P). When a human passes close to the robot, the robot lowers its arm to avoid him (Figure 6.17-Q). When the object has reached to its desired position, the human partner lowers the load. The robot opens its hand and releases the handle.

Figure 6.17: Scenario for illustrating the Human-Robot Joint Transportation task. A human partner holds the robotic hand and takes the robot to the object that he wants to transport (from A to I) with obstacles avoidance. After grasping the handle (J,K,L), the robot transports an object with a human partner in dynamic environment (from M to U) (Video 14).

6.6 Extensions of Virtual Elastic System on holonomic mobile platforms or higher DOF manipulators

This section is dedicated for further dicussions about the proposed Virtual Elastic System approach. As previously stated in Section 6.3, two parameters $\{\varphi_1, L_2\}$ among three VES parameters, i.e. the opening angle of the arm from the body φ_1, the arm stretching length L_2 and the wrist angle φ_3, are chosen to be controlled independently in anthropomorphic mobile manipulators whose the mobile platform is nonholonomic. In these mobile manipulators, continuous control of the wrist angle φ_3 yields a poor performance.
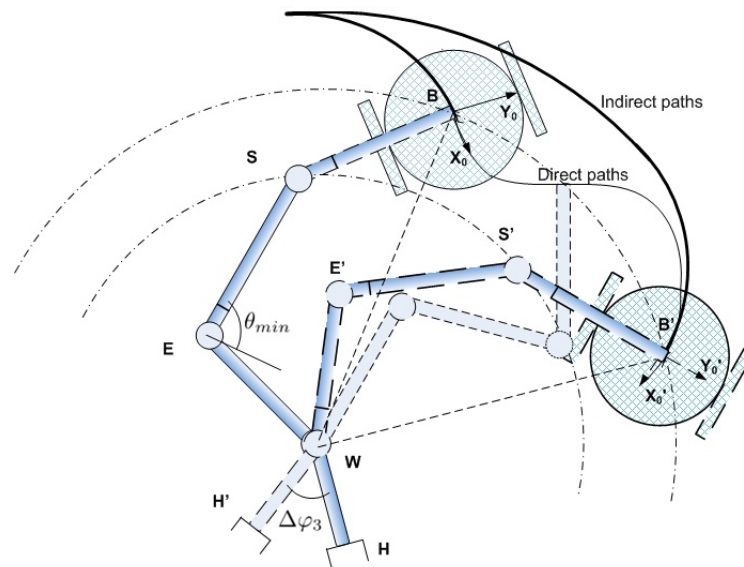

Figure 6.18: Control of the parameter φ_3 degrades the performance of the anthropomorphic mobile manipulators whose the mobile platform is nonholonomic. A small change of φ_3 requires the mobile platform to move a considerable distance and direct paths are usually unfeasible because of physical limits of joints or geometric contraints of the mobile manipulator. A considerable amount of time needs to be spent so that the robot recovers the wrist angle φ_3 by indirect paths.

Lets consider that the wrist of the manipulator rotates a small angle of $\Delta\varphi_3$ as illustrated in Figure 6.18. Because of the length of the robotic arm, a small change $\Delta\varphi_3$

requires the mobile platform to move a considerable distance from the point B to B' if the angle φ_3 is controlled. The nonholonomic mobile platform can move either in direct paths or indirect paths to recover the wrist angle. Direct paths allows the mobile platform to react quickly but are usually unfeasible because of physical limits of joints or geometric contraints of the mobile manipulator. They are only suitable for manipulators whose Shoulder-Base link is short, relative to the arm length and thus converging to situations of top, center mounted manipulators. Indirect paths, which are always available, should be used for anthropomorphic robotic arm. However, the robot needs to spend a considerable amount of time for recovering the wrist angle φ_3 by indirect paths.

Therefore, the wrist angle needs to be kept away from its limits by another solution instead of controlling it for a desired value. Normally, the value of φ_3 rarely enters into a critical region because whenever the end effector moves forward, the angle φ_3 will be restored to a value in the middle of its range. This issue is illustrated by a simulation in Figure 6.19. The end effector moves in straight lines (the green path) and the mobile platform tries to recover the pose of the manipulator by using the Virtual Elastic System (the red path). The coordinates of important points such as the center and the orientation of the mobile platform, the center of the Shoulder, the Wrist and the Hand of the manipulator are computed in Matlab^{TM} and the graphical visual is provided by plotting their x and y coordinates in a 2D graph. The unstructured environment is simulated by the dynamic appearance of obstacles on the ground, represented by magenta circles. The simulation shows that forward movements of the end effector will restore the angle φ_3 regardless of whether the wrist angle φ_3 becomes too large (Figure 6.19-C) or too small (Figure 6.19-E). The experiment in Figure 6.20 also proves that forward movements of the end effector restore φ_3 from its limits. Therefore, the forward movement of the end effector can be a solution for keeping the wrist angle φ_3 in its limits without slowing down the reaction of the mobile platform.
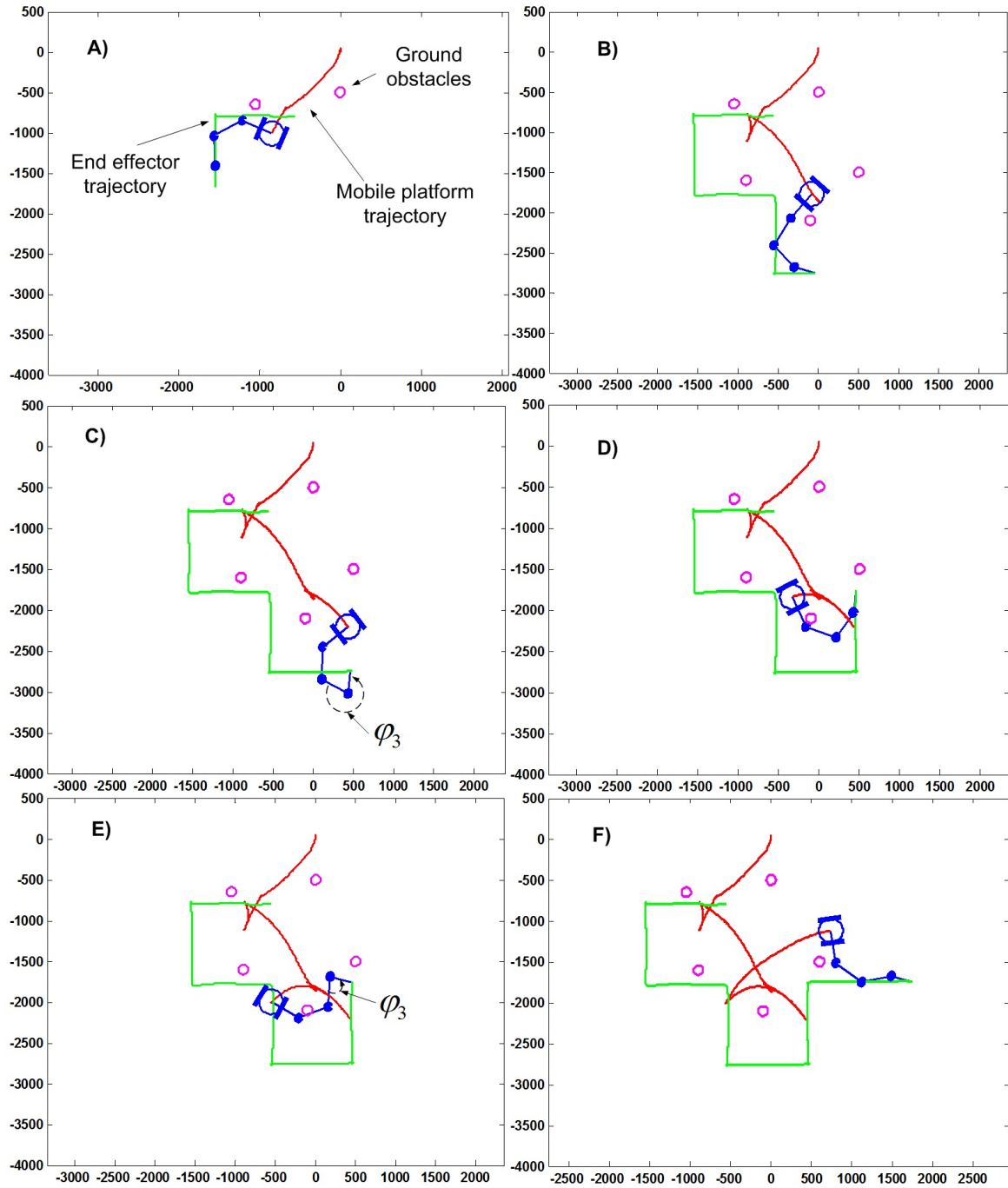
Figure 6.19: Simulation shows that whenever the end effector moves forward, the angle φ_3 converges to a value in the middle of its range regardless of whether φ_3 is near its upper limit (C) or lower limit (E).
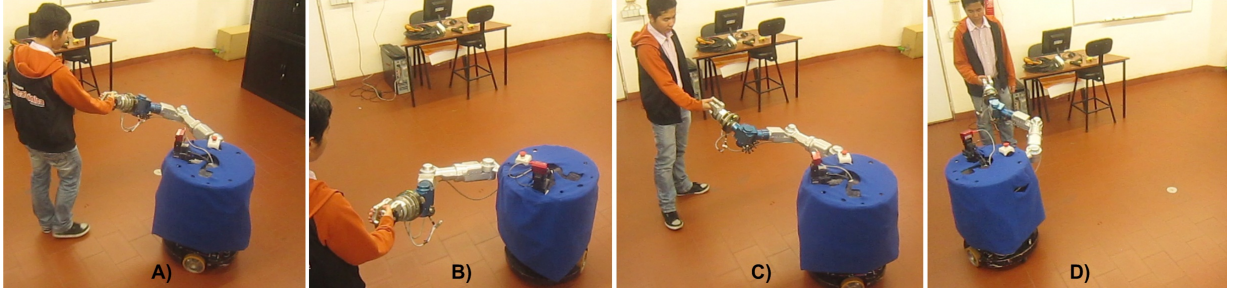
Figure 6.20: Experiment shows that the wrist angle φ_3 will be restored to a value in the middle of its range whenever the end effector moves forward regardless of whether the angle φ_3 become too large (A) or too small (C) (Video 15).

6.6.1 Extensions for anthropomorphic mobile manipulators with a holonomic mobile platform

In anthropomorphic mobile manipulators with a holonomic mobile platform, the Virtual Elastic System can be extended as in Figure 6.21. Because the holonomic mobile platform can move in any direction directly, no repulsive moment is applied on the mobile platform by obstacles. The effect of obstacles on the mobile platform is represented as a total repulsive force F_{obs}, which is computed from the following equation:

$$\vec{F}_{obs} = \left(\sum_i -\kappa \, \exp\left(\frac{-d_i}{D}\right) \cos(\phi - \psi_i) \right) \vec{e}_{X0}$$

$$+ \left(\sum_i \kappa \, \exp\left(\frac{-d_i}{D}\right) \sin(\phi - \psi_i) \right) \vec{e}_{Y0} \tag{6.29}$$

$$= \left(\sum_i -\kappa \, \exp\left(\frac{-d_i}{D}\right) \cos(\theta_i) \right) \vec{e}_{X0}$$

$$+ \left(\sum_i -\kappa \, \exp\left(\frac{-d_i}{D}\right) \sin(\theta_i) \right) \vec{e}_{Y0} . \tag{6.30}$$

where d_i is the distance from the ith obstacle to the center of the mobile platform. The coefficient κ determines the maximum strength of each repulsive force contribution and can be chosen as a constant. The coefficient D is to control the distance from which the ith obstacle exerts its repulsive force to push the mobile platform. The term $\phi - \psi_i$ is the
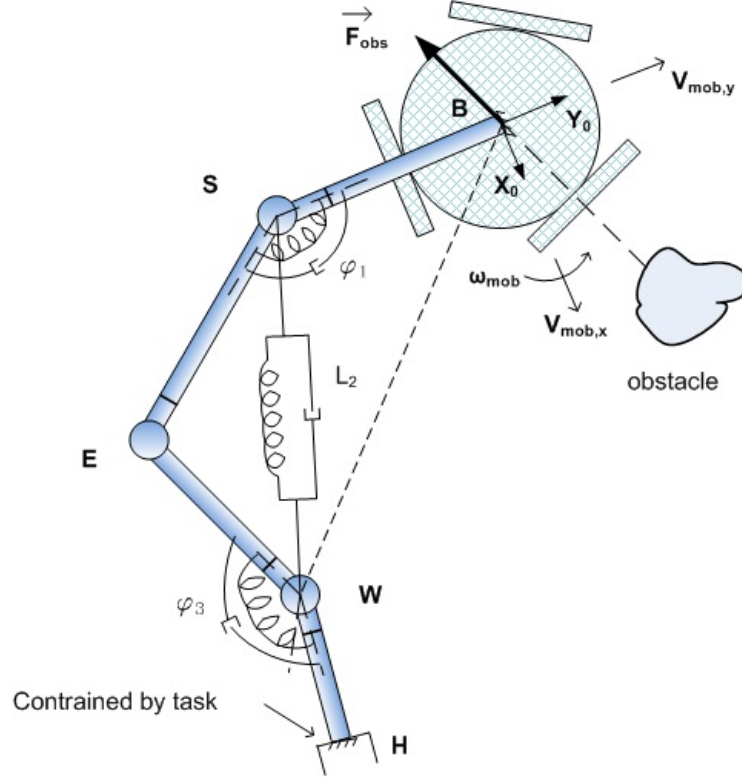
Figure 6.21: Virtual Elastic System for holonomic mobile platforms

relative direction from the robot to the ith obstacle that is equal to the additive inverse of θ_i, the relative pointing angle of the ith distance sensor which is constant due to the sensor position. Therefore, the obstacle avoidance behavior for the mobile platform is achieved just by sensed distances from distance sensors without information about the position and orientation of the mobile platform and obstacles in the world.

Three VES parameters $\{\varphi_1, L_2, \varphi_3\}$ can be controlled independently and governed by the following VES equations:

$$K_{m1}\ddot{\varphi}_1 + K_{v1}\dot{\varphi}_1 + K_{e1}(\varphi_1 - \varphi_{1,0}) = 0, \tag{6.31}$$

$$K_{m2}\ddot{L}_2 + K_{v2}\dot{L}_2 + K_{e2}(L_2 - L_{2,0}) = -K_{f2}F_{obs,x}, \tag{6.32}$$

$$K_{m3}\ddot{\varphi}_3 + K_{v3}\dot{\varphi}_3 + K_{e3}(\varphi_3 - \varphi_{3,0}) = K_{f3}F_{obs,y}. \tag{6.33}$$

where the current value of the opening angle of the arm from the body φ_1 and the arm

stretching length L_2 are calculated from Eq.6.5 and Eq.6.13 respectively. The current value of the wrist angle φ_3 is computed by:

$$\varphi_3 = \begin{cases} \arccos\left(\dfrac{\vec{WE} \cdot \vec{WH}}{L_{WE}\ L_{WH}}\right) & \text{if } (\vec{WE} \times \vec{WH})_z > 0 \\[4mm] 2\pi - \arccos\left(\dfrac{\vec{WE} \cdot \vec{WH}}{L_{WE}\ L_{WH}}\right) & \text{if } (\vec{WE} \times \vec{WH})_z < 0 \end{cases} \tag{6.34}$$

where W, E, H are the position of the Wrist, Elbow and the Hand in the base reference frame {0} respectively and L_{WE}, L_{WH} are the length of links Wrist-Elbow and Wrist-Hand. The term $(\vec{WE} \times \vec{WH})_z$ is the z component of the cross product of the vector $\vec{WE}$ and $\vec{WH}$.

The VES parameters and coefficients in Eq 6.31, 6.32 and 6.33 changes dynamically in the same way which has been presented in Section 6.3 for the mobile manipulator with a nonholonomic platform. After the new state of the Virtual Elastic System is generated, the changes in VES parameters, i.e. $\dot{\varphi}_1$, $\dot{L}_2$ and $\dot{\varphi}_3$, will be converted into the velocity of the holonomic mobile platform, i.e. $V_{mob,x}$, $V_{mob,y}$ and ω_{mob}.

$$\omega_{mob} = \dot{\varphi}_1, \tag{6.35}$$

$$V_{mob,x} = -\dot{L}_2, \tag{6.36}$$

$$V_{mob,x} = -\dot{\varphi}_3\ x_W. \tag{6.37}$$

where x_W is the x coordinate of the Wrist in the reference frame {0}.

The simulation in Figure 6.22 illustrates the control of an anthropomorphic mobile manipulator with a 7-DOF manipulator, side-mounted on a holonomic mobile platform in an unstructured environment. The mobile platform avoids successfully dynamic obstacles which appear in its vicinity, while maintaining a desired pose for the mobile manipulator.
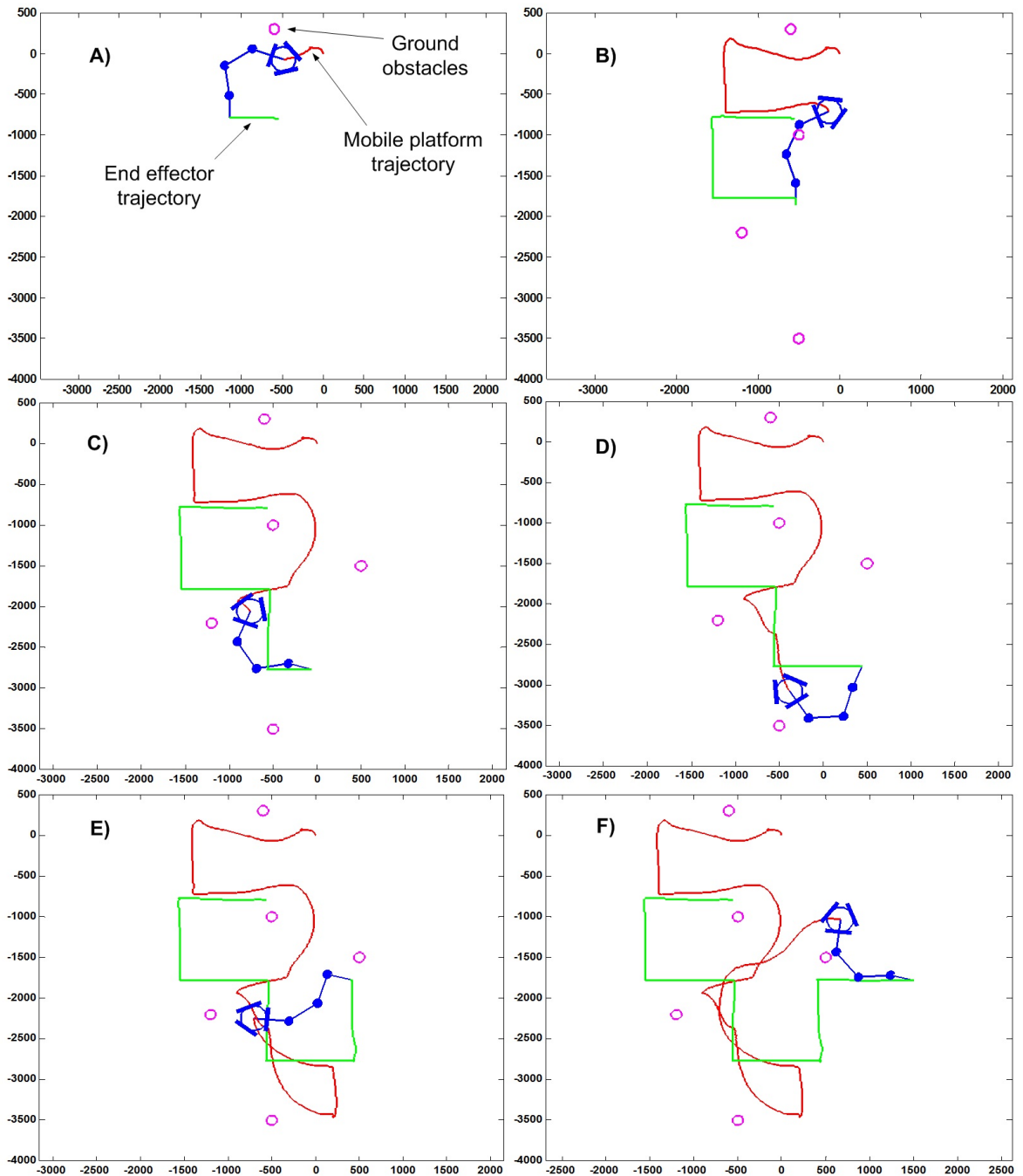
Figure 6.22: Simulation of controlling a 7-DOF manipulator, side-mounted on a holonomic mobile platform in an untructured environment by using the Virtual Elastic System approach. (Video 16)

6.6.2   Extensions for mobile manipulators with higher degrees of freedom manipulators
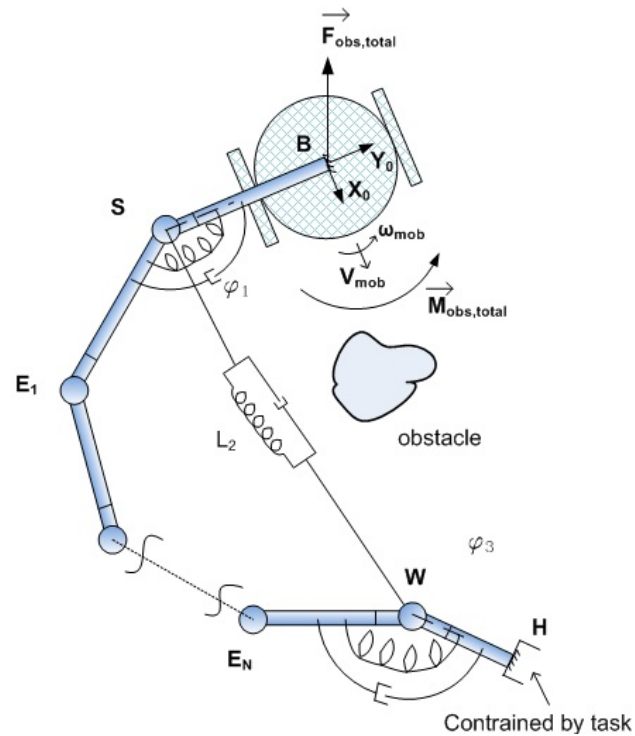

Figure 6.23: Virtual Elastic System for other mobile manipulators with higher degrees of freedom manipulators

The Virtual Elastic System can also be adapted for other mobile manipulators with higher degrees of freedom (Figure 6.23). Three VES parameters, including φ_1 that represents the opening angle of the robotic arm from its body, L_2 that features the reaching and retracting ability of the robotic arm, and φ_3 that is the wrist angle, are still chosen for characterizing the relative position of the mobile platform with the end effector.

For controlling these parameters, depending on whether the mobile manipulator is a nonholonomic or holonomic one, the respective control strategy in Section 6.3 or in Section 6.6.1 can be applied. Figure 6.24 depicts a simulation scenario for controlling of a 11-DOF manipulator, side-mounted on a nonholonomic mobile platform in a dynamic obstacle environment, while Figure 6.25 presents a simulation of controlling a 11-

Figure 6.24: Simulation of controlling a 11-DOF manipulator, side-mounted on a nonholo-nomic mobile platform in an untructured environment by using the Virtual Elastic System approach
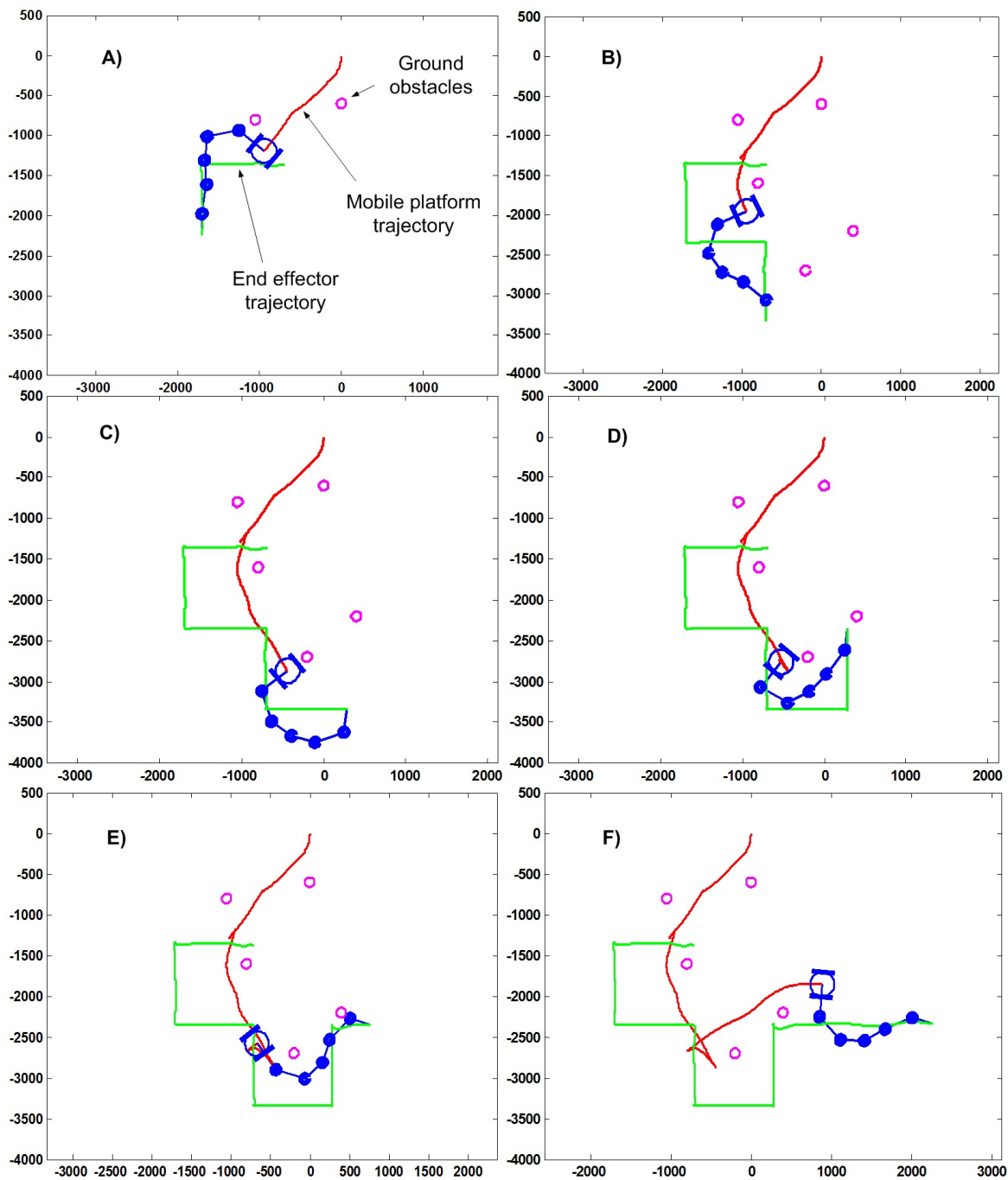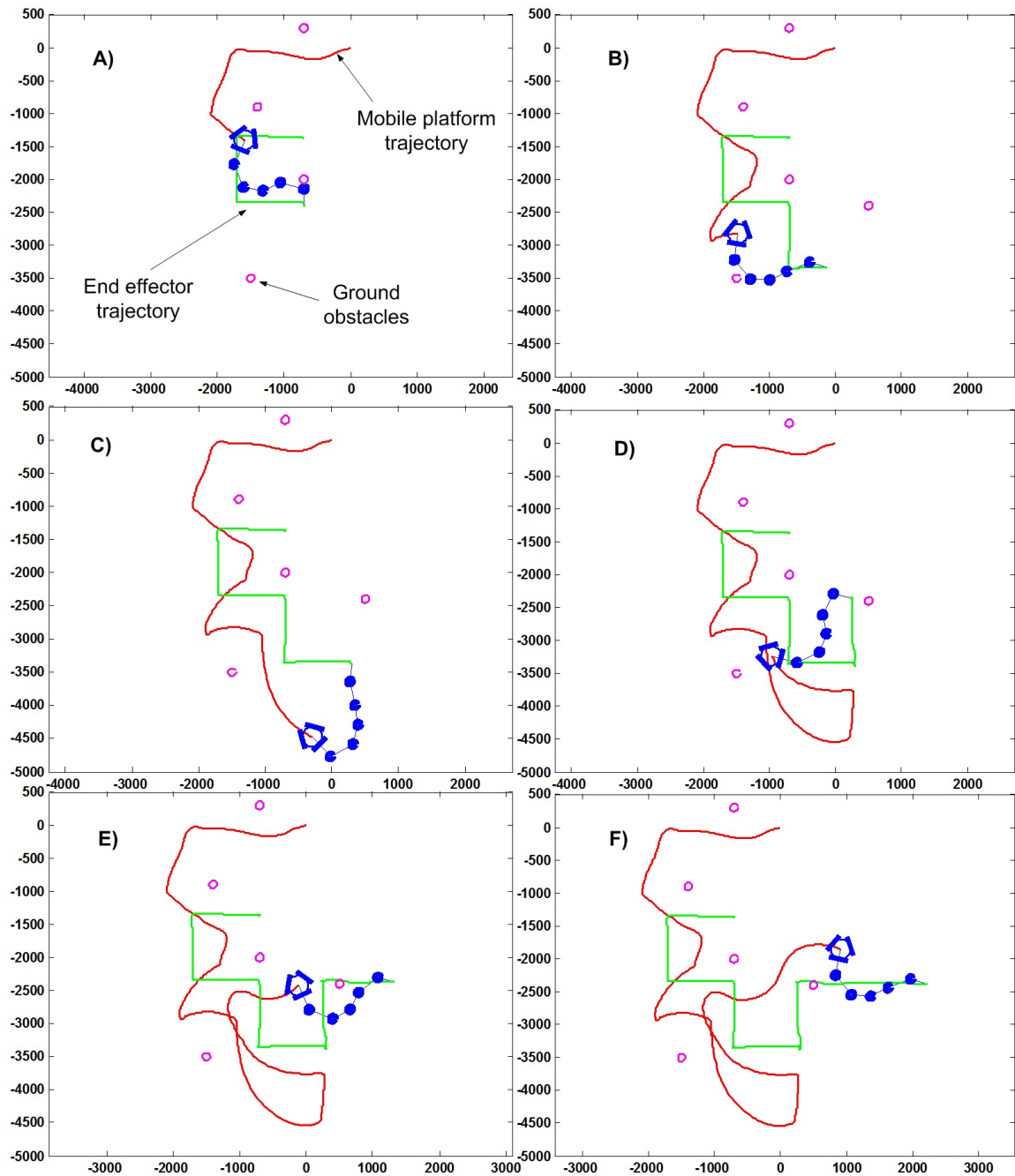
Figure 6.25: Simulation of controlling a 11-DOF manipulator, side-mounted on a holonomic mobile platform in an untructured environment by using the Virtual Elastic System approach

DOF manipulator, side-mounted on a holonomic mobile platform. The robots have been manipulated with high dexterity and flexibilty, proving the efficiency of the developed method.

6.7 Conclusion

In this chapter, a novel Virtual Elastic System approach is proposed to control anthropomorphic mobile manipulators which are capable to provide friendly interactions with humans but possess more geometric and kinematic constraints than conventional centered and top mounted mobile manipulators. The Virtual Elastic System maintains a desired pose for the mobile manipulator flexibly, which enables the combination of an Inverse Differential Kinematics for the redundant manipulator and a Dynamical System for the nonholonomic mobile platform. Experiments which involves physical human contact and the Human-Robot Joint Transportation, have proved the effectiveness of the developed method for physical human-robot interaction tasks with free obstacles movements for both the manipulator and the mobile platform simultaneously in unstructured and dynamic environments. Extensions for mobile manipulators with holonomic mobile platform or higher degrees of freedom manipulator (11-DOF) have been illustrated with simulations, proving the Virtual Elastic System as a powerful approach for controlling anthropomorphic mobile manipulators in particular and also mobile manipulators in general.

Chapter 7

Conclusion

7.1   Summary and discussion

In this dissertation, the differential kinematics of a 7-DOF anthropomorphic manipulator has been studied thoroughly, including the construction of the Jacobian matrix, the Jacobian decomposition technique which allows to decompose the Jacobian into three simple matrix and the redundancy exploitation. The singularity analysis is carried out by a proposed technique to explore exhausively singularities of the redundant robotic arm.

The thesis has also contributed with a real-time obstacle avoidance strategy for controlling anthropomorphic robotic arms in dynamic obstacle environments, taking account of sudden appearances or disappearances of mobile obstacles, while ensuring the safety of the robotic arm from exceeding the physical limits of joints in terms of position, velocity and acceleration. The singularities avoidance is also included. The efficiency of the control method is validated through simulations and also experiments.

A method for compensating force errors due to changes in the orientation of end effectors, independent of structures of force sensors, has been developed to achieve higher efficiency in force control applications. The need of the method and also its effectiveness are illustrated through experiments.

A novel method, so-called the Virtual Elastic System, is proposed to control mobile manipulators for physical Human-Robot Interaction tasks in dynamic environments, which enables the combination of an Inverse Differential Kinematics for redundant robotic arms and a Dynamical Systems approach for nonholonomic mobile platforms. Experiments with a 7-DOF robotic arm, side-mounted on a nonholonomic mobile platform, are presented with the whole robot obstacle avoidance, proving the efficiency of the developed method in pHRI scenarios, more specifically, cooperative human-robot object transportation tasks in dynamic environments. Extensions of the method for other mobile manipulators with holonomic mobile platforms or higher degrees of freedom manipulators (11-DOF) are also demonstrated through simulations.

The control software in C++ (Figure A.1) and the simulator in Matlab (Figure A.3) are user-friendly. User can select the task which needs to be performed. New tasks can be added to the list of available task. These resources can be used and extended for other research projects in the Anthropomorphic and Mobile Robotics Laboratory of the University of Minho.

7.2 Outlook

The work described in this dissertation offers various possibilities for further research. One possibility is imposing human-like movements for the manipulator. In the control of the 7-DOF anthropomorphic robotic arm, the performance criteria for the joint limits avoidance, the singularity avoidance and the obstacle avoidance behaviors are constructed and optimised in order to achieve safe movements in dynamic environments. The studies about the performance criterion of human-liked movements can be carried out for achieving more human-like movements.

The proposed force and torque compensation method allows to eliminate the effect of the end effector orientation on force and torque readings, and also static errors from the end effector and the force sensor. The method can be extended with a method for

eliminating dynamic errors which become considerable in fast movements with high accelerations. One possibility is modelling the end effector as a mass and determining its coordinates in the force sensor reference frame.

The proposed Virtual Elastic System approach allows to maintain a desired pose for many types of mobile manipulators with a side-mounted robotic arm. The control of mobile manipulators with two side-mounted robotic arms is an interesting possibility for extending the work presented here. In bimanual object manipulation, we need to cope the synchronization, motor control and force distribution between two arms.

References

Bayle, B., Fourquet, J., & Renaud, M. (2003). Manipulability of wheeled mobile manipulators: Application to motion generation. *The International Journal of Robotics Research*, 565-581.

Bicho, E., Louro, L., Hipolito, N., Monteiro, S., & Erlhagen, W. (2003). Motion control of a mobile robot transporting a large size object in cooperation with a human: a nonlinear dynamical systems approach. *Proceedings of the IEEE/RSJ International Conference on Intelligent Robots and Systems*, 197-203.

Bicho, E., Mallet, P., & Schoner, G. (2000). Target representation on an autonomous vehicle with low-level sensors. *The International Journal of Robotics Research*, 424-447.

Brock, O., & Khatib, O. (2002). Elastic strips: A framework for motion generation in human environments. *The International Journal of Robotics Research*, 1031-1052.

Buerger, S. P., & Hogan, N. (2007). Complementary stability and loop shaping for improved human–robot interaction. *IEEE Transaction on robotics*, 232 - 244.

Calinon, S., Sardellitti, I., & Caldwell, D. G. (2010). Learning-based control strategy for safe human-robot interaction exploiting task and robot redundancies. *Proceedings of the IEEE/RSJ International Conference on Intelligent Robots and Systems*, 249 - 254.

Cheng, F.-T., Chen, J.-S., & Kung, F.-C. (1998). Study and resolution of singularities for a 7-dof redundant manipulator. *IEEE Transaction on industrial electronics*, *43*.

Costa e Silva, E. (2011). *Reaching, grapsing and manipulation in anthropomorphic robot systems*. Phd thesis, University of Minho, Portugal.

Costa e Silva, E., Costa, F., Bicho, E., & Erlhagen, W. (2011). Nonlinear optimization for human-like movements of a high degree of freedom robotics arm-hand system. *11th International Conference on Computational Sciences and Applications (ICCSA 2011),Lecture Notes in Computer Science, Springer-Verlag, 6784,Part III*, 327-342.

Craig, J. J. (2005). *Introduction to robotics* (Third ed.). Pearson Prentice Hall.

Dombre, E., & Khalil, W. (2007). *Modeling, performance, analysis and control of robot manipulators*. ISTE Ltd.

Ellekilde, L.-P., & Christensen, H. I. (2009). Control of mobile manipulator using the dynamical systems approach. *Proceedings of the IEEE Intermional Conference on Robotics and Automation*, 1370-1376.

Flacco, F., & Luca, A. D. (2011). Residual-based stiffness estimation in robots with flexible transmissions. *Proceedings of the IEEE Intermional Conference on Robotics and Automation*, 5541 - 5547.

Iossifidis, I., & Schoner, G. (2009). Dynamical systems approach for the autonomous avoidance of obstacles and joint-limits for an redundant robot arm. *IEEE International Conference on Robotics and Automation*, 1370-1376.

Janiak, M., & Tchon, K. (2010). Towards constrained motion planning of mobile manipulators. *Proceedings of the IEEE Intermional Conference on Robotics and Automation*, 4990-4995.

Khatib, O. (1986). Real-time obstacle avoidance for manipulators and mobile robots. *The International Journal of Robotics Research*.

Lawitzky, M., MÂÍortl, A., & Hirche, S. (2010). Load sharing in human-robot cooperative manipulation. *Proceedings of the IEEE International Symposium on Robot and Human Interactive Communication*, 185-191.

Lee, K.-K., & Buss, M. (2007). Obstacle avoidance for redundant robots using jacobian transpose method. *Proceedings of the IEEE/RSJ International Conference on Intelligent Robots and Systems*.

Liu, Y., Liang, B., Sun, K., & Jiang, Y. (2008). Research on obstacle avoidance of redundant robots based on geometric models. *ISSCAA - International Symposium on Systems and Control in Aerospace and Astronautics*.

Liu, Y., Zhao, J., & Xie, B. (2010). Obstacle avoidance for redundant manipulators based on a novel gradient projection method with a functional scalar. *Proceedings of the IEEE International Conference on Robotics and Biomimetics*, 1704-1709.

Luca, A. D., Oriolo, G., & Giordano, P. R. (2006). Kinematic modeling and redundancy resolution for nonholonomic mobile manipulators. *Proceedings of the IEEE Intermional Conference on Robotics and Automation*, 1867-1873.

Luca, A. D., Oriolo, G., & Giordano, P. R. (2010). Kinematic control of nonholonomic mobile manipulators in the presence of steering wheels. *Proceedings of the IEEE Intermional Conference on Robotics and Automation*, 1792-1798.

Malheiro, T., Machado, T., Monteiro, S., Erlhagen, W., & Bicho, E. (2012). Object transportation by a human and a mobile manipulator: a dynamical systems approach. *Proceedings of the International Conference Robotica*, 27-32.

Nozaki, K., & Murakami, T. (2009). A motion control of two-wheels driven mobile manipulator for human-robot cooperative transportation. *Proceedings of the IEEE International Conference on Industrial Electronics*,

1574 - 1579.

Papadopoulos, E., & Poulakakis, J. (2000). Planning and model-based control for mobile manipulators. *Proceedings of the IEEE/RSJ International Conference on Intelligent Robots and Systems*, 1-6.

Portillo-Velez, R., Rodriguez-Angeles, A., & Cruz-Villar, C. A. (2011). An optimal admittance approach for physical human-robot interaction. *Proceedings of the IEEE International Conference on Electrical Engineering Computing Science and Automatic Control*, 1-6.

Quigley, M., Asbeck, A., & Ng, A. (2011). A low-cost compliant 7-dof robotic manipulator. *Proceedings of the IEEE International Conference on Robotics and Automation*, 6051 - 6058.

Santis, A. D., Siciliano, B., Luca, A. D., & Bicchi, A. (2007). An atlas of physical human robot interaction. *Mechanism and Machine Theory*.

Seraji, H., Long, M. K., & Lee, T. S. (1993). Motion control of 7-dof arms: The configuration control approach. *IEEE Transactions on Robotics and Automation*, *9*, 125-139.

Shimizu, M., Yoon, W.-K., Kitagaki, K., & Kosuge, K. (2008). Analytical inverse kinematic computation for 7-dof redundant manipulators with joint limits and its application to redundancy resolution. *IEEE Transactions on Robotics*, *24*.

Siciliano, B., & Khatib, O. (Eds.). (2008). *Handbook of robotics*. Berlin, Germany: Springer-Verlag.

Soares, R., Bicho, E., Machado, T., & Erlhagen, W. (2007). Object transportation by multiple mobile robots controlled by attractor dynamics: theory and implementation. *Proceedings of the IEEE/RSJ International Conference on Intelligent Robots and Systems*, 937-944.

Takubo, T., Arai, H., Hayahibara, Y., & Tanie, K. (2002). Human-robot cooperative manipulation using a virtual nonholonomic constraint. *The International Journal of Robotics Research*, 541-553.

Tarokh, M., & Kim, M. (2007). Inverse kinematics of 7-dof robots and limbs by decomposition and approximation. *IEEE Transactions on Robotics*, *23*, 595-600.

Tchon, K., & Jakubiak, J. (2002). Extended jacobian inverse kinematics algorithms for mobile manipulators. *Journal of Robotic Systems*, 443-454.

Tolani, D., Goswami, A., & Badler, N. I. (2000). Real-time inverse kinematics techniques for anthropomorphic limbs. *Graphical Models*.

Vannoy, J., & Xiao, J. (2008). Real-time adaptive motion planning (ramp) of mobile manipulators in dynamic environments with unforeseen changes. *IEEE Transaction on robotics*, 1199-1212.

Wang, J., Li, Y., & Zhao, X. (2010). Inverse kinematics and control of a 7-dof redundant manipulator based on the closed-loop algorithm. *International Journal of Advanced Robotic Systems*, *7*.

Whitney, D. (1972). The mathematics of coordinated control of prosthetic arms and manipulators. *Transac-*

tion of ASME, Journal of Dynamic Systems, Measurement, and Control, 94, 303-309.

Wyrobek, K. A., Berger, E. H., der Loos, H. M. V., & Salisbury, J. K. (2008). Towards a personal robotics development platform: Rationale and design of an intrinsically safe personal robot. *Proceedings of the IEEE Intermational Conference on Robotics and Automation*, 2165 - 2170.

Zinn, M., Khatib, O., Roth, B., & Salisbury, J. K. (2004). A new actuation approach for human friendly robot design. *The International Journal of Robotics Research*, 379 - 398.

Appendix A

Developed control software and simulators

During the work, a control software for controlling the anthropomorphic robotic systems, i.e. ARoS and Dumbo, has been developed in C++ and organised into classes for the ease of future developments (Figure A.1). The software allows to connect to many devices which are available in the robots. It can be extended by adding new tasks to the list of the available tasks.

In addition, a Differential Kinematics simulator has been developed in Matlab^{TM} to simulate the control of a 7-DOF manipulator in velocity contrained tasks (Figure A.2). Obstacles can be added to the workspace at a specific time to simulate the obstacle avoidance behavior. The joint values, which are integrated from the joint velocities, are used to update the new pose of the manipulator. The graphical models in 3D, developed previously by Eliana during her PhD thesis, receives joint values as inputs to update the robotic arm configuration and gives graphical visual of movements.

Another simulator, which allows to simulate the control of several types of mobile manipulators, including a 7-DOF manipulator, side-mounted on a nonholonomic mobile platform, a 7-DOF manipulator, side-mounted on a holonomic mobile platform, a 11-DOF
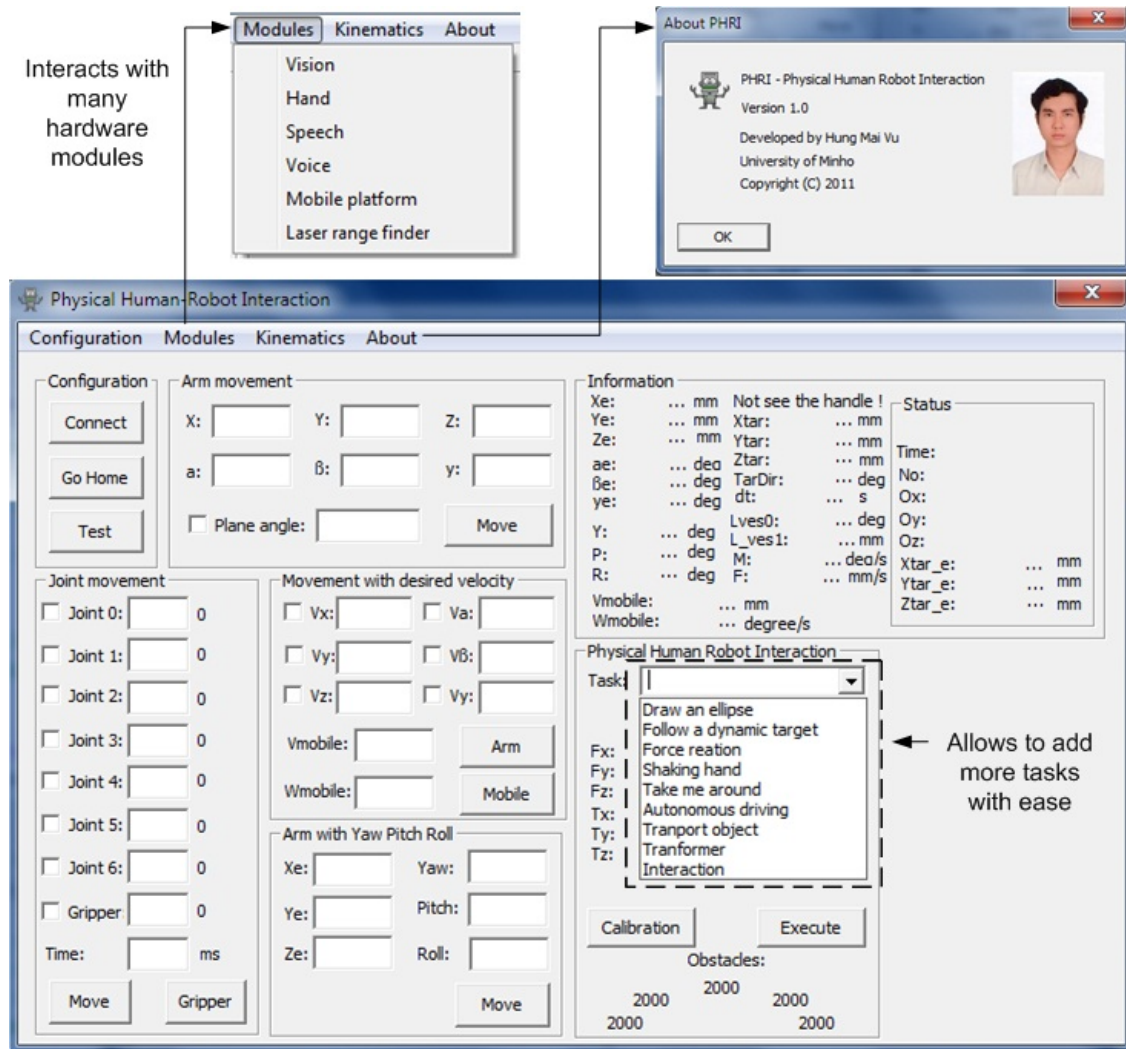
Figure A.1: The developed control software for controlling the anthropomorphic robotic systems, ARoS and Dumbo

manipulator, side-mounted on a nonholonomic mobile platform and a 11-DOF manipulator, side-mounted on a holonomic mobile platform, have been developed in Matlab^{TM} (Figure A.3). New types of mobile manipulators can be added to the simulator.
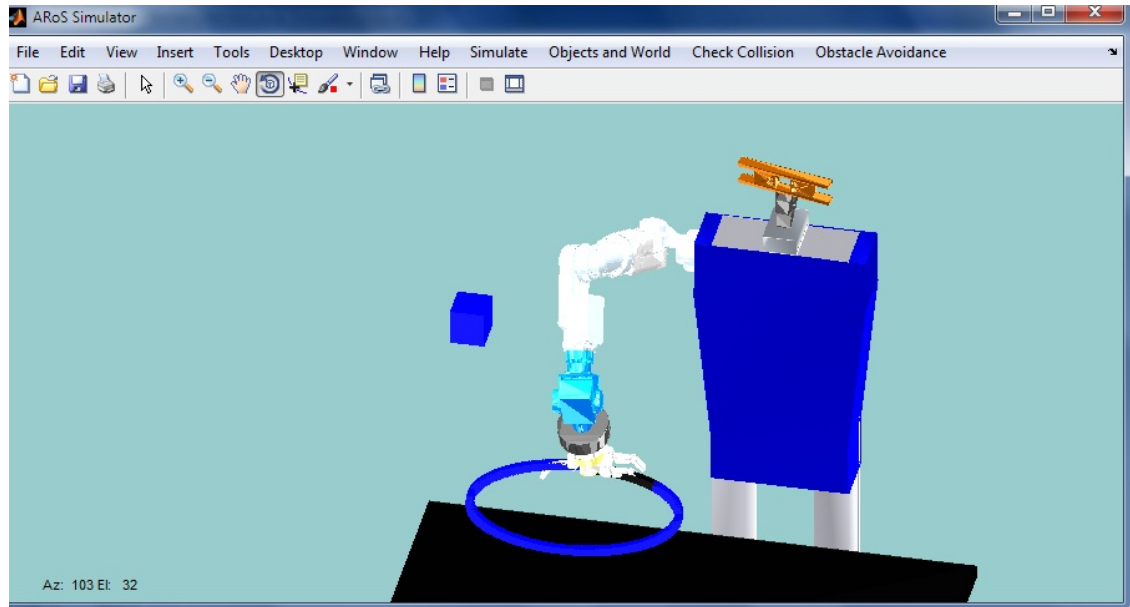
Figure A.2: The developed simulator for simulating the control of a 7-DOF manipulator in dynamic obstacle environments, using Differential Kinematics. The joint values, which are intergrated from the joint velocities, are used to update the new pose of the manipulator and the graphical models in 3D were developed previously by Eliana during her PhD thesis
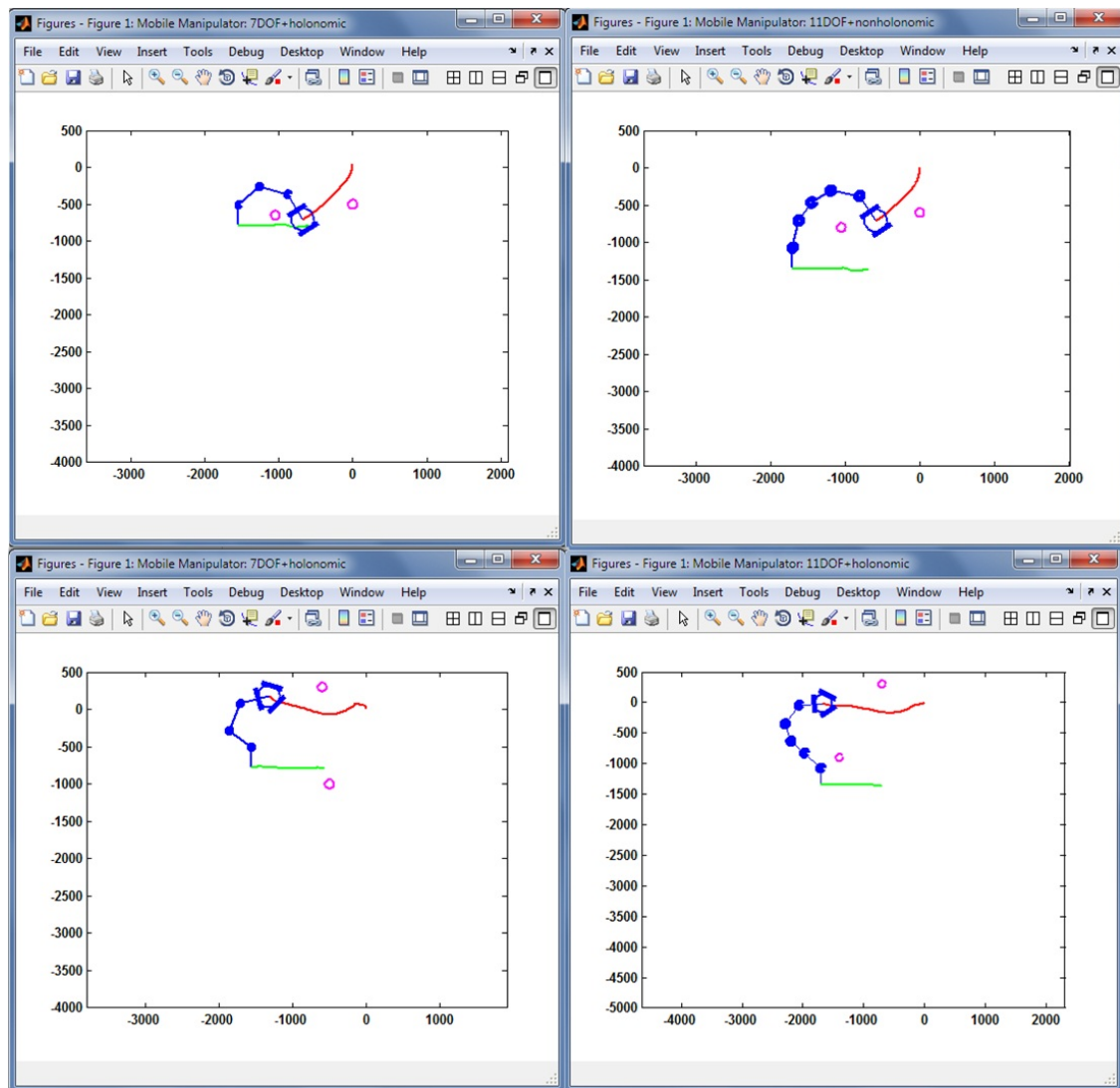
Figure A.3: The developed simulator for simulating the control of several types of mobile manipulators in unstructured environments with dynamic obstacles on the ground

Appendix B

List of Multimedia

Table B.1: List of Multimedia

Video	Description
1	Tracking and grasping a mobile object in a dynamic obstacle environment
2	Drawing an ellipse on a paper sheet in a dynamic obstacle environment by controlling the end effector velocity
3	Drawing an ellipse upon the fragile surface of a stretched and floating paper sheet with and without the compensation of the end effector orientation in the force and torque readings
4	The robot ARoS reacts sensitively to forces and torques interations from a human in a dynamic obstacle environment
5	Stiffness of the virtual system and its effects on the mobile manipulator performance
6	The inertial property of the Virtual Elastic System is adjusted to protect the system from high accelerations during the transformation from a compact configuration of the mobile manipulator

Table B.1 – *continued from previous page*

Video	Description
7	Obstacle avoidance of the manipulator when the mobile manipulator is performing an object transportation task
8	Dumbo passes through a small passage either on its left or right side
9	Dumbo goes around a passage, smaller than its size, on its left, showing that the Virtual Elastic System allows to achieve flexbile movements in difficult situations which require the mobile manipulator to use up its capability for avoiding collisions with obstacles.
10	Dumbo goes around a passage, smaller than its size on its right, illustrating that VES parameters allow the robot to know its limits.
11	Dumbo goes around a passage, smaller than its size, on its left with the support from the human partner to avoid a long obstacle
12	Some situations that the robot tells the human partner to adjust his physical interactions
13	Obstacles avoidance of both the manipulator and the mobile platform at the same time
14	Human Robot Joint Transportation
15	Wrist angle recovery
16	Simulations of controlling several types of mobile manipulators in unstructured environments with obstacles appearing on the ground, including a 7-DOF manipulator or a 11-DOF manipulator, side-mounted on a nonholonomic or a holonomic platform.

Appendix C

Parameters and their value

Table C.1: Parameters and their value

Joint limits avoidance	VES parameter φ_1	VES parameter L_2	Dynamical system
$K_{j1} = 0.4$	$\sigma_{f1} = 3$	$\sigma_{f2} = 3$	$\beta_1 = 45$
$K_{j2} = 0.05$	$\varphi_{1,min} = 100\pi/180$	$L_{2,min} = 580$	$\beta_2 = 30$
$K_{j3} = 0.3$	$\varphi_{1,max} = 220\pi/180$	$L_{2,max} = 700$	$R_{robot} = 30$
$K_{j4} = 0.2$	$\varphi_{1,0} = 130\pi/180$	$L_{2,0} = 630$	$\kappa = 200$
Singularity avoidance	$\sigma_{e1} = 2\pi/180$	$\sigma_{e2} = 3$	$D = 20$
$K_{s1} = 10^{-5}$	$\kappa_{e1} = 40$	$\kappa_{e2} = 70$	
$K_{s2} = 0.2$	$\lambda_{e1} = 10$	$\lambda_{e2} = 30$	
$\epsilon = 10^{-3}$	$\lambda_{m1} = 1$	$\lambda_{m2} = 1$	
$\Delta\theta = 10^{-3}$	$\sigma_{m1} = 10\pi/180$	$\sigma_{m2} = 600$	
Obstacle avoidance			
$K_{off} = 70$			
$K_{r1} = 2$			
$K_{r2} = 6$			
$K_{f1} = 3$			
$K_{f2} = 0.1$			